UNIVERSIDADE FEDERAL DE SÃO CARLOS

CENTRO DE CIÊNCIAS EXATAS E DE TECNOLOGIA

PROGRAMA DE PÓS-GRADUAÇÃO EM ENGENHARIA QUÍMICA

“Compreensão das propriedades estruturais e de superfície de catalisadores de platina promovidos com cério através de técnicas de caracterização *in situ* sob a reação de deslocamento gás-água”

"Insights into structure and surface properties of cerium promoted- platinum catalysts addressed by *in situ* techniques under water gas shift reaction"

Débora Motta Meira

Orientador: Prof. Dr. José Maria Corrêa Bueno

Co-orientadora: Profª. Drª. Daniela Zanchet

SÃO CARLOS – SP

2014

UNIVERSIDADE FEDERAL DE SÃO CARLOS

CENTRO DE CIÊNCIAS EXATAS E DE TECNOLOGIA

PROGRAMA DE PÓS-GRADUAÇÃO EM ENGENHARIA QUÍMICA

“Compreensão das propriedades estruturais e de superfície de catalisadores de platina promovidos com cério através de técnicas de caracterização in situ sob a reação de deslocamento gás-água”

"Insights into structure and surface properties of cerium promoted- platinum catalysts addressed by *in situ* techniques under water gas shift reaction"

Tese apresentada ao Programa de Pós-Graduação em Engenharia Química da Universidade Federal de São Carlos como parte dos requisites necessários à obtenção do título de Doutor em Engenharia Química pela área de concentração em Pesquisa e Desenvolvimento de Processos Químicos

Débora Motta Meira

Orientador: Prof. Dr. José Maria Corrêa Bueno

Co-orientadora: Profª. Drª. Daniela Zanchet

SÃO CARLOS – SP

2014

UNIVERSIDADE FEDERAL DE SÃO CARLOS

Centro de Ciências Exatas e de Tecnologia
Programa de Pós-Graduação em Engenharia Química

Relatório de Defesa de Tese
Candidata: Débora Motta Meira

Aos 28/04/2014, às 13:00, realizou-se na Universidade Federal de São Carlos, nas formas e termos do Regimento Interno do Programa de Pós-Graduação em Engenharia Química, a defesa de tese de doutorado sob o título: Compreensão das propriedades estruturais e de superfície de catalisadores de platina promovidos com cério através de técnicas de caracterização in situ sob a reação de deslocamento gás-água, apresentada pela candidata Débora Motta Meira. Ao final dos trabalhos, a banca examinadora reuniu-se em sessão reservada para o julgamento, tendo os membros chegado ao seguinte resultado:

Participantes da Banca	Função	Instituição	Resultado
Prof. Dr. Jose Maria Correa Bueno	Presidente	UFSCar	APROVADO
Profa. Dra. Daniela Zanchet	Titular	UNICAMP	APROVADO
Prof. Dr. Gustavo de Medeiros Azevedo	Titular	UFRGS	APROVADO
Prof. Dr. Tulio Costa Rizuti da Rocha	Titular	LNLS	APROVADO
Prof. Dr. Fabio Barboza Passos	Titular	UFF	Aprovado
Prof. Dr. Fabio Henrique Barros de Lima	Titular	USP	APROVADO
Prof. Dr. Leandro Martins	Titular	UNESP	Aprovado

Resultado Final: _____

Parecer da Comissão Julgadora*:

Encerrada a sessão reservada, o presidente informou ao público presente o resultado. Nada mais havendo a tratar, a sessão foi encerrada e, para constar, eu, Raquel Ferreira dos Santos Diniz, representante do Programa de Pós-Graduação em Engenharia Química, lavrei o presente relatório, assinado por mim e pelos membros da banca examinadora.

Prof. Dr. Jose Maria Correa Bueno

Profa. Dra. Daniela Zanchet

Prof. Dr. Gustavo de Medeiros Azevedo

Prof. Dr. Tulio Costa Rizuti da Rocha

Prof. Dr. Fabio Barboza Passos

Prof. Dr. Fabio Henrique Barros de Lima

Prof. Dr. Leandro Martins

Representante do PPG: Raquel Ferreira dos Santos Diniz

( ) Não houve alteração no título da tese ( ) Houve. O novo título passa a ser:

_____

_____

_____

"Chemistry without catalysis would be a sword without a handle, a light without brilliance, a bell without sound"

A. Mittasch

"Philosophy is written in this grand book, the universe, which stands continually open to our gaze. But the book cannot be understood unless one first learns to comprehend the language and read the letters in which it is composed. It is written in the language of mathematics, and its characters are triangles, circles, and other geometric figures without which it is humanly impossible to understand a single word of it."

Galileo Galilei, 1623

Aos que sempre me apoiaram incondicionalmente, Nilcéia, Sérgio e Lucas, com amor.

Agradecimentos

Primeiramente, agradeço a Deus por mais esta oportunidade de aprendizado. Em seguida a meus orientadores Prof. Dr. José Maria Corrêa Bueno e a Profª. Drª. Daniela Zanchet pelos ensinamentos, confiança e tempo dedicado em todos esses anos de trabalho. Agradeço também a Dra. Sakura Pascarelli do European Synchrotron Radiation Facility (ESRF) por ter me recebido em seu grupo durante o ano de estágio no exterior e pela atenção dedicada. Ao Dr. Olivier Mathon (ESRF) pela ajuda nos experimentos. A Profª. Drª. Clélia Mara de Paula Marques do Departamento de Química UFSCar pelo carinho e por permitir o uso do laboratório. As minhas amigas Isabel e Paula por tornarem a execução desse trabalho mais agradável e em especial à Renata Uema por toda ajuda e companheirismo, sem a qual a execução desse trabalho seria muito mais difícil. A Renata Bessa pela amizade e downloads de artigos. Aos colegas e amigos do grupo do Prof José Maria e da Prof. Daniela Zanchet Adriano, Cícero, Sato, Tathiana, Isaías, Felipe, Priscila, Ana Carmen, Luelc, Diego por toda ajuda. Aos funcionários do LNLS Cristiane, Daniela, Fábio, Simone e todos os que trabalham nas linhas de luz pela imensa ajuda e atenção. Ao Grupo da Dra. Sakura Pascarelli em especial ao Suresh Gatla e funcionários do ESRF. Aos funcionários do DEQ UFSCar e DQ Unicamp em especial a Monique. Um agradecimento a todos que ajudaram nas medidas realizadas no LNLS e ESRF, pois sem vocês as longas madrugadas e intermináveis semanas não teriam sido superadas, e boa parte desse trabalho não teria sido realizada. A FAPESP pela bolsa concedida (Proc.: 2010/52291-0). Por fim, agradeço em especial àqueles que sempre me apoiaram incondicionalmente, que apostaram em mim mais do que ninguém e que seguramente são os que mais compartilham da minha alegria: minha amada família. Em especial a meus pais Nilcéia e Sérgio, meu irmão Sérgio, minha avó Malvina e meu marido Lucas. A todos que de alguma forma fizeram parte desse trabalho, obrigada.

Resumo

Catalisadores de Pt foram preparados, informações estruturais e eletrônicas foram obtidas usando espectroscopia da estrutura fina de absorção de raios X (XAFS) em função da composição do catalisador, método de preparação, composição da atmosfera e temperatura. Dois tipos de catalisadores foram estudados: i) catalisadores sintetizados com nanopartículas de Pt (1,5% de Pt) ocluídas em uma matrix de Al_2O_3 ou CeO_2-Al_2O_3. Neste estudo, dois métodos de preparação para incorporação do cérioforam utilizados e ii) catalisadores de Pt convencionais com 0,3 ou 1% de Pt em Al_2O_3 e ainda com a adição de céria 6 ou 12%.

Para os catalisadores baseados em nanopartículas, os experimentos de XAFS foram realizados na borda L_3 da Pt e nas bordas L_3 e K do Ce sob atmosfera de redução e condições de reação de deslocamento gás-água (WGS). Os resultados de XAFS, após a redução, revelaram a presença de nanopartículas com número de coordenação (NPt-Pt) similares, em torno de 6, e distância Pt-Pt em torno de 2.75 $\pm$ 0.01 Å, para todas as amostras. A atividade catalítica e a intensidade da interação metal-suporte estão relacionadas com a estrutura do óxido de cério revelada através das análise de XAFS nas bordas K e L_3 do Ce. Medidas de infravermelho *in situ* revelaram a presença de formiatos na superfície do catalisador e que esses são provavelmente espectadores da reação. Foi possível observar que estes catalisadores mudam segundo a atmosfera e a temperatura. Assim, foi possível demonstar, usando as nanopartículas de platina, que diversos parâmetros afetam o comportamento do catalisador como: o tamanho do domínio cristalino do óxido, o contato entre o metal e o óxido e os sítios ativos expostos na superfície.

Para os catalisadores convencionais, as amostras contendo cério apresentaram-se mais oxidadas do que as amostras de platina-alumina; estas após tratamento em alta temperatura aglomeraram. No ajuste dos espectros de EXAFS, para as amostras contendo Ce, foi necessário incluir a contribuição Pt-O além da contribuição Pt-Pt. Essa contribuição Pt-O aumentou proporcionalmente à concentração de Ce demonstrando o ancoramento da Pt ao suporte através dessa ligação. A estrutura da Pt mudou de acordo com a temperatura, o suporte e composição dos reagentes na atmosfera demonstrando a importante ferramenta que são as técnicas de caracterização *in situ* para o entendimento das propriedades catalíticas.

Abstract

Pt based catalysts were measured with *in situ* X ray absorption fine structure spectroscopy (XAFS) to obtain information about the catalyst crystalline structure and electronic properties as a function of catalyst composition, method of preparation, inlet feed conditions and temperature. In these experiments, two type of catalysts were studied: i) nanoparticles of Pt occluded in Al_2O_3 or CeO_2-Al_2O_3 matrix containing 1.5 % of Pt where two different methods to incorporate the cerium were used and ii) conventional Pt supported catalysts containing 0.3 and 1 % of Pt on Al_2O_3 or with addition of 6 or 12 % of ceria.

For catalysts based on nanoparticles, XAFS spectra were acquired at Pt L_3-edge and Ce K and L_3-edge under reduction and water gas shift (WGS) reaction conditions. The XAFS results reveal, after the reduction, the presence of Pt nanoparticles with similar coordination numbers (N_{Pt-Pt}), about 6, and similar Pt-Pt distances, about 2.75 $\pm$ 0.01 Å. The catalyst activity for WGS and the strength of interaction between the metal and the support are related with cerium oxide structure revealed by XAFS analysis at Ce K and L_3 edges. *In situ* infrared spectroscopy under WGS conditions revealed the presence of formates on the catalyst surface and that they are probably spectators for the reaction. It was possible to observe that these catalysts changes according to the atmosphere and temperature. Thus, it was possible to demonstrate, using the pre-formed nanoparticles that several parameters affect the catalyst behavior like: the metallic and the oxide particle size, the contact between them and what is exposed on the surface.

For the conventional catalysts, the addition of ceria on 03PtAl sample enhances Pt oxidation, reflecting in a larger Pt-O coordination number for this sample. After reduction, 03PtAl resulted in larger Pt particles compared to the 12Ce03PtAl. For Ce-containing samples, in addition to the Pt-Pt contribution, a Pt-O contribution had to be considered to fit the spectra. This Pt-O increases proportionally to the cerium amount demonstrating that Pt clusters are anchored on support through a Pt-O bond. The Pt structure changes depends on the temperature, support nature and reactants composition, demonstrating that the catalytic properties requires the use of *in situ* characterization techniques.

LISTA DE FIGURAS

LISTA DE TABELAS

LISTA DE ABREVIATURAS

BE - binding energies

BET - Brunauer, Emmett and Teller

ΔXANES - delta XANES

DFT - density functional theory

D_p - pore size diameter

DRIFTS - diffuse reflectance infrared Fourier transform spectroscopy

ESRF - European Synchrotron Radiation Facility

EXAFS - extended X-ray absorption fine structure

FTIR - Fourier transformed infrared

FWHM - full width at half maximum

GHSV - gas hourly space velocity

HERFD - high-energy resolution fluorescence detection

HRTEM - high resolution transmission electron microscopy

HTS - high temperature shift

IC - ionization chamber

LCA - Linear combination analysis

LR - low wave number region

LNLS - Brazilian Synchrotron Light Laboratory

LTS - low temperature shift

MCT - mercury cadmium telluride

MEE - multielectron excitation effect

OSC - oxygen storage capacity

PROX - preferential oxidation

Pt-NPs - colloidal platinum nanoparticles

PVP – polivinilpirrolidone

RT – room temperature

S_{BET} - Specific surface area

SMSI - strong-metal-support interaction

TCD - thermo conductive detector

TEM - transmission electron microscopy

TGA - thermo gravimetric analyses

TOF - turn over frequency

V_p - pore volume

XAFS – X-ray absorption fine structure spectroscopy

XANES - X-ray absorption near edge structure

XPS - X-ray photoelectron spectroscopy

XRD - X-ray diffraction

WGS - water gas shift

Summary

1. Introduction

A catalyst by definition, is a material that increases the chemical reaction rate without being consumed. A heterogeneous catalyst usually is a solid with a high-surface-area on which a well dispersed metallic active phase is supported [1]. The catalytic activity and selectivity may dependent on both support and metal phase and in addition, to the interface [2][3][4][5].

The heterogeneous catalysts properties can be divided in: (i) kinetic and (ii) physical. The first corresponds to: particles morphology, number of active site that are available for the reaction, the presence of specific sites like edges, corners, facets and the interaction with the support. The second includes surface area, pore structure, density and mechanical properties like attrition resistance [6]. All these charcateristcs will reflect in the activity, selectivity and stability.

Through the years, the catalyst design has been improved based mostly on empirical work. In recent years, however, due the development of characterization techniques and computational devices the understanding about the catalysts properties is becoming more accurate. The best catalyst would be the one presenting the highest activity, 100% selectivity for the product of interest and stable for long periods. However, all these properties involve several characteristics as: particle size, particle and surface structure, composition and physical/chemical interactions between the components. More than that, it is necessary to understand the surface properties that are related with the knowledge about the active centers at atomic level and their dynamic behavior under reaction conditions.

For catalysts used for structure sensitive reactions, the most important parameters are the metallic particle size and shape. When preformed nanoparticles are used to prepare supported catalysts, the metallic particle size usually depends on the amount and kind of metal precursor, the synthesis temperature and the reductive and protective agents that are used [7]. The metallic particle size and morphology determine the number of corners, edges and kinks present on the particle, what is very important for the catalytic activity [8]. The particle size is also related to the metal-support interaction since for small particles this interface becomes important [7]. Thus, the interface, the metallic particle size and morphology can create different active sites. The knowledge about the active site is very important since it determines the catalyst

behavior. Further it is a challenging issue since it depends on the catalyst material, the gases and the temperature where the catalyst will be applied [9–11].

In this context, *in situ* characterization becomes very important once it is possible to characterize the catalysts properties under reaction conditions. All over the years, several *in situ* techniques have been developed and their use is increasing. Among them, X-ray absorption fine structure spectroscopy (XAFS) revealed to be very useful since it does not require a long range order for the crystalline structure and it is possible to obtain information about the structural and electronic parameters under different gas atmospheres and temperatures.

One structure sensitive reaction that is strategic and interesting to be studied *in situ* is the water gas shift reaction (WGS). The WGS (equation 1) is one of the reactions required to produce hydrogen, which can be used directly as fuel or as energy storage [12].

$$CO + H_2O \rightarrow CO_2 + H_2 \qquad \text{(equation 1)}$$

Although it seems very simple, the reaction mechanism is very complex giving rise to a lot of controversy in the literature [13].

Thus, the aim of this work is to obtain relevant information about the electronic and structure properties of catalysts to elucidate the nature of catalysts' active sites and reaction mechanism using *in situ* techniques. For this purpose platinum-ceria catalysts were chosen and studied using XAFS as the main *in situ* technique. It was possible to address the role of the metal-support interaction depending on the catalyst preparation method and the influence of this interface on the catalyst activity and stability.

2. Literature review

Several products, from our daily life, are produced due to heterogeneous catalysis. Polymers, pharmaceuticals, pesticides and oil refining are made through catalytic processes and contribute with the economy. In addition, catalysts are very important on environmental issues, such as the popular catalytic converters used to clean up the gas exhaustion from automobiles. One third of the entire U.S. material Gross National Product involves catalysts. Some studies reported that catalysts are responsible, per year, of $4 trillion in manufacturing. The global catalysts market is bigger than $10 billion. Catalysis is also an area that demands intensive research. In the US, $17.6 billion is spent annually on Research and Development in this field [14][15].

One product that is very important and produced through catalytic routes is hydrogen. It presents the highest energy density of all fuels and energy carriers (122 kJ/kg). It is 2.75 times more efficient than other hydrocarbon fuels. For instance, 9.5 kg of hydrogen is sufficient to replace 25 kg of gasoline. Furthermore, it presents the advantage of being a clean fuel since the only emission produced when it is used is water [16,17].

The usual hydrogen production involves reforming reactions and can be summarized by the following chemical equations [18]:

- Steam reforming

$$C_mH_n + mH_2O \rightarrow mCO + (m + \frac{1}{2}n)H_2$$

- Dry reforming

$$C_mH_n + mCO_2 \rightarrow 2mCO + \frac{n}{2}H_2$$

- Partial Oxidation

$$C_mH_n + \left(\frac{1}{2}\right)mO_2 \rightarrow mCO + \left(\frac{1}{2}\right)nH_2$$

- Autothermal reforming

$$C_mH_n + \left(\frac{1}{2}\right)mH_2O + \left(\frac{1}{2}\right)mO_2 \rightarrow mCO + (\left(\frac{1}{2}\right)m + \left(\frac{1}{2}\right)n)H_2$$

- Carbon formation

$$C_mH_n \rightarrow\ xC + C_{m-x}H_{n-2x} + xH_2$$

- Carbon removal

$$C + O_2 \rightarrow CO_2$$

$$C + CO_2 \rightarrow 2CO$$

$$C + H_2O \rightarrow CO + H_2$$

- Water-gas shift

$$CO + H_2O \rightarrow CO_2 + H_2$$

The focus of this work was the WGS reaction. As represented above, the WGS deals with the conversion of CO with steam producing CO_2 and H_2. This reaction is known since the late eighteenth century but became widely used about ninety years ago, in the ammonia synthesis, developed by Carl Bosh at BASF [19]. Nowadays, this reaction is part of many industrial processes, such as methanol production [20–24] and Fischer-Tropsch reaction [25,26]. Industrially, it is conducted in two steps. The first one, known as high temperature shift (HTS) reaction (300-500 ^{0}C) uses iron-based catalysts. It reduces the CO level, from a methane steam reformer, for example, from 8-10% to 3-5%. In the second one, a Cu/ZnO/Al_2O_3 catalyst is used at low temperatures (LTS, 200-300 ^{0}C) and the CO concentration in the hydrogen stream decreases typically below 1% [27]. This low level of CO will not poison the catalyst used for ammonia synthesis, but it can be further decreased using a preferential oxidation of CO (PROX). Finally, hydrogen can be used for fuel-cell application [28].

Although the WGS has been used for long time, the reaction mechanism is still controversial, being a consensus that it depends on the reaction conditions and on the catalyst [29,30]. The two main reaction schemes that have been proposed are the redox mechanism and the associative mechanism. In the redox mechanism, the metallic particle adsorbs CO and the reducible oxide (from the support) provides labile oxygen in a mechanism called Mars-van Krevelen [31]. For this mechanism, the particle oxidation state is not specified, neither the reaction intermediates; however, it is pointed out a synergistic effect between the particle and the support [31] [32]. In the associative mechanism, formates, carbonate and carboxylate species have been proposed as intermediates; CO is oxidized directly from water while the oxygens from the support do not participate in the reaction [32]. Another mechanism proposed is the associative mechanism with redox regeneration (via carboxyl or formate). This mechanism can be described by a H-transfer between the two oxygen atoms in the –

COOH (or –HCOO) carboxyl intermediate (or formate intermediate) forming a more stable intermediate that will be dissociated and will form the products. A fourth reaction pathway deals with the adsorption of a second CO on the oxygen vacancy prior to water dissociation. Due to the oxygen vacancy CO adsorbs strongly on the Pt, being the linear orientation more stable for the second CO adsorption in the presence of water. For this mechanism, after the CO adsorption a H atom from the interfacial OH goes to the Pt. CO_2 desorbs generating an interfacial oxygen vacancy where H_2O adsorbs and dissociates leading to H_2 desorption. The redox and the associative mechanisms are represented in Figure 1**.**

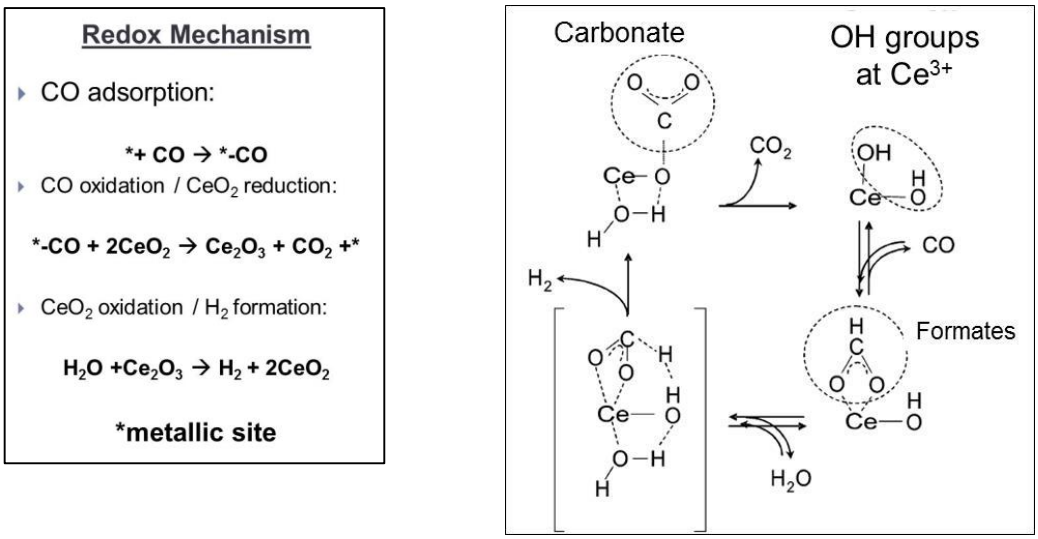

Figure 1. Schematic representation of WGS pathways involving an interfacial site of a metal cluster supported on a reducible metal oxide.

Phatak et al [33] studied the kinetics of WGS reaction using platinum-alumina and platinum-ceria catalysts considering two mechanisms. They evaluated the possibility of a redox mechanism where CO is oxidized to CO_2 on the surface (CO* + O* → CO_2* + *, where O* comes from the support surface) and a modified redox mechanism where the CO is oxidized directly by the OH (CO* + OH* → CO_2* + H*) and concluded that was not possible to establish which one happens or which are the reaction intermediates. On the other hand, nonmetallic platinum species, Pt-O_x-Ce, were reported by Fu et al. [34] as the active species for low-temperature WGS reaction on Pt/CeO_2 catalysts also using a gas mixture that simulates a reformate gas

composition. They identified Pt^{2+} and Pt^{4+} but no Pt^{0} suggesting a reaction pathway involving these cationic species.

Whatever mechanism is considered, the water activation is the determinant step for the WGS reaction [35], as for the other reforming reactions. However, as it was highlighted above, three questions remain unclear: the reaction mechanism, the role of each catalyst constituent and the importance of the interaction between them. Each one of these parameters participates in different ways favoring the reaction. Thus, many studies have been performed to understand the catalyst characteristics that are necessary to promote the reaction and their relation to the reaction mechanism. Theoretical studies using DFT (density functional theory) [36] have shown that the dissociation of water is favored on small metal particles and decreasing the metal particle size, more favored will be the water dissociation. Experimental studies exploring different preparation methods have also been performed. The preparation method will determine the contact between the metal and the oxide [37] and thus the interaction between them and the reaction pathway. Furthermore, studies exploring different methods of synthesis are interesting since the WGS is a structure sensitive reaction. In other words, the reaction rate depends on the metal particle size and thus varying the catalyst preparation method different metal particles can be obtained and different catalysts can be studied.

There are several catalysts preparation methods, the most common are: deposition-precipitation, coprecipitation and impregnation. Another approach that has progressed a lot in the last twenty years is to use pre-formed nanoparticles to produce supported catalysts. Using nanoparticles, it is possible to obtain controlled materials through the control of the size and/or shape of the metallic phase and/or the support and thus influencing the catalysts properties [38]. The colloid method is the most common. It involves the reduction/decomposition of a metal precursor by a reducing agent/temperature in the presence of a protective agent that prevents agglomeration. For certain reactions, the nanoparticles can be used in solution, acting as a “homogeneous” catalyst [38]. In other cases, they have to be supported on high-surface-area materials to be used as a “normal” heterogeneous catalyst. Normally, after being incorporated on the support it is necessary to remove the protective agent to make the catalytic sites available for the reaction. The temperature used to remove the protective agent is important since high temperatures can lead sintering [39].

One of the main metals, that are used as catalysts, is platinum and several methods have being described in literature to obtain nanoparticles [38]. Platinum is very expensive and its dispersion is usually maximized to enable it to be used. The platinum stability, against sintering, will depend on the Pt-support interaction. This interaction generally starts at the last step of catalyst preparation, the calcination. Normally the calcination deals with high temperatures and oxidative atmosphere. At high temperatures more stable structural phases are formed and/or protective agent are removed from the nanoparticles. Generally, it is also necessary to remove anionic species like NO_3^- and Cl^- from the metallic precursor that can poison the metallic particles. During the calcination, PtO_x is formed and when these species weakly interact with the support sintering occurs. However, in the presence of a reductive oxide like ceria, PtO_x species become stable enough and not only sintering is avoided but a redispersion may occur. The Pt sintering/redispersion is a reversibly process and depends on the temperature and the atmosphere [40]**.** Vayssilov et al. [41] showed that for Pt nanoparticles supported on CeO_2 an electron transfer occurs from Pt to ceria, leading to the formation of Ce^{3+} near the particles. In addition to the electron transfer from Pt to CeO_2, they identified that reverse oxygen spillover from CeO_2 to Pt also occurs above 130 ^{0}C. Thus, electronic changes were observed favoring the platinum stability. It was also reported in the literature [42–44] for Pt-CeO_2 catalysts that the ceria surface oxygen atoms are an anchoring site for Pt and that it depends on the ceria surface. Besides this advantage of improving the Pt stability, ceria presents a high oxygen storage capacity (OSC). This is due to the possibility of vacancy formation that arises from the reversible conversion between CeO_2 and CeO_{2-x} making it an excellent oxygen carrier [45–50].

The energy required to form an oxygen vacancy is lower for small particles compared to surfaces and is inversely proportional to the particle size [51,52]. Migani et al. [51] demonstrated that the energy separation between the valence and the conduction band for ceria nanoparticles is lower compared to a (111) surface, promoting the vacancy formation. The addition of a metallic particle like platinum favors the formation of Ce^{3+} ions by electron transfer from the metal cluster. Thus, the vacancy formation also depends on the contact between the removed O and Pt [53].

Concerning ceria crystallographic orientation earlier studies proposed a high OSC for the (100) surface when compared to (110) or (111) since the energy

required to form an oxygen vacancy is smaller [54,55]. Further experimental observations and DFT analysis stated that oxygen vacancies tend to group together in clusters [56]. Thus, it is possible to observe that the OSC depends on the CeO_2 particle size, on its surface structure and the proximity of this particle to a metallic particle. These characteristics can be tuned by the preparation method.

Although all this advantages, ceria is much more expensive than other common supports like SiO_2 or Al_2O_3 and presents lower thermal stability [37]. Alumina is the most used support in catalysis due its thermal and mechanical stability. Al_2O_3 exists in several structures but the most interesting are: α-Al_2O_3 that is crystalline and γ-Al_2O_3 that is amorphous and porous. The later typically presents high surface area (50-300 m^2 g^{-1}), high thermal stability and is easily shaped like pellets [57]. Thus, combining ceria with alumina is a good strategy to improve the ceria surface area, dispersion and stability [34] [58] [59] [60] [61].

One method to obtain alumina is the sol-gel method since it is possible to control the pore size, the surface specific area, the structure and the final composition when more than one component is used in the synthesis [62] [63]. Several parameters affect the sol-gel process: precursor type, solvent, amount of water, pH, temperature, gel drying, etc. They can change the gel and as consequence, the final material [63].

Thus, it is possible to notice that through the catalyst preparation method is possible to control the catalysts properties. Using a more controlled system it is possible to study the parameters that will affect the reaction and as a consequence the reaction mechanism.

Pierre et al. [64] prepared Pt-ceria catalysts using different methods in order to obtain ceria nanoparticles and high amount of reactive surface oxygen. They demonstrated the importance of the carbonate removal from the surface, which is formed during WGS, using hydrogen and oxygen to obtain a catalyst more active. Deng et al. [65] demonstrated that in the presence of a small amount of oxygen an increase in stability for Au or Pt-ceria catalysts for WGS is observed. These studies were carried out at low and high temperatures as well in a cyclic shut-down/start-up operation. They claimed that is possible to use these catalysts to WGS and PROX in one reactor thus presenting an advantage for fuel-cell application. Other metals were also studied for WGS reaction. Fu et al [34] demonstrated that Au is anchored on ceria surface defects

that leads to active sites for WGS reaction being the sample inactive when Au was completely removed by leaching. Kyriakou et al. [66] used 1% of Pd combined with 99% of Cu and demonstrated using a single atom approach how a very small amount of reactive metals can affect the catalytic activity specially for bimetallic catalysts. Wheeler et al [67] observed the activity order is Ni>Ru>Rh>Pt>Pd above 300 ^{0}C and a reactant composition of CO:H_2:H_2O = 1:2:4. However, Pt/CeO_2 catalyst was more active than Au/CeO_2 or Au/Fe_2O_3 for low temperature WGS reaction for several CO/H_2O ratio. Moreover, water addition to the feed presented a more pronounced effect for the platinum catalyst [68]. Further, the turnover frequency of Pt(111) is initially 5 times higher than Cu(111) [69]. On the other hand, it deactivates with time by carbon deposition except when Pt is in contact with reducible oxides [70]. In addition, higher activities were found for Pt on a mixed Ce-TiO_2 support than when is supported on each oxide individually [71]. Thus more than the isolated properties coming from the metallic phase or the support the importance of their interaction, as mentioned before, have been assigned to contribute with the catalyst activity and stability.

The first time that the catalytic performance was related with the properties of the support and the metallic phase was in beginning of 1930 with Schwab et al. [72]. Using the term “electronic factor” that came from semiconductors they explained the electron transfer between the support and the metallic phase leading to changes in the reaction rate. Two types of interactions were proposed: i) structural, related to the metallic phase stabilization by the support and ii) synergetic, related to electronic interactions leading to a new active component like due to the support-metal interface.

Changes in the gases chemisorption were observed, for group VIII metals, when they are supported on reducible metal oxides. Tauster et al. [73,74] in 1978 used for the first time the term “strong-metal-support interaction” (SMSI) to explain these effects. Later, Haller et al. [75] included in this definition any interaction between an active metallic phase and the support. Nowadays the SMSI is explained by electronic effects being the changes in the chemisorption properties due electron transfer from the support to the metallic active phase. Campbell et al. [76] proposed this description for highly dispersed nanoparticles in contact with ceria with high surface area. Another effect that is proposed to explain this metal-support interaction is the encapsulation. In this case the support would cover the metallic phase depending

on the gases atmosphere and/or the temperature [77]. This “decoration” phenomenon was observed experimentally by high resolution transmission electron microscopy (HRTEM) for several metallic particles supported on oxides, proving to be a reversible phenomenon [1]. Liu [1] defined the metal-support interaction more generally as *“any effect that a support material modifies the performance of a supported metal catalyst via the synthesis process or during a catalytic reaction”*. Thus, they included *“anchoring and sintering of metal/alloy nanoparticles, formation of interfacial interphases or new compounds, decoration or encapsulation of metal nanoparticles by support-derived materials, the influence of support on the shape of metal alloy nanoparticles, and the electron transfer between the support material and metal/alloy nanoparticles”*.

Two main factors determine the metal-oxide interaction: (i) the metallic particle size and (ii) the preparation method of the catalysts. Smaller the particle size, bigger is the interaction due to the species ranging, from metallic to ionic form, that are available at the interface [78].

One preparation method that favors this interaction between the metal and the support is the impregnation. Using low metal content, the presence of metal atomically dispersed is favored being more “sensitive” to the support effects. Further, these highly dispersed systems are strongly sensitive to the environment to which they are exposed, either in a characterization chamber or in reaction conditions [79].

One interesting effect, which comes from this metal-support interaction, are the changes caused by the metallic phase in the oxide redox properties. Two explanations are found for this: the first is the hydrogen spillover, through the metal, to the support surface [3]; in other words, the hydrogen is dissociated on the metal surface generating atomic hydrogen that reduces the oxide [80]. The second is related with electronic interactions between the metal and the oxide [81,82] characterized by a disturbance from the noble metal on the electronic band of the oxide being this later reduced directly by H_2. Acerbi et al. [83] reported that ceria reduction temperature, in the presence of a noble metal, correlates with on the metal work function. The work function is the minimum energy needed to remove an electron from a solid and take it infinitely far away at zero potential energy [57]. Like this, Acerbi et al. [83] reinforced the idea that electronic interactions at the interface are very important although they did not exclude the spillover effect.

Electronic changes on platinum when in contact with ceria, due to the metal-support interaction, improves water dissociation and as a consequence, the catalytic activity increases for WGS reaction [36]. The conversion is directly proportional to the interaction. The catalytic activity is further increased when ceria is co-deposited as nanoparticles with Pt on bulk TiO_2 (110), since like this platinum and ceria will be well dispersed on the surface. The transfer of oxygen from ceria to Pt opens a new path for the WGS reaction. Qiao et al. [84] studied the nature of the active sites on catalyst with very low platinum supported on high-surface-area FeO_x showing that it is possible to keep the platinum in ionic form well dispersed on the oxide surface during WGS. Moreover, the catalysts are stable during CO oxidation reaction. Their conclusion was that atomically dispersed Pt–O species act as catalytic centers single-site — opposing the conclusion from a previous work that showed that cationic platinum in Pt–O sites on FeO_x are the active centers for CO oxidation [85].

Thus, despite the importance of this metal-oxide interface for the catalyst activity and stability, especially under reaction conditions, it is not well established in the literature how this metal-oxide interface participates in the mechanism reaction. Only recently it has become possible to understand the metal-oxide interface since over the past few years several techniques have been developed to characterize the structural and electronic properties of catalysts under reactions conditions. Some of them are: X-ray diffraction, pair-distribution-function analysis, X-ray absorption fine structure, transmission electron microscopy, ambient-pressure X-ray photoelectron spectroscopy and infrared spectroscopy [86]. Among them, XAFS progressed a lot due the availability of high flux synchrotrons, new set-ups development like furnaces, gases, pressure and temperature controllers and the possibility of coupling more than one characterization technique. Compared to diffraction based techniques, where it is necessary particles minimally ordered to give Bragg diffraction, XAFS presents as advantage, the possibility of characterize materials without long order range. Furthermore, the statistics is improved when compared with Transmission Electron Microscopy (TEM) since it probes a high number of particles. As disadvantages, the data obtained is an average and the data analysis should be carried carefully and compared with other techniques to reveal more consistent results [87].

Frenkel et al. [8] demonstrated the possibility of understanding nanoparticles shape and morphology and also a relation between temperature and

bond distances for small metallic nanoparticles using Extended X-Ray Absorption Fine Structure (EXAFS) analysis. Recently [9], using high-energy resolution fluorescence detection (HERFD) they demonstrated the correlation between bond strength and particle-support interaction. Also using XAFS, Nagai et al. [40] demonstrated how platinum stability can be increased by the presence of Pt oxide on ceria surface being the sintering and redispersion a reversible phenomenon. The redispersion was favored at low temperatures and oxidative atmosphere. Agostini et al [88] studied Pd catalysts prepared via deposition-precipitation method. For the unsupported material (amorphous), it was possible to determine the local structure around Pd by EXAFS. For the supported material, it was possible to observe the crystallization and sintering due to thermal treatments. They also studied the materials under reductive atmosphere and observed that Pd-O contribution for the first shell was replaced by Pd-Pd contribution forming a fcc structure. They also studied different supports and observed variations for the Pd particles size depending on the support. Comparing alumina and different types of carbon they confirmed the alumina ability to stabilize the particles. Nagai et al. [89] identified using ex situ EXAFS a Pt-O-Ce bond at the surface that would be responsible for anchoring the platinum particles. A Pt-O-Ce bond was also reported as responsible for stabilizing platinum particles in a cerium-zirconia support under oxidizing atmosphere and high temperatures [2]. Guo et al. [90] studied Pt and Au catalysts for WGS to identify their structure and relate it with the activity. Using EXAFS they concluded that the active phase for both metals is completely reduced. Using X-ray absorption near edge structure (XANES) they identified the adsorbates covering the metallic surface. By XANES it is possible to identify the oxidation state and adsorbates effects on the surface [91]. Three types of adsorption sites have been reported based on XANES analysis [92]: ontop, atop and n-fold, relating to where the adsorbed is linked on the particle surface. The bond strength of the adsorbates on Pt depends on the support ionicity, temperature and gas pressure [92].

Thus, it is possible to note that several studies have been performed through the years, a lot of progress has been made, but not final conclusions concerning the mechanism reaction and catalytic active site have been obtained. Concerning the formation of the catalytic active site, the metal-support interaction is claimed to play an important role for the reaction success as for the catalysts stability. However, the way and the conditions that this interaction occurs are not well

established. Therefore, the study of catalysts constituents using *in situ* techniques is very interesting since the characteristics can change depending on the atmosphere and temperature and thus may lead the catalysts development.

3. Objective

The aim of this study is to explore *in situ* characterization techniques to understand the role of the catalysts constituents (metallic phase and support) and the effect of their interaction in the water gas shift reaction, a structure sensitive reaction in which this interface is relevant.

4. Consideration

This thesis is divided in two independent sections, based on the catalysts preparation method (Pt pre-formed nanoparticles (Part I) and conventional impregnation (Part II)). The materials and methods will be described for both together in Part I, except for particular experiments that will be described in details in each specific part.

Part I

I. 5. Materials and Methods

I. 5.1. Catalysts preparation – Pt pre-formed nanoparticles

Colloidal platinum nanoparticles (Pt-NPs) were prepared as described elsewhere through hexachloroplatinic acid reduction by ethylene glycol using polivinilpirrolidone (PVP) as a protective agent (molar ratio PVP/Pt =10) [93].

The nanoparticles were incorporated (1.5% Pt (w/w)) during the sol-gel synthesis of alumina (PtAl) and cerium-alumina oxides [94].

Twelve and 20% (w/w) of CeO_2 were added in two ways: during the sol-gel synthesis or by impregnation of $Ce(NO_3)_3.6H_2O$ (99.9%, Aldrich) on the PtAl catalyst. After gel drying, the samples were calcined at 500 ^{0}C (4 ^{0}C.min^{-1}, in synthetic air for 4 h). For the impregnated samples another calcination was carried out, in the same conditions described for the samples where cerium was added to the gel, after the impregnation.

The catalyst will be labeled as g-Pt*x*CeAl (x = 12 or 20 % Ce) for the samples in which Ce was added during the sol-gel synthesis and i-xCePtAl for the samples in which Ce was impregnated on PtAl catalysts. To differentiate just the preparation method, independently of Ce content, the samples will be called “GEL samples” and “IMP samples” when Ce was added during the sol-gel synthesis and when Ce was impregnated, respectively.

I.5.2. Characterization

I.5.2.1. X-ray diffraction (XRD)

X-ray diffraction (XRD) patterns were collected with a Rigaku Miniflex DMAX 2500 PC (30kV-10mA) diffractometer using Cu Kα radiation in a range for 2θ from 5 to 90^0 with a scan rate of 2 °.min^{-1} and step of 0.02°.

I.5.2.2. Specific surface area (S_{BET}) and pore volume (V_p)

Specific surface area (S_{BET}) and pore volume (V_p) were measured by N_2 adsorption–desorption isotherms at -196 ^{0}C, using a Quanta Chrome Nova 1200. The samples were degassed at 200 ^{0}C under vacuum for 2 h. The S_{BET} and pore volume (V_p) were calculated using the Brunauer, Emmett and Teller (BET) and Barrett-Joyner-Halenda (BJH) methods, respectively.

I.5.2.3. X-ray photoelectron spectroscopy (XPS)

X-ray photoelectron spectroscopy (XPS) spectra were obtained with a SPECSLAB II (Phoibos-Hsa 3500 150, 9 channeltrons) SPECS spectrometer equipped with an Al K_α source (1,487 eV, E_{pass} = 40 eV, energy step = 0.2 eV, and acquisition time = 2 s per point) at Brazilian Synchrotron Light Laboratory (LNLS). Samples were prepared as pellets (100 mg) and transferred to the XPS pre-chamber under an inert atmosphere, and maintained under vacuum for about 12 h. The residual pressure inside the analysis chamber was less than 1 x 10^{-9} torr. The samples were reduced in a furnace attached to the XPS instrument, by heating up to 500 ^{0}C (10 ^{o}C min^{-1}) under a mixture of 5% H_2 in N_2 for 1 h. Due to the overlap of the Pt 4f and Al 2p peaks, the Pt $4d_{5/2}$ peak was used to evaluate the concentration and chemical state of the Pt. The binding energies (BE) were referenced to the Al 2s (118.9 eV). The BE of Pt 4d, O 1s, N 1s, C 1s and Ce 3d core levels were determined by computational fitting using the CASAXPS (version 2.3.13) software, to an accuracy of $\pm$ 0.4 eV.

I.5.2.4. Fourier transformed Infrared (FTIR) spectra with CO adsorption

Fourier transformed Infrared (FTIR) spectra with CO adsorption were recorded using a Thermo Nicolet iS50 FTIR spectrophotometer equipped with a Mercury Cadmium Telluride (MCT) detector and a Harrick diffuse reflectance infrared Fourier transform spectroscopy cell with CaF_2 windows. CO adsorption measurements of supported catalysts were carried out using approximately 80 mg of sample. The samples were pre-reduced up to 500 ^{0}C (10 ^{o}C min^{-1}) under a mixture of 25% H_2 in N_2 flowing at 45 mL min^{-1} for 1 h. After this, the samples were cooled to 25 ^{0}C in N_2. FTIR spectra (64 scans at 4 cm^{-1} resolution) were then collected after 5 min exposure of the catalysts to CO at 25 ^{0}C and 20 torr.

I.5.2.5. Oxygen storage capacity (OSC)

Oxygen storage capacity (OSC) was measured using a thermo gravimetric analyses (TGA) system (e.g. TA Instruments, SDT Q600 TGA/DSC). The samples were first reduced *in situ* using H_2 (5%H_2/N_2, 2.5 ml.min^{-1} and total flow 100 ml.min^{-1} completed with N_2) by heating up to 500 ^{0}C (10 ^{0}C.min^{-1}) for 60 min. Then, the temperature was decreased to 400 ^{0}C. At this temperature alternate flows (5 cycles) of O_2 (20% O_2/N_2, during 5 minutes) and H_2 (5% H_2/N_2, during 5 minutes) (both 2.5

ml.min^{-1} and total flow 100 ml.min^{-1} completed with N_2) were performed. The mass change indicates the oxygen uptake and release capacity of the catalyst. The temperature was decreased down to 100 ^{0}C, using 100 ^{0}C steps, and in each step the cycles were repeated. A typical curve obtained during the OSC experiments is presented in Figure 2. The peak highlighted with a red square is an artifact due to the gas exchange since the gas inlet is placed on top of the sample and thus it does not correspond to a real mass variation from the sample. Several tests were done to check if increasing the exposure time for each gas would be possible to obtain a curve completely flat however it was not possible. Thus, the mass variation (Δm) was measured for all the samples at the end of the oxygen cycle since it was the flattest part of the curve. The results were averaged. A platinum-alumina sample was measured and Δm for this sample was negligible and thus the results correspond to ceria variations. Δm was converted to µmol of O_2 and related with the catalyst mass used during the test. Knowing the catalyst mass and composition was also possible to calculate the OSC as a function of ceria content [95].

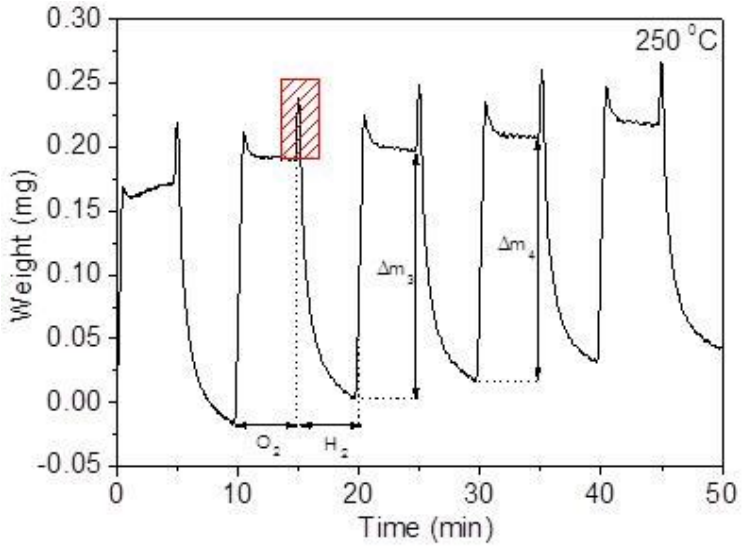

Figure 2. Typical curve obtained during an OSC experiment.

I.5.3. *In situ measurements*

I.5.3.1. X-ray absorption fine structure spectroscopy (XAFS)

XAFS is a very useful technique for materials characterization, in particular for heterogeneous catalysts. Developments along the years involving synchrotron light sources and experimental set up allowed experiments that are more

sophisticated. This was the most important technique for this work, thus will be discussed and described with more details below.

I.5.3.2. XAFS experiment scheme (resumed)

Normally, the beamline can be divided in optical hut and experimental hut. The optical hut is where the photons from the machine arrive and mirrors, slits and monochromator, for example, are used to select the best conditions to perform the experiments. The experimental hut is where the samples are placed with the necessary apparatus to perform the *in situ* experiments, like cryostats and ovens. We can also find, in the experimental hut, the detectors that will collect the signal. Among them, we used two types, depending on the kind of sample: the fluorescence detector and the ionization chambers. The ionization chambers detect the beam before and after the sample. Normally three ionization chambers are used. The photons will arrive at the first one (IC_0) and then pass through the sample (in our case placed inside a furnace) that is followed by the second ionization (IC_1) where the photons that were not absorbed by the sample will be detected. Next, there is the third ionization chamber (IC_2). Between the second and the third ionization chambers a standard reference is placed. This is represented in Figure 3(A). The measurements can be done instead of transmission mode in fluorescence mode for diluted samples and in this case a detector is placed perpendicular to the beam and the sample 45^0 in relation to the beam. In our case, due the furnace there were no photons passing to IC_1. The scheme is presented in Figure 3(B).

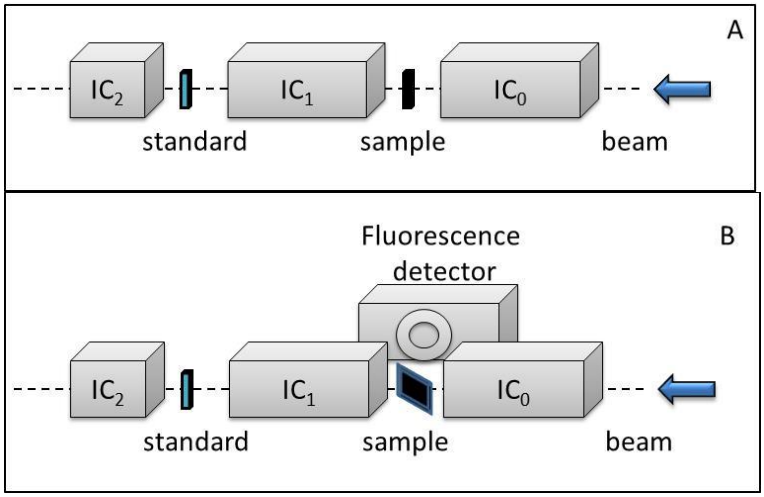

Figure 3. (A) Scheme for transmission XAS experiment. IC_0, IC_1 and IC_2 are the ionization detectors. (B) Scheme for fluoresce XAS experiment.

For the transmission mode, two different furnaces were used and another one was used for fluorescence mode. Figure 4(A) shows the first furnace for transmission. It has a quartz tube, with two Kapton windows, that is placed in a ceramic box with resistance cartridges to heat the sample. The gas flow goes in from one side of the tube and goes out at the other side. The sample is placed in a horizontal support where the thermocouple is.

Figure 4(B) shows the other oven for transmission measurements. In this case, the sample is placed in a vertical base and the gas is blown near the pellet to fill the whole chamber (built in stainless steel with Kapton windows) and goes out through the bottom part. In this vertical base is the resistance cartridge to increase the temperature and the thermocouple.

In both cases, the beam comes from one side of the oven pass through the sample and goes out through the other side and it is possible to measure the standard simultaneously to the sample.

Figure 4(C) shows the oven for fluorescence measurements. It has a round base where the pellet is placed. Behind this base, are the resistances used for heating and the thermocouple. The gas comes from the upper part and goes out from the bottom part and the oven is sealed with a Kapton window and O-rings. The photons come from one side and part is emitted as fluorescence being collected by the detector. In this geometry, it is not possible to measure the standard simultaneously.

For all setups, the samples are used as pellets and the mass was calculated to maximize the jump and reduce the absorption or fluorescence emitted from the rest of the sample.

It is important to highlight that the cells used for XAFS experiments are not perfect catalytic reactors because a compromise has to be made between the conditions that are necessary to perform the XAFS measurements and the catalytic activity such as bed geometry, temperature, flow, diffusion limit, etc. Nevertheless, several results in the last years [87] show that important insights about catalyst behavior have been obtained, which was only revealed in the *in situ* measurements.

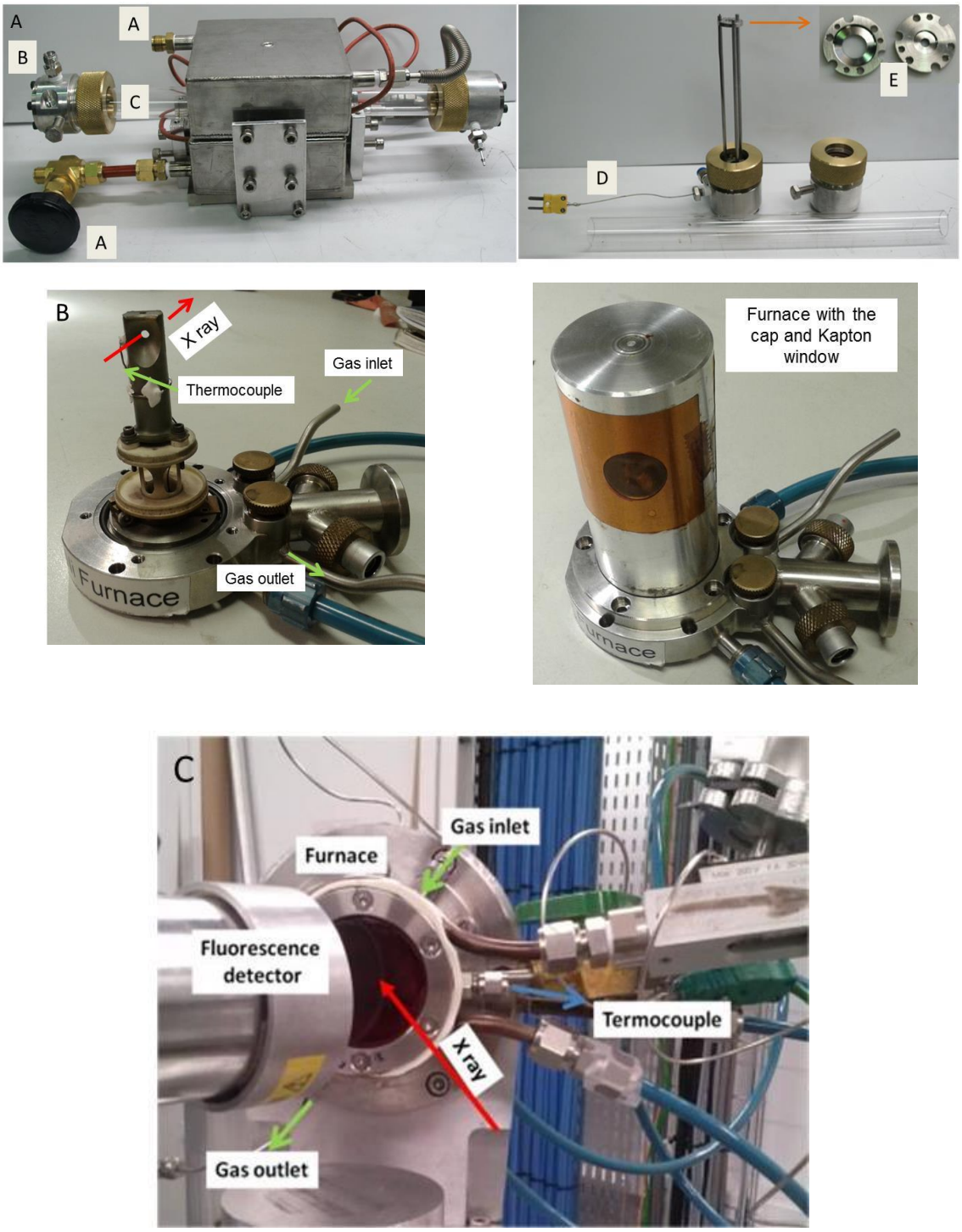

Figure 4. (A) Tubular furnace (a) water cooling system, (b) connection for the gases, (c) quartz tube, (d) thermocouple and (e) sample holder; (B) Transmission furnace. (C) Furnace and set-up used for fluorescence measurements. Set up (A) is from LNLS and (B) and (C) from ESRF.

I.5.3.3. XAFS theory

The sample absorption coefficient, μ(E), is measured as a function of the photon energy (E) being represented by a monotonically decrease function:

$$\mu(E)/\rho \approx Z^4/AE^3 \quad \text{where}$$

ρ = sample density
Z = atomic number
A = atomic mass

From this equation, it is possible to observe that the spectrum is dependent on the metal loading (reflecting at the edge jump) and the support nature.

The μ(E) is divided in two regions: XANES that is near the edge and EXAFS the extended region after the edge.

As mentioned before, for a transmission experiment, the X-ray beam is measured by the ionization chambers and its intensity can be represented by IC_x, where x corresponds to which ionization chamber it is referred to (IC_0, IC_1, IC_2). Thus, μ(E), the energy measurement and the IC_x can be related through Lambert-Beer law:

$$IC_x(E) = IC_{(x-1)}(E)e^{-\mu(E)d} \quad \text{where}$$

$I_{(x-1)}$ = ionization chamber before the one of interest (x).
d = sample's concentration

For fluorescence experiments μ(E) is given by:

$$\mu(E) = F(E)/IC_0(E) \quad \text{where}$$

F = intensity of the fluorescence yield emitted by the sample.

A signal intensity reduction, when fluorescence mode is used, happens due to sample self-absorption. It is negligible for diluted samples or should be corrected adjusting the samples thickness and/or dilution.

The normalization of μ(E) oscillatory part defines the EXAFS spectrum χ. This is done by subtracting from μ(E) a pre-edge μ_0(E) and a normalization function to the edge jump. Normally, it is expressed as a function of the modulus of the wave vector, k:

$$k = \sqrt{\frac{2m}{\hbar^2}E_f} = \sqrt{\frac{2m}{\hbar^2}(\hbar\omega - E_b)} \quad \text{where}$$

m = photoelectron mass

E_f = photoelectron kinetic energy

$\hbar\omega$ = energy of incoming photoelectron

E_b = binding energy photoelectron

Thus, the EXAFS signal, χ (k), is

$$\chi(k) = [\mu(k) - \mu_0(k)]/\mu_0(k)$$

It can be expressed also in terms of energy:

$$\chi(E) = [\mu(E) - \mu_0(E)]/\mu_0(E)$$

Since, $\mu_0(E)$ is not well behaved normally the value of the background function is evaluated at the edge energy:

$$\chi(E) = [\mu(E) - \mu_0(E)]/\mu_0(E_0)$$

Finally, the EXAFS equation, considering a single scattering, can be expressed k-weight as:

$$k\chi(k) = S_0^2 \sum_i \frac{N_i A_i}{r_i^2} e^{\left(-\frac{2r_i}{\lambda}\right)} e^{\left(-2\sigma_i^2 k^2\right)} \sin[2kri + 2\phi i(k)] \quad \text{where}$$

S_0^2 = passive electron reduction factor

λ = photoelectron mean-free path

i = different coordination shells around absorbing atom

$A_i(k)$ = amplitude function for the scattering atom (Å)

φ_i (k) = phase function of the of the i*th* shell

N_i = coordination number of the i*th* shell

r_i = interatomic distance of the i*th* shell

σ_i = Debye-Waller factor of the i*th* shell

The Debye-Waller factor quantifies the system disorder and can be expressed by the dynamic term (σ_T), due to thermal disorder, and the static term (σ_D) due to structural disorder:

$$\sigma_i^2 = \sigma_{i,T}^2 + \sigma_{i,D}^2$$

Applying a Fourier transform to the $\chi(k)$ function (weighting k = 1, 2 or 3), it is possible to isolate the contributions of each coordination shell in R-space. By performing the fit, the best values of N, r and σ are found by minimizing the difference between experimental and modeled curves.

When is necessary to describe a non-Gaussian distribution of atoms the third and fourth cumulants are included to this equation.

According to Nyquist theorem, the maximum number of parameters (n_{ind}) that can be fitted is related to the interval in k and in R according the equation:

$$n_{ind} = 2\Delta k \Delta R/\pi$$

Table 1 present's Δk, ΔR, n_{ind} and the number of parameters that were fitted (n_R) in each case (depending on the edge, platinum or cerium and the temperature). The way that the fits were performed will be explained ahead.

Table 1: Maximum number of parameters calculated using Nyquist theorem and number of parameters used in the fit.

	Δk	ΔR	n_{ind}	n_R
Platinum	9	2	11	3
Ce gel	7	2	9	8
Ce impregnated	7	3	13	6

I.5.3.4. X-ray absorption measurements

XANES and EXAFS at Pt L_3-edge (11564 eV) were measured at BM23 beamline of the European Synchrotron Radiation Facility (ESRF). A double crystal monochromator equipped with a pair of Si (111) crystals was used with energy resolution of 0.3 eV. Harmonic rejection was obtained using two Si mirrors with an angle of 2 mrad. The samples were prepared as pellets (150 mg for a jump of 0.2) and placed into a furnace with Kapton® window [96] (Figure 4C). Data was collected in fluorescence mode using a 13 elements Ge detector.

The samples were reduced *in situ* by heating up to 500 ^{0}C under 100 mL.min^{-1} H_2:He flow (5:95) for 90 min. During this process, XANES spectra were recorded in the energy range 11500 to 11620 eV. Each spectrum took about 13 min. The sample was cooled down to room temperature under H_2 and EXAFS was measured in the energy range 11200 to 12200 eV (kmax = 13 Å^{-1}).

XANES measurements were also carried out for some of the samples under WGS reaction conditions. The H_2O/CO ratio = 10 was used, with 5.4 mL.min^{-1} flow of 5%CO/He. One hundred mL.min^{-1} of He passing through a water saturator (25 ^{0}C) was used to carry the steam (2.7 ml.min^{-1}).

XANES spectra at Ce L_3-edge (5723 eV) were measured at D04B-XAFS1 beamline of LNLS using a Si (111) channel cut monochromator. The measurements were done in transmission mode during reduction and WGS reaction. The reduction was done as described before recording XANES in the energy range 5628 to 5908 eV (7 min to each spectrum). The samples were cooled down to room temperature under H_2 where the gas atmosphere for WGS reaction was changed. Two different experiments using two different ratios between H_2O/CO were carried out to evaluate the influence of the amount of water. H_2O/CO ratio = 10 (described above) and also CO/H_2O = 3 was performed. For this, 100 mL.min^{-1} flow of 5%CO/He and 50 mL.min^{-}1 of He passing through a water saturator (60 ^{0}C) was used to carry steam (15 mL.min^{-1}). The samples were heated up to 400 ^{0}C in steps of 100 ^{0}C (5 ^{0}C.min^{-1}) remaining at each temperature for 60 min.

Ce K-edge (40443 eV) was also measured at BM23 beamline of ESRF using Si (311) crystal. The samples were prepared as pellets (using 300 mg for a jump of 0.35) and placed into a furnace for transmission measurements. The samples were reduced using the same conditions for Pt edge and XANES were recorded during the

heating ramp in the energy range 40,200 to 40,700 eV. Each spectrum took about 11 min. At 500 ^{0}C three EXAFS spectra were recorded in the energy range 40,000 to 41,550 eV (kmax = 20 Å^{-1}) what took about 50 min each one. The sample was cooled down to room temperature under H_2/He and EXAFS spectra were measured in the same energy range. After this, the gas atmosphere was changed for WGS reaction (ratio 10:1). The temperature was increased up to 250 ^{0}C where EXAFS measurements were done.

A scheme with the role apparatus used for the experiment is presented in Figure 5.

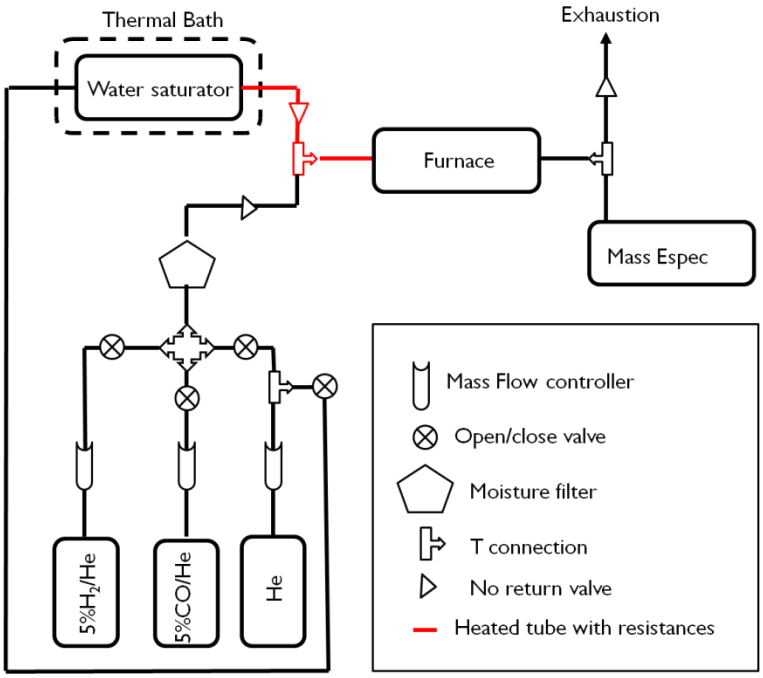

Figure 5. Experiment setup describing the gases, valves and other equipment.

I.5.3.5. X ray absorption data analysis

I.5.3.5.1. Background removal and normalization

The absorbance before the edge (pre-edge) is regressed by a line and a polynomial is regressed to the data after the edge. By default, at Athena software, a three-term (quadratic) polynomial is used as the post-edge line, but its order can be changed depending on the data. The normalization consists in scaling the absorbance to an edge step of 1 and the background above the edge. At Athena, the normalization constant, $\mu_0(E_0)$ is evaluated by extrapolating the pre- and post-edge lines to E_0 and

subtracting the E_0-crossing of the pre-edge line from the E_0-crossing of the post-edge line. This difference is the value of the “Edge step” parameter.

The pre-edge line is extrapolated to all energies in the measurement range of the data and subtracted from μ(E). This has the effect of putting the pre-edge portion of the data on the y=0 axis. The pre-edge subtracted data are then divided by $\mu_0(E_0)$ resulting in the normalized data.

For transmission measurements, any energy shift observed for the standard (that was measured simultaneously to the sample) was applied to the sample data. In the cases that were not possible to measure (in transmission) the sample and the standard simultaneously, when the sample absorbs too much, for example, the standard was measured immediately before and after the sample and any energy shift observed in the standard was applied to the sample. For the fluorescence measurements, once was not possible to measure the standard simultaneously, glitches at I_0 were used as an internal reference. All these procedures were done using Athena software.

I.5.3.5.2. Pt XANES data analysis

I.5.3.5.2.1. Linear combination analysis (LCA)

Using this method, the experimental spectrum is simulated by linear combination of reference spectra (or theoretical curves). To determine the number of variables to reproduce a spectrum, a “Principal Components Analysis” can be done [97]. In some cases (like our case, for Pt spectra) the spectra presents isosbestic points, showing that the first specie transforms to the new one without intermediates, it is possible to know that two species represent the experimental data. The LCA can be described by the equation:

$$XANES_{experimental} = x\,XANES_1 + (1-x)XANES_2$$

The LCA was done using the tool “Linear Combination Fitting” in Athena software. The experimental data for the Pt foil and PtO_2 were selected as standards. The fits were done in the range -20 to 30 eV relative to the edge. An example for the fit result is presented in Figure 6 with the weighted components (16% to Pt^0 and 84% to PtO_2) and the difference between the data and the fit.

It should be noted, however, that the values obtained for the percentage of Pt and PtO_2 species should not be taken as absolute values, since we used bulk references to fit nanoparticles and thus size effects introduce uncertainties to the analysis. Nevertheless, since the fits were done following the same procedure, a comparison among samples should be possible.

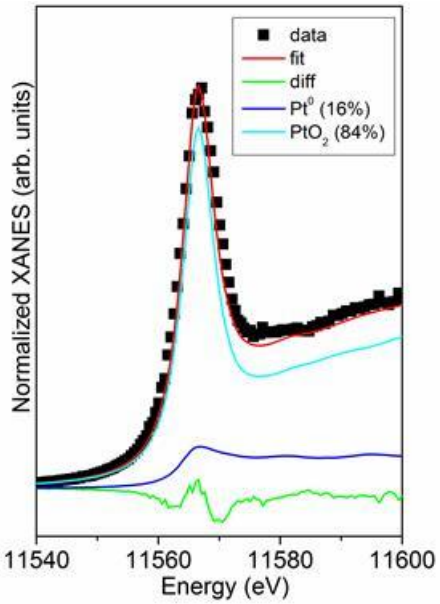

Figure 6. LCA result. Data (black squares), fit (red line), difference between the fit and the data (green line), Pt^0 and PtO_2 scaled proportional to the fit contribution (dark and light blue, respectively).

I.5.3.5.3. Pt EXAFS data analysis

As mentioned before, the structural parameters N_i, r_i and σ_i^2 can be extracted from the EXAFS signal. Thus, using a least-square approach, the difference between the experimental and modeled EXAFS function is minimized and the structural parameters are found. This can be done in k or R-space. The oscillations were Fourier-transformed within the limit k = 3-12 $Å^{-1}$. The local environment of the Pt atoms was determined using the phase shift and amplitude functions for Pt-Pt calculated for metallic Pt using the Atoms software [98]. The N_i, the effective half-path-length, R_i (which is equal to the r_i for single-scattering paths) and σ_i^2 were adjusted independently. Despite being possible to fit 11 parameters, independently, according Nyquist theorem and the range of data used in this work, to reduce the number of variables and the correlation between them we fixed the passive electron amplitude reduction factor (S_0^2) and photoelectron energy origin correction (ΔE_0) to those found for the metallic Pt.

Using the N_i found in the EXAFS data analysis, it is possible to estimate the particle size. Several models have been proposed in the literature [8], considering different particles geometries. One of the simplest is the spherical model [99] that relates the nanoparticle radius to the r and the N for the first coordination shell:

$$N_{nano} = \left[1 - \frac{3}{4}\left(\frac{r}{R}\right) + \frac{1}{16}\left(\frac{r}{R}\right)^3\right] N_{bulk}$$

Where,

N_{nano} = coordination number for the first coordination shell found experimentally;
r = interatomic distance for the first coordination shell found experimentally;
R = nanoparticle radius;
N_{bulk} = 12 for fcc Pt

Using the nanoparticle diameter (D) obtained by coordination number it is possible to calculate the Pt dispersion, which corresponds to the percentage of atoms at the surface related to the total amount. The total number of atoms (n) in a nanoparticle is the ratio between the nanoparticle volume and the atom volume (considering that the atom diameter is twice the Pt metallic ratio and equal to 1.38 Å):

$$n = \frac{D^3}{d^3}$$

The surface area of a spherical nanoparticle is πD^2. One atom at the surface contributes with $1/4*\pi d^2$ from this surface area that corresponds to the area projected at the surface thus, the number of atoms at the surface (N) is:

$$N = \frac{4D^2}{d^2}$$

The dispersion (Di), as mentioned, will be the ratio between the atoms at the surface and the total number of atoms:

$$Di = \frac{N}{n} * 100$$

I.5.3.5.4. Ce XANES data analysis

After normalization and background correction, where the photon energy origin was set at the maximum of the first derivative at edge region, a LCA was tried for spectra measured at Ce L_3-edge using CeO_2 and $Ce(NO_3)$ as Ce(IV) and Ce(III) standards, respectively. As can be seen in Figure 7(A) the fit quality was not good and it did not represent well the experimental data. To improve the analysis, another method called peak fitting was used [100] [101]. This method is preferable when instead of a band-structure (like Pt^0) the element presents molecular like-orbitals (like CeO_2) and the transitions could be represented by functions. In this case, the electronic transitions ($2p_{3/2}$ → 5d) related with the XANES at Ce L_3-edge could be represented with Gaussians functions (Figure 7(B)) [102] [103] [104] [105] [106] [107] [108]. Gaussian A corresponds to the delocalized d character at the bottom of the conduction band (2p → 5d). Gaussian B mainly corresponds to the amount of Ce^{3+} and is related with the transition 2p → $4f^1 5d e_g \underline{L}$. The Gaussians C is associated to the transitions *2*p → $4f^1 5d_{t2g} \underline{L}$. "$\underline{L}$" denotes the hole in the 2p shell and $5d_{eg}$ and $5d_{t2g}$ refers to the excited electron in the previously unoccupied 5d state [100]. Gaussian D and E are related with crystal field splitting 2p → $4f^0 5d$ [102] [103] [104] [105] [106] [107] [108]. Using this method the fit quality improves as can be seen in Figure 7(B).

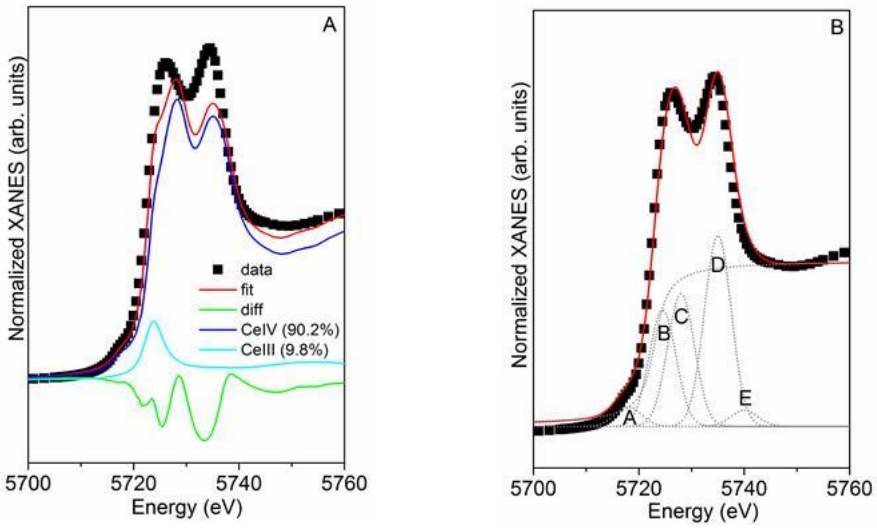

Figure 7. (A) Fit using LCA; (B) Fit using peak fitting method and Gaussians and Arc tan used to simulate the experimental curve.

The peak fitting procedure was done using WinXas 3.1 software where five Gaussians functions and one Arc tan [102] were considered. First, fits were done for Ce(III) and Ce(IV) standards, $Ce(NO_3)$ and CeO_2 respectively. For the standards analysis, the Gaussian width was kept constant as 6 eV except for B that 4 eV was used. The Arc tan width was also fixed as 6 eV and height as 1. The energy and height (maximum intensity) were adjusted for each Gaussian. The results for the Gaussian positions, obtained for the standards, are found in Figure 1 in Annex A.

To decrease the number of parameters, the energy position and width for the Gaussians were fixed (Table 2) and the height was adjusted. The total area of each peak is described as I_x (where x = A, B, C, D and E). The amount of Ce^{3+} was calculated using the relation between the areas according the equation (2) [109]:

$$[Ce^{3+}] = I_B * (I_B+I_C+I_D+I_E)^{-1} \qquad \text{(equation 2)}$$

Table 2: Fit constrains for Ce XANES analyses.

Gaussians					Arc tan		
Bond energy*(eV)					Bond energy(eV)	Width (eV)	Height
A	B	C	D	E	Maximum of the first derivative for each sample	6	1
-3	4	6	12	16			
Width (eV)							
A	B	C	D	E			
6	4-6**	6					

* Relative to the edge 5723 eV; ** constrained between these values. The Gaussians heights were left free.

I.5.3.5.5. *Ce EXAFS data analysis*

The EXAFS signal extraction was done following the same procedure for platinum using the Demeter software package [98]. For the samples where Ce was added to gel a multielectron excitation effect (MEE) [110] was observed, Figure 8(A). MEE is characterized by a peak superposed onto the smooth energy and is due to double excitations or shake-up transitions [111]. This peak [110] was removed using the function “multi-electron excitation removal” from Athena software [98]. The results in Energy and k-space can be seen in the red curves for the Figures 8 (A) and (B), respectively. The oscillations were Fourier-transformed within the limit k = 3-10 $Å^{-1}$. For both samples the photoelectron energy origin correction (ΔE_0) was determined using the spectrum after the reduction. The distances were fixed equal to 0 and ΔE_0 was

adjusted freely. Then both (distance and ΔE_0) were adjusted freely and the value found for ΔE_0 for the reduced sample was applied for the samples on the other conditions. For IMP samples the environment of Ce atoms was determined using the contributions of Ce-O and Ce-Ce calculated for a CeO_2 compound. The parameters Ni, Ri and σi^2, relative to each contribution, were adjusted freely. For the GEL samples two contributions of Ce-O at the first coordination shell were considered. Furthermore, for the samples after the reduction, to improve the fit quality, a Ce-Al contribution had to be included. All the parameters were fitted independently for each contribution except that for Ce-O contribution that the same σi^2 was used.

The passive electron amplitude reduction factor (S_0^2) found for CeO_2 reference was used and fixed in all cases.

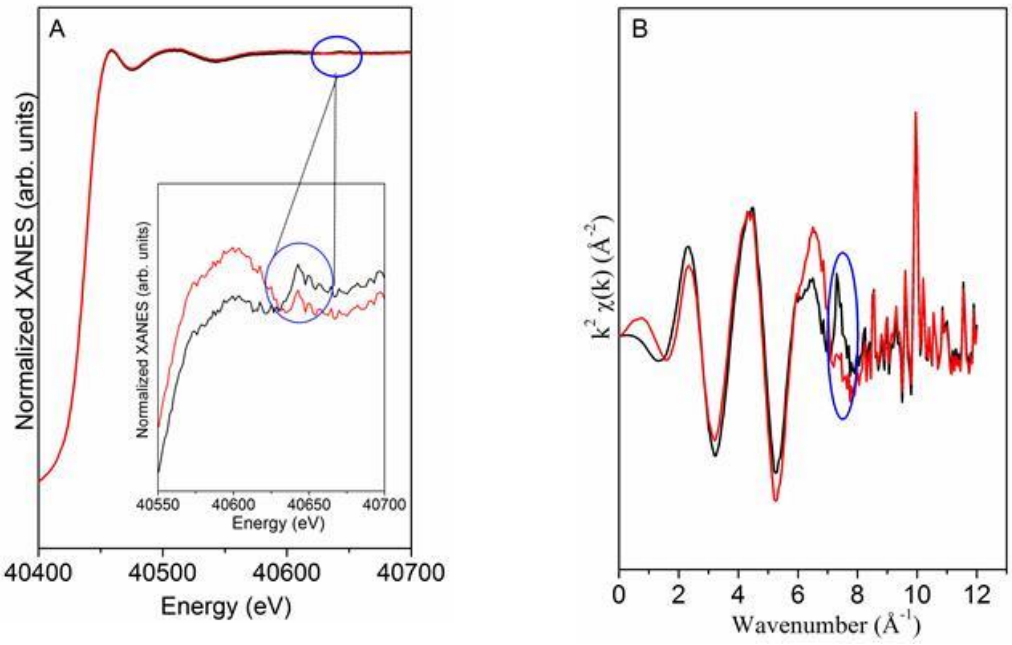

Figure 8. g-Pt12CeAl spectrum under WGS 250 ^{0}C (A) in energy and (B) k-space. Black curve shows the MEE and red curve is after the removal.

I.5.3.6. Fourier Transformed Infrared under WGS conditions

In situ diffuse reflectance infrared Fourier transform spectroscopy (DRIFTS) experiments were carried out in the same equipment described in FTIR-CO experiments. Prior to the reaction, the catalysts were reduced in 25%H_2/He at 500 ^{0}C for 60 min and treated with He for 60 min at the same temperature. The background spectra of the catalysts were taken under He flow at the desired reaction temperatures (200, 250, 300, 350 ^{0}C). Finally the samples were cooled down in He to 200 ^{0}C and

the reactant gas mixture (1%CO and 3%H_2O diluted in He) was fed into the cell. The steam was admitted into the cell by bubbling He through a saturator containing water at 25 ^{0}C. The total reactant flow was 100 mL.min^{-1}, which correspond to gas hourly space velocity (GHSV) of ca. 0.001 g.min.mL^{-1}. Then, the sample temperature was raised to 350 ^{0}C, at 50 ^{0}C intervals, and the FTIR spectra collected. Typically, 128 scans were taken to improve the signal to noise ratio with a resolution of 4 cm^{-1}. The outlet flow was analyzed with a Pfeiffer mass spectrometer.

I.5.3.7. Catalytic test

The WGS reaction was carried out in a fixed bed quartz reactor (i.e. 9 mm) under atmospheric pressure using 77 mg of the catalysts (100 mesh particles) diluted with quartz (123 mg). First, the samples were reduced at 500 ^{0}C, for 1 h under H_2 flow of 35 ml.min^{-1}. Then, the temperature was decreased to 200 ^{0}C under He (50ml.min^{-1}) where the reaction mixture was fed into the reactor. Two reaction mixtures compositions were used: 1:3 and 1:10 of CO: H_2O. The steam was introduced to the reactor by bubbling He through a saturator containing water at 65 ^{0}C. The ratio between catalyst mass and CO flow was kept constant (0.015 g.min.ml^{-1}), which corresponds to a total flow rate of 100 and 130 ml.min^{-1} for 1:3 and 1:10 ratios, respectively.

The effluent gas composition was analyzed by gas chromatography, employing a GC (Bruker 450) with thermo conductive detector (TCD) equipped with two columns of Porapak N and Molecular Sieve 13X in a series-bypass arrangement.

The equations used to calculate an “apparent” turn over frequency (TOF) are presented in Annex A.

I. 6. Results

We started by examining the samples textural and structural properties. Table 3 shows the catalysts surface area and CeO_2 crystallite size. The incorporation of Pt-NPs does not significantly affect the textural properties of the γ-Al2O3 [112] whereas adding cerium lead to a small decrease in surface area as previously reported [60] [59].

Figure 9a presents the diffraction pattern of PtAl before calcination corresponding to the boehmite precursor. Similar XRD patterns (not shown) were

obtained for all sample. Additionally, the incorporation of the Pt-NPs did not influence the support crystallinity (Figure 1 in Annex B presents the diffraction patterns for γ-Al_2O_3 and PtAl). Diffraction patterns after calcination are shown in Figure 9 (b)-(f) where the broad peaks of the poorly crystallized γ-Al_2O_3 phase could be identified for all samples (2θ = 31.7; 37.5; 45.7; 56.6; 60.7; 66.5; 84.6^0). The first three peaks of Pt^0 (2θ = 39.7; 46.2; 67.40) are superposed to γ-Al_2O_3 peaks. Thus it is difficult to evaluate if particle sintering is taking place. We found that Pt aggregation could be better confirmed by also evaluating the region at higher angles, by the analysis of the (311) Pt peak at 2θ = 81.20 (indicated by the dashed line in Figure 9) [112]. The clear lack of this reflection is an indication that the Pt-NPs were well dispersed in all samples, as described previously [112] [5].

Table 3. CeO_2 crystallite size, surface area

Sample	Surface area ($m^2.g^{-1}$)	CeO_2 crystallite size* (nm)
PtAl	282	Does not apply
g-Pt12CeAl	251	Not observed
g-Pt20CeAl	227	2
i-12CePtAl	234	4
i-20CePtAl	213	5

* From XRD data

Peaks corresponding to CeO_2 fluorite phase (2θ = 28.5°, 33.3°, 47.5° and 56.4°, marked by * in Figure 9f) could only be clearly observed in the i-20CePtAl sample, corresponding to a crystalline domain of 5.7 nm (Table 3). In the other samples, g-Pt12CeAl, g-Pt20CeAl and i-12CePtAl, the ceria phase lacks long-range order and only a broad feature corresponding to the main peak can be seen indicating that the diameter of the crystalline domains is smaller than 5 nm. However, a careful analysis indicates that ceria crystallinity increases in the order g- Pt12CeAl < g-Pt20CeAl < i-12CePtAl < i-20CePtAl, showing that both higher loadings and the impregnation method facilitate ceria crystallization. Using the Scherrer equation the CeO_2 crystallite size was estimated and is presented in Table 3.

Figure 10a shows the Pt L_3-edge XANES of i-20CePtAl in comparison with the Pt and PtO_2 standards (the data for the other samples are similar and not shown). The Pt-NPs became partially oxidized during the calcination process, as

evidenced by the intensity of the white line, indicated by the dashed line in Figure 10a. By heating under H_2, the total reduction of the Pt-NPs is achieved at about 500 °C.

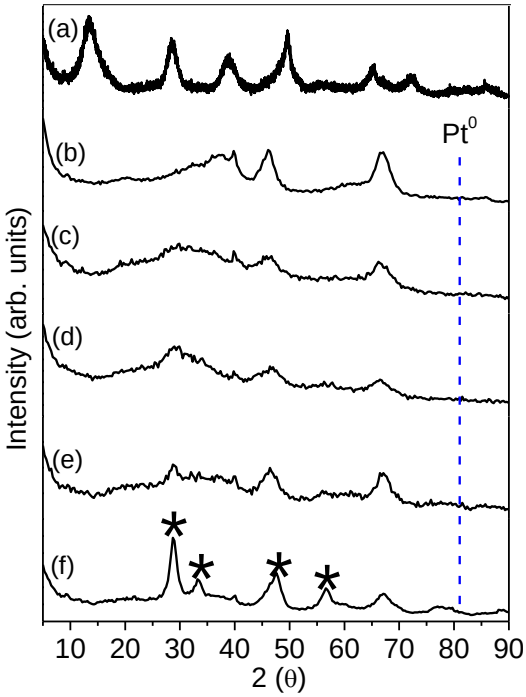

Figure 9. Diffraction patterns for the samples (a) PtAl before calcination (boehmite) and after de calcination: (b) PtAl; (c) g-Pt12CeAl; (d) g-Pt20CeAl; (e) i-12CePtAl; (f) i-20CePtAl. Peaks correspondent to (*****) CeO_2, blue line show the position where the Pt peak should appear if it was agglomerated.

The final spectrum does not fully correspond to the standard due to size effects and temperature. *In situ* XANES during reduction (XANES-H_2) is shown in Figure 10b for this sample. Isosbestic points can be seen, showing that the transition from the oxidized to the metallic phase occurs without intermediate species and the Pt-NPs are fully reduced after this process. Figure 10c shows the evolution of the Pt oxidation state during the reduction for all samples. The first point in Figure 10c corresponds to the samples just after the calcination and it can be seen that the PtAl is less oxidized (53% Pt°) than the samples containing Ce. Comparing the samples containing Ce, the GEL samples are more oxidized (16 and 20% Pt° for g-Pt12CeAl and g-Pt20CeAl, respectively) than the IMP samples (32 and 27% Pt° for i-12CePtAl and i-20CePtAl, respectively). Platinum oxidation was observed [113] when it is deposited on a CeO_2 (111) surface due to the spontaneous reduction of the substrate facilitating the formation of vacancies and thus the change of the cerium oxidation state in the vicinity of Pt from Ce^{4+} to Ce^{3+}. Thus, the Ce presence contributes to further

oxidize the sample and probably the Pt-Ce interaction is stronger when Ce was added to gel. Thus, despite having synthesized a metallic nanoparticle the calcination process led to the particle oxidation. A reduction was carried out, before the reaction, since increasing the Pt electron density would facilitate the reaction with CO (through π-back donation) [114]. As mentioned before, the PtAl sample is ~50% reduced after calcination (i.e., 50% Pt°) while for the samples with Ce, the temperature needed to achieve this degree of reduction was 209 °C for g-Pt12CeAl, 231 °C for g-Pt20CeAl, 113 °C for i-12CePtAl and 165 °C for i-20CePtAl. In addition, PtAl is completely reduced at 321 °C while the samples containing Ce reduce only at 500 °C. Once again, it is much easier to reduce the sample without Ce and the samples where Ce was impregnated than the samples where Ce and Pt were added to the gel. As observed for the spectrum before the reduction, the spectrum after the reduction does not match perfectly with the Pt^0 standard (Figure 10a, blue curve) due to the particle size effect in the white line intensity.

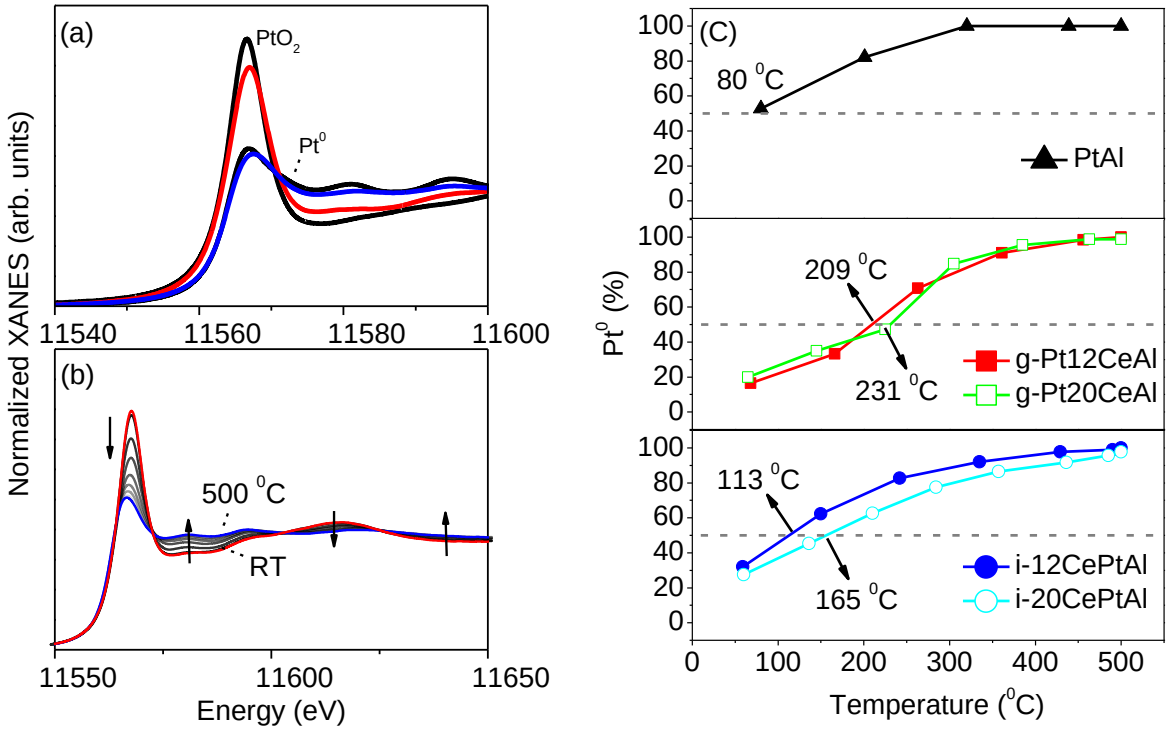

Figure 10. (a) Comparison between the Pt^0 and PtO_2 standards and the sample at the beginning and at the end of reduction. (b) Temperature-resolved XANES-H_2 at Pt L_3-edge for i-20CePtAl. (c) Pt species quantification obtained by linear combination between Pt^0 and PtO_2: PtAl (black triangles), g-Pt12CeAl (red squares), g-Pt20CeAl (green empty squares), i-12CePtAl (blue circles), i-20CePtAl (blue empty circles).

Figure 11 presents the Pt L_3 edge EXAFS and the best fits for PtAl after the reduction (g-Pt12CeAl and i-12CePtAl are presented in Figure 2, Annex B). Damped coordination shells above 3Å were observed, as expected for nanoparticles (Figure 11). The fit results are in Table 1 in Annex B. They are very similar among samples after reduction, independently of the Ce presence or incorporation method. Thus, the similarity achieved due to the fact that the catalysts were prepared from the same batch of colloidal nanoparticles was not affected and still the same. XANES at the end of reduction showed that the samples were completely reduced and the EXAFS data could be reproduced with only Pt-Pt contribution.

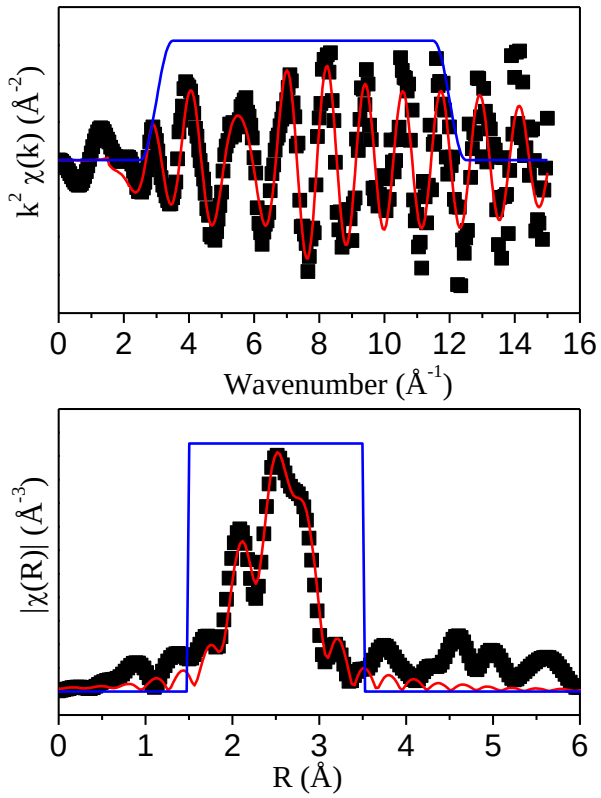

Figure 11. EXAFS data and fit at k space and magnitude of the Fourier transform for PtAl after the reduction at room temperature. Black squares (data); red line (fit) and blue line (window).

The coordination numbers obtained were 6.0 ± 1.0 (1st coordination shell of Pt-Pt) that can be used to estimate particle shape/size. Different models have been proposed in the literature [24, 36]. Using the spherical model [79], the particles show mean diameter of 0.8 nm for all samples.

Contraction of Pt-Pt distances ($\Delta R_{Pt\text{-}Pt}$) > 0.1Å is expected for small particle sizes [115, 38]. Our results showed a contraction of 0.01-0.02 Å with respect

to bulk fcc Pt. This contraction observed in our samples is similar to Pt catalysts supported on zeolites [116] and is explained due to chemisorbed hydrogen, which increases the delocalization of electrons increasing bond distances [117] since the measurements were done under hydrogen atmosphere.

Since XAFS is a bulk technique to evaluate the catalysts surface FTIR spectra with CO adsorption and XPS measurements were carried out. While FTIR-CO provides indirect information about the exposed Pt sites and Pt electronic density through the modification of CO stretching bands (linear, bridge, 3-fold), XPS provides direct information on the surface chemical composition and electronic state.

FTIR-CO measurements were collected in the 2300–1700 cm^{-1} region, (Figure 12) to probe the interaction of CO molecules with Pt surface atoms. All spectra (Figure 12a) exhibited a main band at high wave number at about 2077 cm^{-1} assigned to CO linearly bonded on higher coordination Pt sites and a tail at low frequencies. The main band at 2077 cm^{-1} shows a slight red shift for the catalysts promoted by ceria, but is within experimental error (4 cm^{-1}). It is known that lateral interactions can significantly shift band positions [118], but detailed studies have also associated the signal in the ~2050–2010 cm^{-1} region with the adsorption of CO on smaller Pt NPs or Pt defects sites (corners and edges) in a linear mode [118] [119] [120] [121]. It is worth to note that the PtAl catalyst also show in the low wavenumber region, a pair of overlapping bands at 1820 and 1766 cm^{-1}. The band at 1820 cm^{-1} is associated with CO bonded to two Pt atoms in bridge form whereas the band at 1766 cm^{-1} is assigned to CO bonded to Pt species in tridentate mode [118] [5]. In the presence of ceria, the adsorption of these species, become unfavorable due to the decrease of the Pt electronic density or the presence of patches of ceria on the Pt surfaces [118] [5].

Since the full width at half maximum (FWHM) for linear CO is sensitive to the particle size distribution of the Pt clusters, this value was very close (about 34 cm^{-1}) for all samples, confirming the presence of particles with similar size.

XPS measurements were performed before and after the reduction. The results are shown in Table 4. All calcined samples present Pt 4d5/2 BEs closer to PtO_2 (316.8 eV) than Pt^0 (313.6 eV) [122]. These high BEs confirm partial oxidation of the Pt-NPs during catalyst preparation and/or an important interaction with the support. The XPS results are in agreement with the XAFS data presented before. After reduction, all samples present a slight decrease in the Pt 4d5/2 BEs but the values are

still higher than the BE of the metallic Pt. This effect is more pronounced in the ceria-promoted catalysts, in agreement with Riguetto et al. [118]

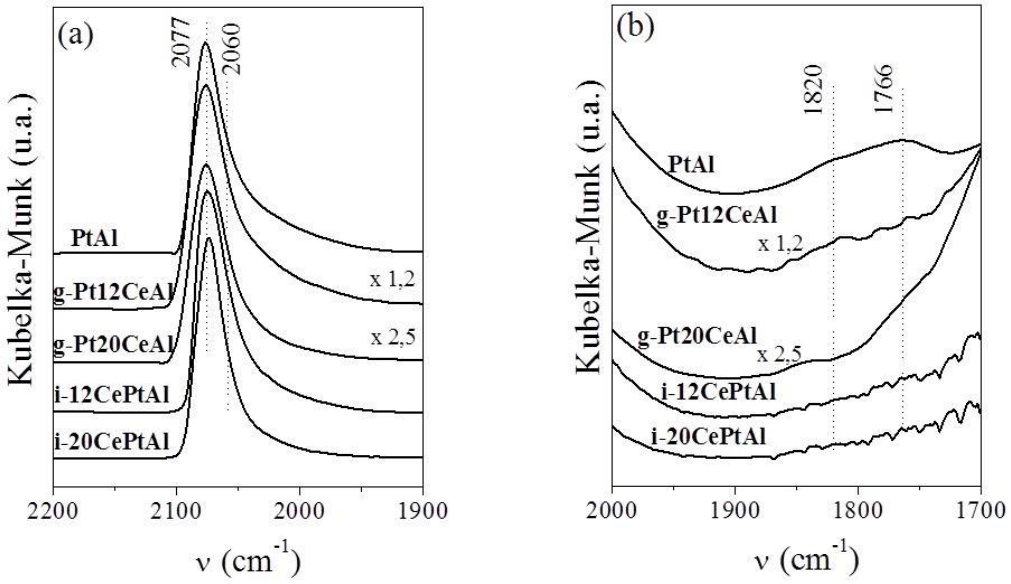

Figure 12. DRIFT spectra of adsorbed CO after catalyst reduction.

The surface atomic compositions are similar for all catalysts, according to Table 4. The Pt surface concentration is quite small and corresponds to about 12% of the total Pt concentration. This was expected considering that the Pt-NPs are embedded in the oxide matrix. A slight variation of Ce surface concentration was found when comparing GEL and IMP samples of same bulk concentration (12 or 20%). In general, the IMP samples show smaller Ce surface concentrations, compared to the corresponding GEL samples, which is in accordance with the stronger segregation and crystallization of CeO2 in the IMP catalysts, as indicated by XRD in Figure 9.

The percentage of Ce^{3+} at the surface can be calculated through a relation between the components used to fit the spectra: $[Ce^{3+}]=[(A_{u'}+A_{v'})/(A_{u'''}+A_{u''}+A_{u'}+A_u+Av'''+Av''+A_{v'}+A_v)]$, where A is the area of each component [123,124]. The reductive treatment leads to a slight increase of Ce surface concentration for most of the samples. The atomic percentages of Ce^{3+} at the surface are also presented in Table 4. Thus, ceria reduction was promoted by the Pt presence through a hydrogen spillover decreasing the reduction temperature [33, 34]. Confirming this, a higher amount of non-reduced ceria was found for the support (not shown) when the reduction was carried out up to 500 ^{0}C.

Thus, after evaluate changes for platinum due to the cerium presence the cerium properties were further evaluated, XAFS spectra at Ce L_3-edge were collected.

Table 4: Binding energy (BE) for Pt $4d_{5/2}$, atomic surface composition before (B) and after (A) reduction and $\%CeO_2$. The values in brackets correspond to the percentage relative to the total amount.

Samples		BE (eV)	%Concentration				%[Ce^{3+}]
		Pt $4d_{5/2}$	O	Pt	Al	Ce	
PtAl	**B**	315.1	60.4	0.1 (7)	39.5	-----	-------
	A	314.6	57.5	0.1 (7)	42.4	----	-------
g-Pt12CeAl	**B**	316.0	60.6	0.1 (7)	38.0	1.2 (10)	31
	A	315.1	57.6	0.1 (7)	40.9	1.4 (12)	38
g-Pt20CeAl	**B**	315.8	58.8	0.1 (7)	39.1	2.0 (10)	34
	A	315.3	57.9	0,1 (7)	39.9	2.0 (10)	39
i-12CePtAl	**B**	315.6	59.6	0.1 (7)	39.4	0.8 (7)	37
	A	314.8	60.1	0.1 (7)	38.9	1.1 (9)	40
i-20CePtAl	**B**	316.2	63.8	0.1 (7)	34.8	1.3 (7)	25
	A	315.1	60.9	0.1 (7)	37.4	1.6 (8)	32

* BE for Pt^0 = 313.6 eV and PtO_2 = 316.8 eV.

The electronic transitions related with the XANES at Ce L_3-edge can be described with Gaussian functions, as explained before. In a general way there is a particle size dependence related to the features: peaks B and D (Figure 13a) became larger, the intensity of peak B slightly increases while peak D became less intense and both peaks shift toward lower energy smaller the particle is. Thus, changes in the intensity and position of features B and D can be explained by an enhanced contribution of cerium atoms situated on the NP surface and having a different local environment compared to the bulk atoms [126]. However besides size effects these features are also related with oxidation state as discussed below.

Figure 13a shows the initial spectrum of the calcined g-Pt20CeAl and the best fit. The most pronounced features (C and D for this sample) are characteristic of CeO2 and the slight difference in the relative intensities compared to the bulk standard (Figure 13b) are probably related to nanometric effects. Figure 13b shows the spectra evolution during reduction for g-Pt20CeAl catalyst (similar for the other ones). By increasing the temperature under H_2, the features C and D decrease and feature B

increases, corresponding to the transition from Ce^{4+} to Ce^{3+} [126]. Using the areas of the Gaussians, the amount of Ce^{3+} / Ce^{4+} in the samples during the reduction was calculated. The evolution of the cerium oxidation state (as Ce^{3+}) for all catalysts is shown in Figure 14. At the beginning, all the samples have about 20% of Ce^{3+} except for i-20CePtAl that presents about 30%, probably due to the formation of larger crystallite size and species that are not easily reduced (as observed by XRD, Figure 9). Samples g- Pt12CeAl, g-Pt20CeAl and i-12CePtAl present similar behavior and at the end of the reduction the amount of Ce^{3+} increases to 42%. The sample with the larger CeO_2 crystalline domain, i-20CePtAl, does not significantly change its overall oxidation state.

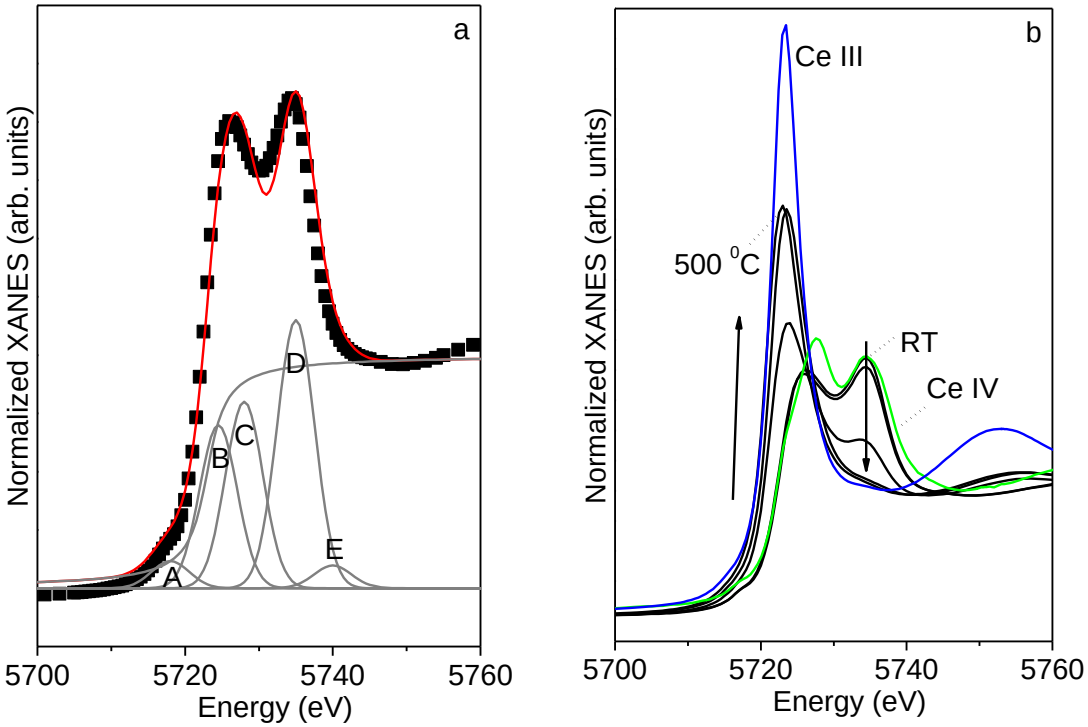

Figure 13. (a) XANES at Ce L_3-edge before the reduction (room temperature) for the sample g-Pt20CeAl (squares) and the best fit (red line) obtained using Gaussians and arc tan functions corresponding to Ce electronic transitions (gray curves). Squares: data; black line: fit. (b) Temperature-resolved XANES during the reduction at Ce L_3-edge for g-Pt20CeAl and Ce(III) (blue line) and Ce(IV) (green line) standards.

The presence of Pt leads to ceria reduction at lower temperature, since the reduction is not observed for the support (not shown) as observed for the XPS results due to the metal ability to dissociate hydrogen [127].

Comparing the XANES and the XPS results, before the reduction, the surface is more reduced than the bulk for the samples g-Pt12CeAl, g-Pt20CeAl and i-

12CePtAl. For the sample i-20CePtAl the percentage of Ce^{3+} at the surface and the bulk are quite similar (25 and 30%, respectively). At the end of the reduction an increase for Ce^{3+} at the surface was observed for all samples and the amount of Ce^{3+} at the surface and in the bulk becomes quite similar (about 40% for all samples except for i-20CePtAl that presented 30%).

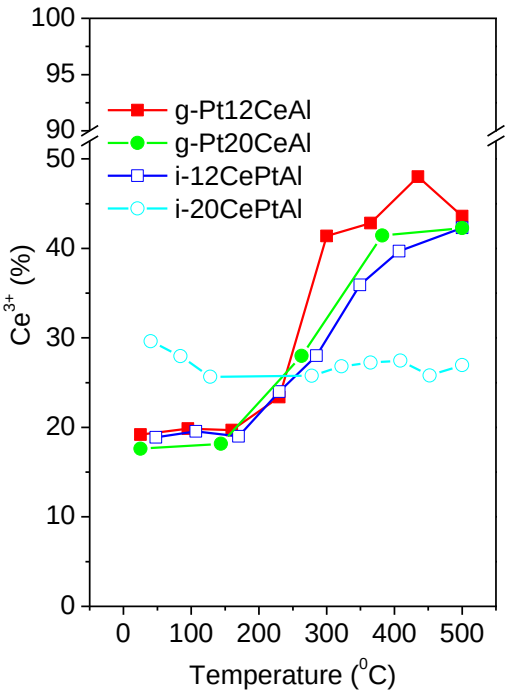

Figure 14. Ce species quantification, during reduction, obtained by fits using functions corresponding to electronic transitions. g-Pt12CeAl (full red squares), g-Pt20CeAl (full green circle), i-12CePtAl (empty blue square), i-20CePtAl (empty blue circle).

Ce K-edge EXAFS was performed for g-Pt12CeAl and i-12CePtAl after calcination, under H2 at 500°C, and after cooling down under H_2 at room temperature. EXAFS data under WGS at 250 °C were also obtained. Figure 15 presents the magnitude of the Fourier transform at the Ce K-edge for each catalyst after calcination and after reduction. The contributions used in each fit are also indicated in Figure 15 and fit results are presented in Table 5 and 6. EXAFS data and corresponding fits for these two samples under all conditions are presented in Figure 3, Annex B and the results are presented in Tables 2 and 3 (Annex B).

From the structural parameters presented in Table 5 and 6, it is possible to observe that both samples show a significant attenuation of the oscillations compared to the CeO_2 standard due to the small crystallite size and/or higher degree of disorder. Comparing both samples, i-12CePtAl is clearly more ordered than g-

Pt12CeAl since the Ce-Ce contribution is visible at ~ 3.8 Å (but with N_{Ce-Ce} much smaller than the CeO_2 standard). For the CeO_2 standard, the first coordination shell corresponds to 8 O neighbors at 2.34 Å [ICSD Coll Colde: 156250]. For the samples, however, it was necessary to include two Ce-O contributions, one at about 2.25 Å and another at 2.40 Å, that indicate that Ce bounds to different species at the surface or at the interface with alumina. After reduction, the Ce environment seems to become more disordered and a Ce-Al contribution (3.27 Å) appears.

Table 5: Structural parameters obtained from EXAFS analysis of g-Pt12CeAl before and after the reduction at RT.

	Calcined	H_2 25 $^0C^{(a)}$
N_{Ce-O1}	3 (± 1)	3 (± 1)
R_{Ce-O1} (Å)	2.10 (± 0.03)	2.20 (± 0.05)
N_{Ce-O2}	3 (± 1)	4 (± 1)
R_{Ce-O2} (Å)	2.3 (± 0.02)	2.40 (± 0.05)
N_{Ce-Al}	--	3 (± 8)
R_{Ce-Al} (Å)	--	3.7 (± 0.1)
σ_{Ce-O}^2 / σ_{Ce-Al}^2 (Å)	0.005 (± 0.008)	0.001 (±0.006) /0.01 (± 0.03)

(a) after reduction; E_0 = -15 (± 5), S_o^2 = 0.9.

Table 6: Structural parameters obtained from EXAFS analysis of i-12PtCeAl before and after the reduction at RT

	Calcined	H_2 25 $^0C^{(a)}$
N_{Ce-O1}	9 (± 2)	7 (± 2)
R_{Ce-O1} (Å)	2.29 (± 0.02)	2.33 (± 0.01)
N_{Ce-Ce}	4 (± 3)	2.3 (± 0.8)
R_{Ce-Ce} (Å)	3.81 (± 0.02)	3.80 (± 0.02)
σ_{Ce-O}^2 / σ_{Ce-Ce}^2 (Å)	0.01 (± 0.003) / 0.005 (± 0.002)	0.01 (± 0.005) / 0.005 (± 0.002)

(a) after reduction; E_0 = -9 (± 2), S_o^2 = 0.9.

Ceria amorphization and the formation of aluminates have been reported for treatments at high temperature [128] [129]. The amorphization of ceria nanoparticles deposited on silica has been observed at temperatures around 500 ^{0}C during prolonged heating in hydrogen [128]. The formation of ceria aluminates has

been observed at 600 ^{0}C when Ce is dispersed on alumina surfaces and higher temperature (800 ^{0}C) for nanoparticles [129]. In our case, the aluminate formed at lower temperatures is due to the fact that the Ce was added to the alumina gel during the synthesis. Alayoglu et al. [130] found for Pt/CeO_2 catalysts bond distances for Ce-O contribution between 2.31 – 2.33 Å, depending on the atmosphere (hydrogen or oxygen). They observed that the CeO_2 crystalline structure is dynamic in the presence of platinum and vary depending on the atmosphere conditions (oxidative or reductive). Furthermore they correlated the Ce-O contribution with the oxygen vacancy formation. Thus our results probably indicate the presence of vacancies on our samples that are further increased after the reduction.

The structural differences between the two samples is also reflected in the different values found for ΔE_0 (-9 and -15 for i-12CePtAl and g-Pt12CeAl, respectively). Further the different structures these differences could be related with the approximations used to calculate the core hole potential by FEFF. The absorption edge is also different from the CeO_2 standard (ΔE_0 = -5). Thus, it was necessary to shift the theoretical E_0 to reproduce the spectra. This larger values have already been obtained for high energy edges, such as the Ce K edge [131].

Comparing the coordination numbers under H_2 small variations were observed for both samples while a small increase of Ce-O contribution was observed under WGS.

Several works have proposed that ceria OSC impacts directly the catalytic activity by facilitating the water activation [132] [133] [134]. Aspects that may enhance or reduce the ceria OSC are: ceria surface area [135], contact between the metal and the ceria [136] [137], crystallographic orientation and defects. It has been proposed that oxygen is more easily removed from high defect surfaces and small crystallites [135] [138]. For both set of samples, GEL and IMP, the OSC increases with the Ce-loading (73 and 116 µmol $O_2 \cdot g_{catalyst}^{-1}$ for the g-Pt12CeAl and g-Pt20CeAl, and 79 and 92 µmol $O_2 \cdot g_{catalyst}^{-1}$ for i-Pt12CeAl and i-Pt20CeAl, respectively; at 300 °C, Table 7). Interesting, comparing the samples prepared by the same method, the smaller amount of ceria (12%wt) leads to higher OSC per gCeO_2.

Wang et al [95] carried out OSC measurements at 300 °C in ceria nanomaterials with different shapes and found values from 128 up to 427 µmol O_2. g^{-1}. Considering that they synthetized ceria bulk and our catalysts are just 12 or 20% of

ceria, we can compare their results with our results relative to mass of ceria, also presented in Table 7. It is possible to observe that our materials even with a small amount of ceria (compared to a bulk material) present a high OSC due to the small crystalline domain. Considering that the GEL samples presented the same amount of Ce at the surface (according XPS results, Table 4), is possible to observe that smaller the crystalline domain larger the OSC. Comparing the samples with 12% of cerium the amount of Ce at the surface and the OSC results are similar. The sample i-20CePtAl, due to the bigger crystalline domain, presented a smaller amount of Ce at the surface as a smaller OSC result. The OSC for temperatures below 200 ^{0}C are similar for all the samples and less than 80 µmol O_2. g^{-1}. From the XANES results it is possible to observe that for temperatures below 200 ^{0}C there is a higher amount of Ce^{4+} than Ce^{3+}.Considering that due to the re-oxidation the sample goes back to the oxidation state, achieve during the reduction, this higher amount of Ce^{4+} probably is decreasing the OSC.

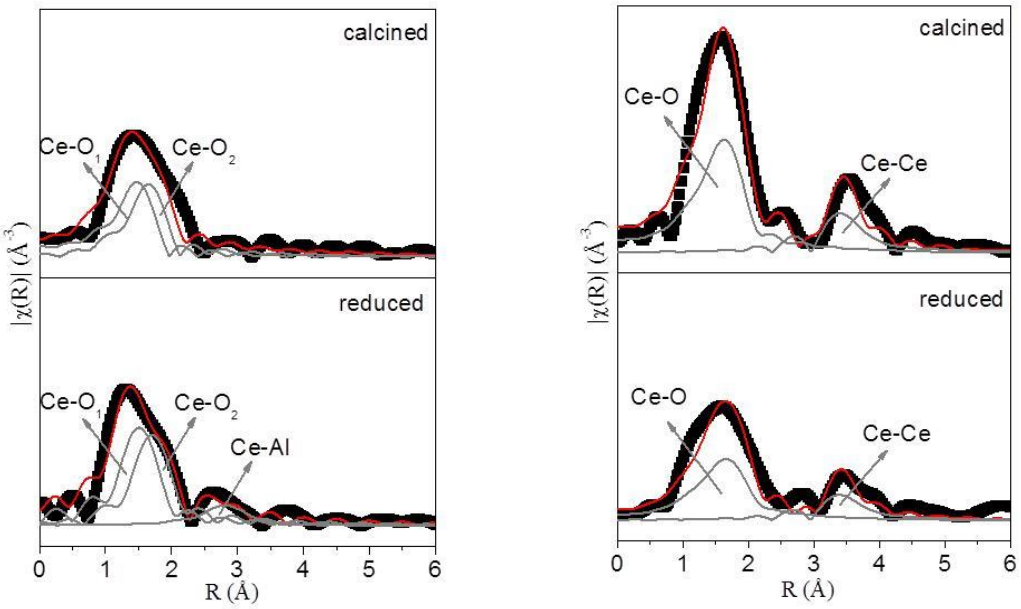

Figure 15. Magnitude of the Fourier transforms for (a) g-Pt12CeAl (b) i-12CePtAl.

Figure 16 shows the catalytic results under WGS as a function of temperature for H2O:CO ratios of 10:1 and 3:1. The conversion below 200 ^{0}C is very small most likely due the presence of PtO_x on the surface preventing H_2 dissociation. Further at this temperature there is a strong CO adsorption poisoning the catalyst. Additionally, ceria is not reduced what can make the reaction even more difficult. At

higher temperatures platinum and ceria becomes reduced [139] decreasing CO adsorption strength. The CO conversion is higher for the samples with Ce compared with the sample PtAl for both H_2O:CO ratios.

Table 7: Oxygen storage capacity at 300 ^{0}C.

Samples	OSC (μmol O_2. g^{-1})*	OSC (μmol O_2. g_{CeO2}^{-1})*
g-Pt12CeAl	73	608
g-Pt20CeAl	116	580
i-12CePtAl	79	658
i-20CePtAl	92	460

* 5% error.

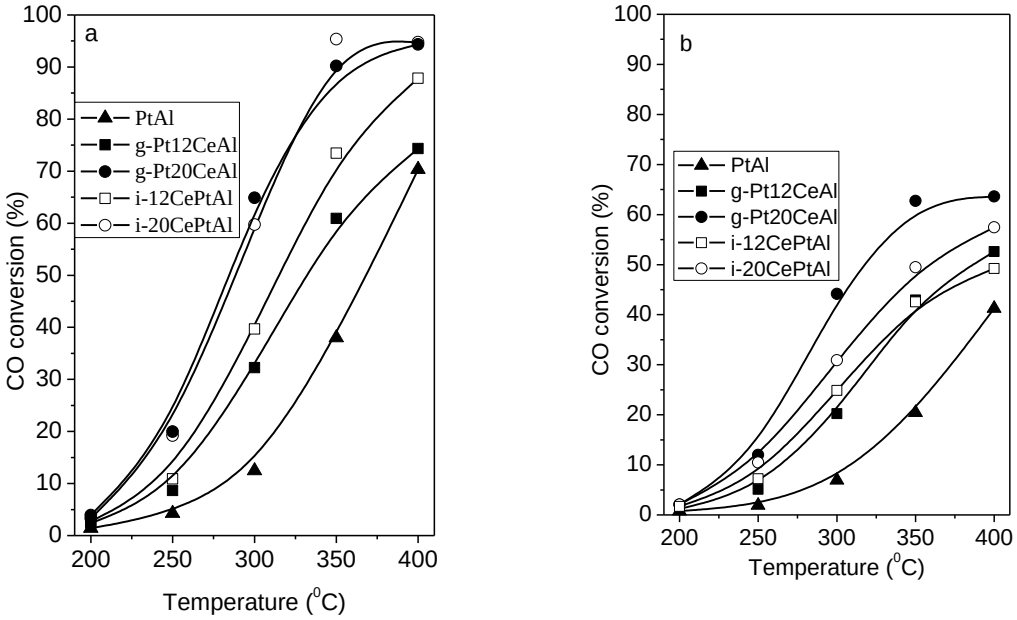

Figure 16. WGS reaction catalytic test (a) H_2O:CO ratio 10:1; (b) H_2O:CO ratio 3:1.

WGS specific reaction rate results are presented in Table 8. The presence of Ce increases the specific reaction rate in all samples, by a factor up to seven compared to PtAl, depending strongly on the ceria contents an temperature. It becomes clear that ceria plays a more important role at 250 °C. The increase of cerium from 12 to 20 wt%, for both set of samples (GEL and IMP) and both H_2O:CO ratios, roughly doubles the specific reaction rate. In addition, increasing the H_2O:CO ratio from 3:1 to10:1 has a similar effect since the reaction order is positive to water and larger than the reaction order to CO, for the reaction over a Pt surface [140] [33]. It is important to remark that the specific reaction rates and turnover frequencies values are significantly affected by the reaction conditions, metal dispersion and metal-

support interaction and several values can be found in the literature [64] [33] [32]. Several examples from the literature are given in Table 9 illustrating these differences.

Table 8: WGS average specific reaction rates ($mol_{COconv}\ g_{metal}^{-1}\ s^{-1}$) at 200 and 250 °C for both H_2O:CO ratios.

Samples	Rate at 200 °C (×10^5)		Rate at 250◦C (×10^5)	
	10:1	3:1	10:1	3:1
PtAl	3.9	2.3	12	5.7
g-Pt12CeAl	7.2	3.6	28	16
g-Pt20CeAl	12	6.2	75	42
i-12CePtAl	8.3	5.1	36	23
i-20CePtAl	10	6.3	71	36

Table 9: TOF results from the literature using different reaction conditions.

Reference	Sample	Condition	TOF (s^{-1})
Phatak et al. [33]	1.66%Pt/Al_2O_3 (69% of metal exposed)	200 ^{0}C	0.0011
Phatak et al. [33]	1%Pt/CeO_2 (28% of metal exposed)	200 ^{0}C	0.0414
Panagiotopoulou et al. [141]	0.5%PtCeO_2 (46% of Pt dispersion)	250 ^{0}C 3%CO and 10%H_2O	0.55
Vignatti et al. [142]	0.4%Pt/CeO_2 (37% of Pt dispersion)	3%CO and 3%H_2O	0.4
Zalc et al. [143]	1.5%Pt/CeO_2	300 ^{0}C 200 ^{0}C	0.2 0.04
Aranifard et al. [32]	1%Pt/CeO_2	P_{CO} = 0.07, P_{CO2} = 0.085, P_{H2O} = 0.22, P_{H2} = 0.37 atm, 200 ^{0}C	0.0414
Aranifard et al. [32]	1%Pt/CeO_2	P_{CO} = 0.1, P_{CO2} = 0.1, P_{H2O} = 0.2, P_{H2} = 0.4 atm, 300 ^{0}C	0.2

The effect on the reaction rates due to the metallic phase and the support are controversial. It is claimed that the reaction rates do not depend on the morphological characteristics of the metallic phase but only on the amount of the exposed surface metal atoms for structure insensitive reactions [144], [145]. However changes were observed evaluating theoretically $Pt_8/CeO_2(111)$ and $Pt(111)/CeO_2$ [86] [36] concerning the ability of small particle sizes to dissociate water. Support surface area and/or support crystallite size has been shown to be very important in some works [144] [45] while they had no effects for a certain range of ceria crystallite size [16] on others. The main point is that the correlation among the parameters is very strong. For example, the support reducibility depends on the crystallite size that changes the type,

number, density and reactivity of surface groups [144] [146][136][147]. Furthermore, there is the contact between the metallic particle and the support. Thus it is better not to use the reaction rates absolute values but as a comparative result between the samples measured at the same conditions.

Considering the structural characterization under WGS reaction conditions, no changes with respect to the corresponding reduced samples are observed at the Pt L_3-edge XANES (not shown). Also, no modifications of the Ce environment under WGS are detected by Ce K-edge EXAFS (Figure 3 and Tables 2 and 3, Annex B). The quantification of Ce^{3+} from Ce L_3-edge XANES taken at 300 °C is shown in Table 10 (within 5% estimate error). Similar values are found for the measurements done at 200, 300 and 400 °C. For H_2O:CO = 10:1, g-Pt12CeAl and g-Pt20CeAl are more reduced under WGS than at the end of the reduction, i- 12CePtAl is more oxidized and i-20CePtAl remains constant. On the other hand, for H_2O:CO = 3:1, the GEL samples are more oxidized while i-12CePtAl is more reduced. Therefore, no straightforward trend could be found among the samples. The constant oxidation state of Ce under reaction conditions at different temperatures, similar to what happened to Pt, indicates that only modifications at the surface might be happening with the temperature, not detected in these measurements.

Table 10: Amount of Ce^{4+} (%) at different reaction conditions (5% error) obtained from XANES analysis.

	WGS reaction	
	Ratio 10:1	**Ratio 3:1**
g-Pt12CeAl	45	65
g-Pt20CeAl	55	75
i-12CePtAl	62	53
i-20CePtAl	74	--

*the oxidation state did not vary with the reaction temperature.

To probe the evolution of surface species during WGS, *in situ* DRIFTS was performed. Under reaction conditions, vibrational modes of hydroxyls (3600–3000 cm^{-1}), formates (2900 cm^{-1}, 1650–1350 cm^{-1}), carbonates and carboxylates (1700–1000 cm^{-1}), as well as Pt-CO bands (2100-1950 and 1820–1766 cm^{-1}) are observed for all samples [148]. These bands are presented in Figure 17 for PtAl (A) and i-20CePtAl (B). A set of similar bands to i-20CePtAl is observed for the other samples containing cerium. The band at about 2060 cm^{-1} is assigned to the CO adsorption on

Pt sites in the linear mode. Compared to FTIR-CO (Figure 12), this band is significantly shifted under reaction conditions mainly due to the higher temperature (> 200◦C) and consequently lower CO coverage fraction (of about θ_{CO} = 0.27). In addition, under reaction, besides CO, other species such as H, O and OH might be adsorbed at the Pt surface [149]; these species are predominantly σ bonded and would decrease the electronic density at Pt surface contributing to the band shift to lower frequencies.

The overall widths of the CO adsorption bands are also slightly broader under WGS compared to FTIR-CO experiments (Figure 12). As in the case of FTIR-CO measurements (Figure 12), there are other two bands in the low frequency region (1820 and 1766 cm^{-1}) for the PtAl sample (Figure 17A). These bands remain constant even with the temperature increase. On the other hand, these bands are observed under reaction conditions at 200 °C but not under CO atmosphere for the i-20CePtAl sample (Figure 12). This indicates that the formation of Ce-O-Pt adducts, which hinders the adsorption of CO multi-coordinated, is apparently less effective under reaction conditions. Furthermore, in the i-20CePtAl, these bands wash out by increasing the temperature. The broad band at 3600–3000 cm^{-1} confirms the presence of asymmetric and symmetric stretching of OH vibration of water molecules on the surface. Bands associated with formates and carbonates species are clearly observed for i-20CePtAl at 1594, 1394 and 1375 cm^{-1} [148]. In addition, a low intensity pair of bands is observed at around 2900 cm^{-1}, which confirms the presence of CH bond associated to formates. For PtAl, these bands appear just above 300 °C. Thus, the cerium presence leads to the formation of formates at the catalyst surface at low temperatures. For i-20CePtAl, above 250 °C the appearance of adsorption modes of CO_2 in 2364 and 2322 cm^{-1} confirms the progress of the WGS reaction. For PtAl, this set of band appears above 300 °C confirming the higher reactivity for the samples with Ce as observed for the catalytic test. At 350 °C there is a decrease in the intensity of symmetric and asymmetric stretching modes of water, suggesting desorption of these species at higher reaction temperature. For i-20CePtAl there is an increase in intensity of the bands at 1594 and 1394 cm^{-1} with increase of temperature from 200 to 250 °C (Figure 17b). This result indicates the CO oxidation forming stable formates and carbonates that accumulate on the surface. At 300 °C there is a decrease in the intensity of formates bands at 2090 and 1594 cm^{-1}, suggesting the decomposition of these species

at higher reaction temperature, while for PtAl catalyst this species seems stable at higher temperature.

To get further information on the interaction of CO in the absence and presence of water, the samples were subsequently analyzed by closing and opening the water inlet at 350 °C, after being submitted to WGS conditions. Figure 18 shows the results for the samples PtAl (A) and i-20CePtAl (B). While CO_2 bands (2364 and 2322 cm^{-1}) decrease with time in the absence of water, formate and carbonate (2900, 1594 and 1375 cm^{-1}) and Pt-CO (2060 cm^{-1}) bands remain almost constant. The results demonstrate that in absence of H_2O (Figure 18 A-b,c,d and B-b,c,d), formates accumulate by CO oxidation on both supports, alumina and ceria-alumina, and are very stable [150]. The water is turned on again and the CO_2 band reappear at the surface (Figure 18A-e and B-e).

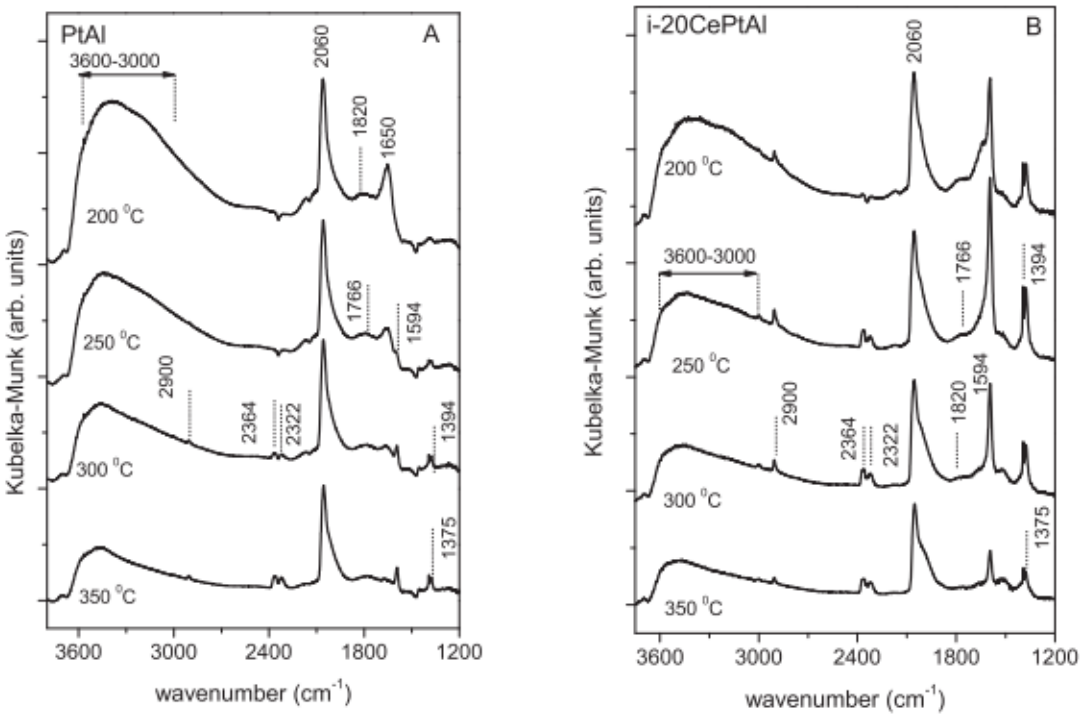

Figure 17: DRIFT spectra of PtAl (A) and i-20CePtAl (B) catalyst during WGS reaction at different temperatures.

To analyze the stability of species on the surface, the feeding was interrupted and the spectra recorded at 350 °C after 10 and 15 min. Complete CO_2 desorption is observed after 10 min for PtAl and after 15 min for i-20CePtAl, while the formate band at 1564 cm^{-1} decreases but it is still present.

To get further insights about the interaction of CO in the absence and presence of water, the samples was subsequently analyzed by closing and opening the water inlet at 350 ^{0}C, after being submitted to WGS conditions. Figure 18 shows the results for the i-20CePtAl sample. The absence of water led to a decrease of CO_2 bands with the time, as shown in the Figure 18 (a), (b) and (c). On the other hand, both formate and Pt-CO bands remained almost intact. Thus, these species are stable and are probably spectators in the reaction. If the formates were intermediates, the bands would be totally converted to products. The formate decomposition is related to the reaction rate [13]. For catalysts like MgO and Rh/CeO_2 that do not present a high activity the formate decomposition is comparable to the reaction rate and has been proposed that 10-15% of the products come from the formates observed by IR spectroscopy [13]. However, Xu et al [151] found that formates are spectators for Pt-Ru/CeO_2 catalysts that are more active. Further theoretical calculations [152][153] showed that large activation barriers exists to decompose the formates making this reaction pathway more difficult. The water was turned on again and the CO_2 band reappeared at the surface (Figure 18d).

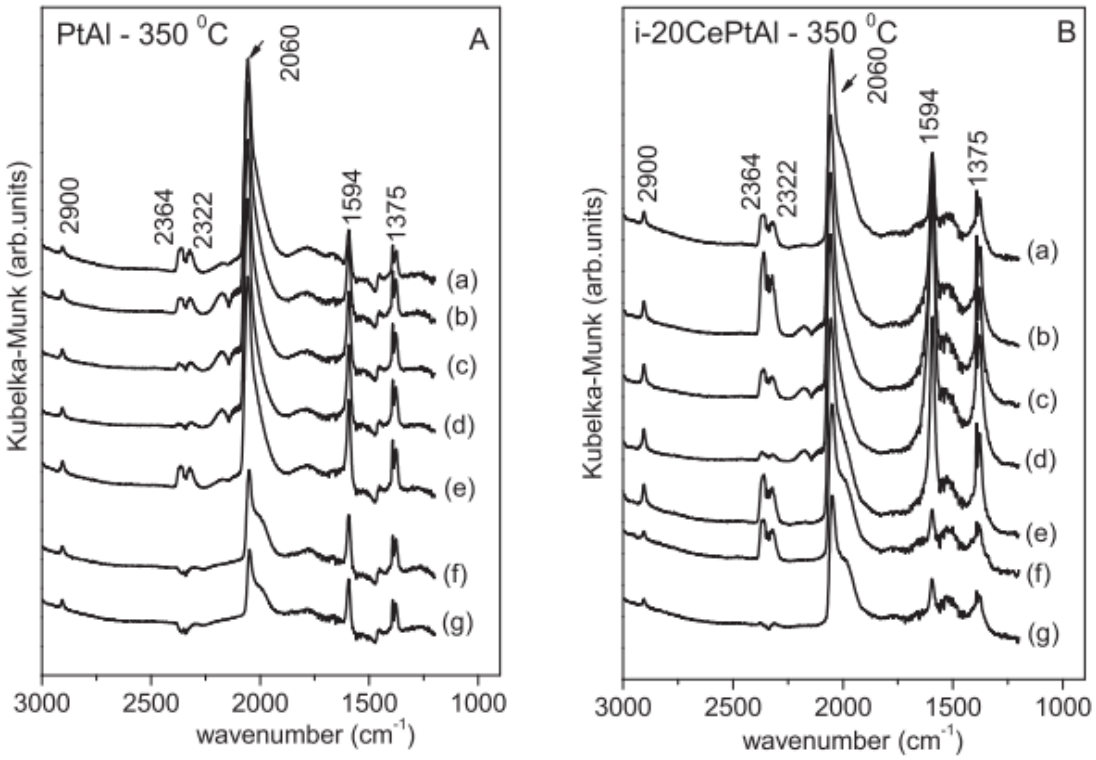

Figure 18: DRIFT spectra for PtAl (A) and i-20CePtAl (B) catalysts at 350 °C under (a) WGS ($CO + H_2O + He$), under $CO + He$ for (b) 1 min, (c) 5 min, (d) 10 min; under WGS again after (e) 1 min and output and feeding closed for (f) 10 min and (g) 15 min

I.7. Discussion

The importance of the metallic phase and the support on the catalytic activity for WGS reaction has been discussed but the role of each catalyst component is still not clear. By preparing the catalysts from the same batch of colloidal nanoparticles it was possible to obtain Pt-Al_2O_3 and Pt-CeO_2-Al_2O_3 catalysts with similar platinum dispersion as previously described [112] [5]. This strategy of synthesis allowed evaluating independently and in an uncorrelated manner the impact of the structural and redox properties of the CeO_x on the alumina support in the WGS reaction. By changing the method used to produce the ceria-alumina support it was possible to raise interesting questions about the impact of support properties and its interaction with the metal particles.

Since the catalysts were prepared from the same batch of colloidal nanoparticles the platinum structure, confirmed by EXAFS results, was similar for all the samples. However, they showed different redox properties comparing the samples with and without Ce and the preparation method.

XANES and XPS results show that the supported Pt-NPs oxidize during catalyst sol-gel preparation and calcination, which can be reversed by reduction. After reduction, the Pt-NPs in all catalysts show similar structural parameters, confirmed by EXAFS. Since the Pt-NPs are similar in all samples, a similar standard free energy and equilibrium constant for the Pt + O ↔ PtO reaction could be expected. Nevertheless, clear differences among the catalysts were found. Before reduction, the Pt-NPs are more oxidized on samples containing ceria; among the ceria containing samples, the GEL samples lead to higher Pt-NPs oxidation. Theoretical calculations [113] show a charge transfer when Pt is on top of CeO_2 (111) surface with spontaneous reduction of the substrate and formation of vacancies, changing the cerium oxidation state in the vicinity of Pt from Ce^{4+} to Ce^{3+}. The more severe oxidation observed for GEL samples suggests that the Pt-O-Ce interaction is more extensive when Ce is added to gel. Additionally, for the GEL samples higher temperatures are necessary to reach the same amount of Pt° and PtO_2 (Figure 10b) reinforcing the difficulty in reducing Pt in the presence of Ce. Higher reduction temperature was also observed by González et al. [71] comparing Pt/CeO_2 with Pt/TiO_2 or Pt/CeO_2-TiO_2, which was assigned to differences in the metal-support interaction.

The higher temperature found for Pt on CeO_2 was attributed to the reduction of PtO_x species while the lower temperatures on TiO_2 and CeO_2-TiO_2 would be due to the reduction of PtO_x with lower stoichiometry (PtO).

After reduction, Pt-NPs show similar structural parameters (Table 4) and it is not possible to see differences in the average oxidation state of the Pt-NPs by in situ XAFS (Figure 10b); however, XPS results suggest partial Pt surface oxidation and/or charge transfer to the support. Interestingly, FTIR-CO spectra were sensitive to the presence of Ce through the relative intensity and symmetry of the bands. Additionally, bands in the low wavenumber region of the IR spectra (Figure 12a) are strongly suppressed in Ce-promoted catalysts; these results indicate that ceria may change the local Pt electron density or block part of the Pt sites [118] [120] [121]. Bruix et al. [36] observed a strong metal support interaction especially for small Pt particles and suggested that this interaction determines the reaction pathway, having mainly an influence in the water dissociation.

Many factors influence the support and metal-support interaction. In our case, considering the similarity among the samples concerning the Pt-NPs, the support characteristics and its interface with Pt should mainly determine the catalyst properties. Different Ce species could be expected based on the preparation methods and conditions: i) crystalline CeO_2 and non-stoichiometric phases; ii) few nm-sized CeO_2 crystallites and/or a highly dispersed CeO_x phase that could not be detected by XRD; and iii) Ce-O-Al local surface sites. The results show that the GEL preparation method and smaller loading favor the formation of a more dispersed phase. In fact, only for the i-20CePtAl the XRD pattern of nanocrystalline CeO_2 domains can be clearly recognized. This reflected on cerium oxidation state, and in this aspect, this sample is differentiated, showing smaller % of Ce^{3+} (surface and bulk) that is not significantly affected by reduction at 500 °C.

Looking in more detail at the local structure of the ceria phase, the Ce K-edge EXAFS analysis reveal some interesting features. It confirms that the IMP samples have a more ordered structure than the GEL samples. In particular, the i-12CePtAl sample shows a Ce-Ce contribution with average distance similar to the CeO_2 phase; this contribution is not presented in the g-Pt12CeAl. Different from the bulk CeO_2, however, two Ce-O distances are found for both samples, one shorter (~2.23–2.28 Å) and another longer (~2.43–2.47 Å) than the CeO_2 fluorite phase (2.34

Å). Similar Ce-O distances were previously reported in the literature: the shorter one was found in 4-fold Ce^{3+}sites in (111) CeO_2 (short distance) [154] and the long one in surface sites of nanometric $Ce_{21}O_{41}$ [154], in Ce_2O_3 [ICSD Coll.Code: 96202], and in $CeAlO_3$ [ICSD Coll.Code: 150277]. Interesting, after reduction a Ce-Al contribution is detected, independently of the preparation method. The Ce-Al distance is similar to the one found in $CeAlO_3$. It is important to remark, however, that is unlike that the crystalline $CeAlO_3$ would be formed at the low temperatures used in this work (maximum of 500 °C) [129]. In fact, both EXAFS and XRD data show that the formation of $CeAlO_3$ crystalline phase is ruled out. The results also show that Ce_2O_3 crystalline phase is not formed under reduction. In these two phases, the Ce-Ce distance would be longer (4.08 Å) and shorter (3.27 Å), respectively. Therefore, although we detect small crystallites of CeO_2 in the IMP catalysts, it is likely that in all samples a large fraction of a well dispersed CeO_x phase is formed and that the reduction enhances the interaction with the alumina support.

Ceria structure is intrinsically related to the amount of Ce^{3+} and vacancies formation. Vacancies formation is easier in small CeO_2 particles than on CeO_2 surfaces and it is further facilitated by the presence of Pt [41] [134] [53] [51] [52]. Migani et al. [51] demonstrated that the energy separation between the valence and the conduction band for ceria nanoparticles is lower compared to the (111) surface, promoting vacancy formation. The addition of metallic Pt- NPs favors the formation of Ce^{3+} ions by electron transfer from the metal cluster. Thus, the vacancy formation also depends on the contact between the removed O and Pt [53]. Rodriguez et al.[86] observed a significant increase of Ce^{3+} under WGS for catalysts with small clusters of Pt and Ce_2O_3 nanoparticles rather than what was observed for Pt supported on bulk CeO_2 where the ceria reduction was less than 0.5%. Concerning ceria crystallographic orientation, earlier studies proposed a high OSC for the (100) surface when compared to (110) or (111) since the energy required to form an oxygen vacancy is smaller [54] [55]. Further experimental observations and DFT analysis stated that oxygen vacancies tend to group together in clusters [56]. Thus, it is possible to observe that ceria vacancy formation and as a consequence the OSC depends on its interaction with alumina, its particle size, its surface structure and its proximity to a metallic nanoparticle and as a consequence, should be deeply affected by the catalyst preparation method. In our case, the OSC results are an average contribution of

several species and the weight of each one varies among the samples. The similar OSC values found for samples with the same ceria content, despite the larger average CeO_2 crystalline domain in the IMP samples suggest that small CeO_2 particles distribution tail and highly dispersed CeO_x species dominates.

Different reaction mechanisms can occur depending on the support and atmosphere conditions. The most important are: i) monofunctional redox mechanism on the metal: for this mechanism, only the metallic site participates on the reaction. It involves H_2O reduction forming H_2 and Pt oxidation. Afterwards, Pt reduces regenerating the active site and CO oxidizes to CO_2. ii) bifunctional metal-support redox mechanism: for this mechanism, CO adsorbs on Pt and H_2O adsorbs on the support. The H_2O oxidizes the support (S-O) forming H_2 and the S-O reacts with the CO forming CO_2. iii) bifunctional metal-support redox mechanism involving OH-support sites: for this mechanism, CO adsorbs on Pt and H_2O decomposes adsorbing on the support as S-OH and S-H. Then, S-OH decomposes into S-H and S-O. Both S-H reacts forming H_2 and the S-O oxidizes CO forming CO_2. iv) formate associate mechanism: this mechanism involves a hydroxylated support and the adsorption of molecular H_2O on the support. Firstly CO adsorbs on Pt and rearranges forming a formate with the S-OH, recovering the metallic site. H_2O adsorbs molecularly on the support reacting with the formate yielding CO_2 and H_2, recovering the hydroxylated support surface. v) formate associative mechanism on CeO_2: does not involve the metal just the support where is found hydroxyls that interacts with CO forming formates that will interact with water adsorbed molecularly, also on the support surface, forming CO_2 and H_2 [142].

Considering the WGS activity, regardless the debate about the dominant mechanism (redox, associative or associative with redox regeneration) and the most likely intermediates (formate, carbon- ate, carboxylate), it is a consensus that ceria and its interface with Pt play an important role in water activation and the intermediates that are formed [155] [32] [156]. Lykhach et al. [155] found that the interaction of water with CeO_{2-x} does not cause any detectable change at Ce oxidation state for well-ordered CeO_2 (111) model catalysts. On the other hand, reduction of CeO_x on Pt (111) forming hydroxyl groups due to the presence of water have been reported [157]. Matolín et al. [158] suggested that the ceria reduction when water desorbs, for CeO_2(111)/Cu(111) model catalysts, is due to an increase of the Ce 4f level occupancy. While CO is only activated on the metal, water can be activated on Pt, on the support or on the metal-

support interface [32] [36] [159] [160] [161]. The participation of formates as intermediates has been intensely discussed in the literature, and one of the reasons is the difficulty in associate the FTIR date with kinetics data in different temperatures and compositions [162] [163]. A critical analysis of contribution of formate mechanism was presented by Burch et al. [13], concluding that formates account for just a small percentage of the total WGS reaction. Jacobs et al. [150], on the other hand, raised several arguments in favor of the intermediate role played by the formates, in particular at low temperature WGS conditions, since assistance of water is critical to formates decomposition under reaction. A recent work using concentration-modulation spectroscopy in DRIFTS mode under WGS reaction at low temperature 250 °C showed that the absorption bands from carbonate (1500–1400 cm^{-1}) and bidentate formate (1550, 1370 cm^{-1}) groups vanish in the phase-resolved spectra, indicating that they are spectator species [148]. On the other hand, the monodentate formate and carboxylate species are found to be intermediates, in agreement with carboxyl mechanism activated at the metal-oxide interface. Concerning the role of carbonates, evidences of their high stability on Pt/CeO_2 at 300 °C was obtained using transient isotopic experiments, where is excluded the exchanges of carbonyl in $^{12}CO_3^{2-}$ with ^{13}CO in gas phase [164]. The participation of labile oxygen of the ceria support in the WGS reaction supporting the redox mechanism was demonstrated using ceria as source of ^{18}O and monitoring the evolution of $C^{16}O_2$, $C^{16}O^{18}O_2$ and $C^{18}O_2$ with time on stream. The dependence of the activity with ceria structural properties and nanosize effects were not addressed in this work.

It is clear that the samples studied in this work have significant differences related to the balance of the different CeO_x species and its initial interaction with the Pt-NPs. Surprisingly, the results do not pointed out a direct correlation with the performance in WGS. Panagiotopoulou and Kondarides [165] found that for Pt/CeO_2 catalysts, with CeO_2 particles in the size range of 10–21 nm and surface areas of 25–57 m^2/g, the catalytic activity did not depend on the structural and morphological characteristics of CeO_2. However, recent theoretical studies by Vayssilov et al. [41] found that the oxygen transfer from ceria to Pt (reverse oxygen spillover) is strongly dependent on the ceria structure at nanoscale and its contact with Pt and can help to explain the enhanced performance of $Pt\text{-}CeO_2$ catalysts. Therefore, it could be expected that the smaller crystalline domains and the clear different characteristics

among our samples should affect the activity, in agreement with the work by Bunluesin et al. [45]. In addition, the existence of a reactive zone around the Pt-NPs in WGS reaction, in the order of 1–2 nm for ceria-based supports has been discussed in several works [166] [167] [168] [169] [170] [29] [164] [159] [150], and is dependent, for example, on the presence of dopants, such as Ti^{4+}, La^{3+} and Zr^{4+} [169] [164]. The diffusion of the intermediates species in this reaction zone is a key aspect that affects the reaction rate. It could be expected that ceria nanosize effects have a significant impact. Several works have pointed out a dependence of the WGS activity on Pt particle size (or Pt loading) and support [166] [164] [36] [86]. In our case, the Pt-NPs size are similar among the samples, but the ceria phase was different. In fact, the electron density changes on Pt surface through the position of adsorbed CO band or contraction of Pt-Pt distance bond could not be clearly observed in different catalysts. Thus, it could be reasonable to suggest in a first approximation a similar catalytic property for Pt sites in PtAl and PtCeAl. It has been presented in the literature [164] that turnover frequencies in Pt/CeO_2 catalysts do not strongly depend on the Pt size, for particles in the ~1–8 nm range. On the other hand, it has been proposed that the interfacial Pt-O-Ce sites are the most reactive [164] [36] [171] [172].

It is interesting to mention that several works also point out that the strong metal support interaction, especially found in small Pt particles in contact with ceria, is determinant to the reaction path- way, mainly influencing water activation and dissociation [32] [36]. The Pt-O-Ce interaction, as demonstrated from theoretical studies [36], significantly enhances the ability of the admetal to adsorb water and dissociate the O−H bonds. It also affects the stability and decomposition of intermediates [32] [150]. Aranifard et al. [32] demonstrated from first principle that the Pt-O-Ce interface sites are 2–3 orders of magnitude more active than Pt(111) and the associative carboxyl pathway with redox regeneration could be the preferential pathway to the overall rate. Our experimental data showed that for Ce-containing catalysts the WGS specific reaction rates increase less than one order of magnitude compared to the PtAl unpromoted catalyst, lower than expected based on the theoretical studies (about 2 orders of magnitude taking in account the way Pt atoms are considered, surface or perimeter) [32]. On the other hand, theoretical calculations showed a decrease in the density of Pt 5d states near the Fermi level for the $Pt/CeO_2(111)$ system compared to bulk Pt [173] [174], in agreement with our XPS data.

Thus, a smaller heat of adsorption of CO bonded on Pt atoms is expected at the Pt-O-Ce interface, increasing the reactivity of the CO interface relative to the unpromoted catalyst. Compared to the PtAl, the changes of electron density of Pt near the Pt-O-Ce interface and the presence of Pt-O-Ce could increase the reactivity of CO and enable a new pathway for WGS, respectively. Considering that, (i) at high WGS temperature a small fraction of the Pt surface is covered by CO, (ii) not all adsorbed CO are part of the active pool [164], (iii) formates and carbonates are stable species; (iv) not all Pt sites make interface with ceria; and (v) different ceria species exist in our samples; the main dependence of the activity with the two ceria loading for the two preparation methods, and not with the average ceria structural properties, suggests that the creation of the interfacial sites seems to be the limiting factor in these samples. Therefore, increasing the cerium loading is likely to increase the amount of most active sites at interface of Pt interacting with ceria.

I.8. Conclusion – Part I

Catalysts are very complex and dynamic systems since their behavior depends on the structural and electronic properties of different species and on the temperature and atmosphere they are submitted to. In this work we show that the presence of Ce in PtAl catalysts increases the WGS specific reaction rates up to seven times in the WGS reaction. Several parameters impact the activity and the use of pre-formed Pt-NPs was the strategy adopted to prepare model systems focusing on the support and interface effects. It was possible to highlight differences and similarities among the samples concerning several parameters related to the cerium oxide phase, such as ceria crystalline domain size and local environment, the initial contact between the metal and the oxide, the ceria oxidation state among others. However, a clear identification of a possible main ceria parameter governing the reaction turned out to be challenging and a direct correlation between the properties that were observed by both ex situ and in situ experiments and the catalyst activity could not be clearly made. The main parameter affecting activity seems to be ceria loading; however, the increase in specific reaction rate values due to the presence of ceria was significantly smaller than predicted by theory considering a Pt-O-Ce interface [32]. Thus, similar to the use of pre-formed platinum nanoparticles, it could be worth to explore well-defined oxide

particles to clearly evaluate aspects such as dependence of the crystalline size, exposed facets and oxidation state under reaction conditions.

The importance of *in situ* characterization was once more highlighted since different properties were observed depending on the atmosphere and temperature. These results suggest that the odds to create the true active sites might be the limiting factor in these samples and that they are related to the contact to highly dispersed CeO_x species. Nevertheless, how different species of ceria, such as highly dispersed CeOx species in contact with alumina and few nm-sized crystallites of ceria operate in water activation and intermediates formation has still to be deeper understood.

Part II

II.9. Materials and Methods

II.9.1. Catalysts preparation – Conventional impregnation method

Alumina support, prepared as described elsewhere [94], was impregnated with H_2PtCl_6 to produce two sets of catalysts: 0.3 and 1% Pt w/w. The impregnated supports were calcined in air at 500 ^{0}C for 4h and referred as 03PtAl and 1PtAl, respectively. Part of each sample was further impregnated with cerium nitrate (6 and 12% w/w CeO_2) and calcined again. These catalysts will be referred as 12Ce03PtAl, 6Ce1PtAl and 12Ce1PtAl, respectively.

II.9.2. Characterization

The characterizations that were performed were XRD, SBET and Vp, FTIR with CO adsorption and OSC. The conditions were described before in Part I. The catalytic tests were performed using the H_2O/CO ratio 3:1, like in Part I, however using 100 mg of catalyst. Different *in situ* characterizations were done and will be described below.

II.9.2.1. X-ray absorption measurements

XANES and EXAFS at Pt L_3-edge (11564 eV) were measured at BM23 beamline at ESRF in fluorescence mode. The beamline and the experimental setup used were the same described before. Some spectra were also recorded at Pt L_2-edge (13273 eV).

For all samples, the *in situ* experiments follow the procedure represented Figure 19(A). Two EXAFS spectra at Pt L_3-edge were recorded before reduction, at room temperature (energy range: 11200-12200 eV, kmax = 13Å^{-1}). The sample was reduced *in situ* (5%H_2/He, 5 ^{0}C.min^{-1}, up to 500 ^{0}C) and kept at this temperature for 90 min while XANES spectra were recorded in the energy range 11500 to 11620 eV. Each spectrum took about 13 min. After reduction, the sample was cooled down under H_2, and EXAFS was measured (same energy range used before) at room temperature. Then, the temperature was increased to 250 ^{0}C and three EXAFS spectra were measured. After, the H_2/He flow was changed to WGS conditions, using CO:H_2O molar ratio equal to 1:3, 150 ml/min of CO (5%CO/He) and 50 ml/min of He passing through a saturator with water at 70 ^{0}C to carry 22.5 mL/min of water. Three EXAFS spectra

were recorded taking one hour each. After this, the atmosphere was changed for H_2/He again (100 ml/min) and the temperature increased to 500 ^{0}C (5 ^{0}C.min^{-1}). When the temperature reached 500 ^{0}C it was decreased again to 250 ^{0}C where three EXAFS spectra were measured. In all the steps, after the EXAFS measurement, a XANES at Pt L_2 edge was measured (energy range: 13150 to 13450 eV). The same experiment was repeated for a reaction temperature of 350 ^{0}C. The two sequences (250 and 350 ^{0}C), that took more than 24h each, were done for all the samples.

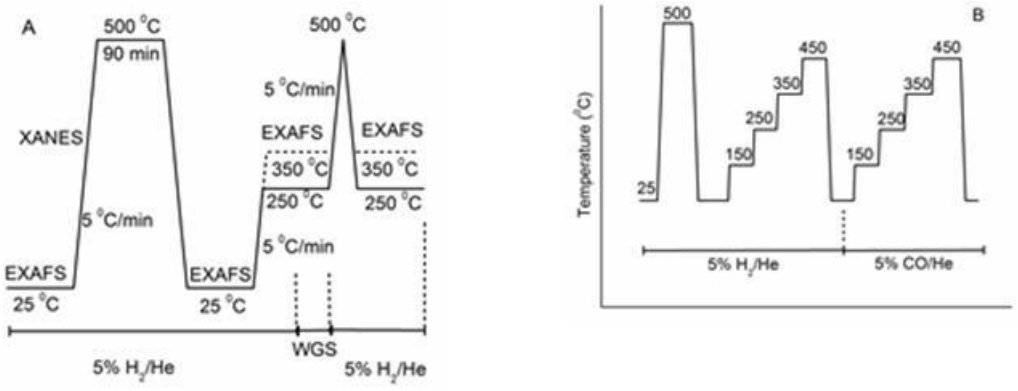

Figure 19. Experiment scheme. (A) under hydrogen and WGS reaction (B) under hydrogen and CO.

Another set of experiments was done for some samples according Figure 19(B). XANES measurements, using the same conditions described above, were performed continuously. After reduction, under hydrogen, the temperature was increased from 25 ^{0}C up to 150 ^{0}C and then up to 450 ^{0}C, using 100 ^{0}C steps. Thereafter, the sample was cooled down and at room temperature the atmosphere was changed to CO (5%CO/He, 100 mL/min) and the temperature sequence was repeated.

II.9.2.1.1. Pt XANES data analysis

It was not possible to measure a reference simultaneously with the sample due to the setup used for the fluorescence measurements. Thus, to perform the sample alignment glitches at I_0 were used as an internal reference.

II.9.2.1.1.1. Linear combination analysis (LCA)

After spectra normalization, LCA [175] was done for each spectrum using Pt and PtO_2 as references as described before.

II.9.2.1.1.2. Delta XANES analysis (ΔXANES)

Another analysis was performed for these samples, called Delta XANES (ΔXANES). This analysis aim to identify small electronic/structural modifications due to specific perturbations like: pH, presence of an adsorbate, magnetic field etc. The sample spectrum is subtracted from a reference spectrum obtaining a differential spectrum. Thus, it is assumed that the two XANES spectra are different just by the external perturbations.

In our case, we are interested in differences caused in the metal by gases adsorption. The gas adsorption occurs due to the overlap of atomic orbitals, from the adsorbate, with the bands of the metal, forming bonding and antibonding molecular orbitals. For transitions metals, electrons with “d” character are involved and can be detected in L_3 edge XANES due to the appearance of special features in the spectra.

Theoretical calculations reproduced special features for gases adsorbed on specific sites of platinum, Figure 20. A positive contribution is observed for atop sites and there was no shift for the absorption edge. However, for bridge or nfold (also called three fold) sites a negative contribution appears followed by a positive contribution due to a charge transfer. Thus, comparing experimental and theoretical results it is possible to identify the type of sites on which the gases are adsorbing. Furthermore, it is possible to identify differences between different gases adsorption or differences caused by the contact between the metal and the support.

Initially, the calculations were done for hydrogen but nowadays studies involving CO, O_2, ethylene, water and hydroxides can be found in the literature. Additionally, studies involving metals like Rh and Ru were also performed [87,176,177].

In addition, to perform this kind of study, it is necessary a careful energy calibration and data normalization since it can create artifacts making difficult the interpretation.

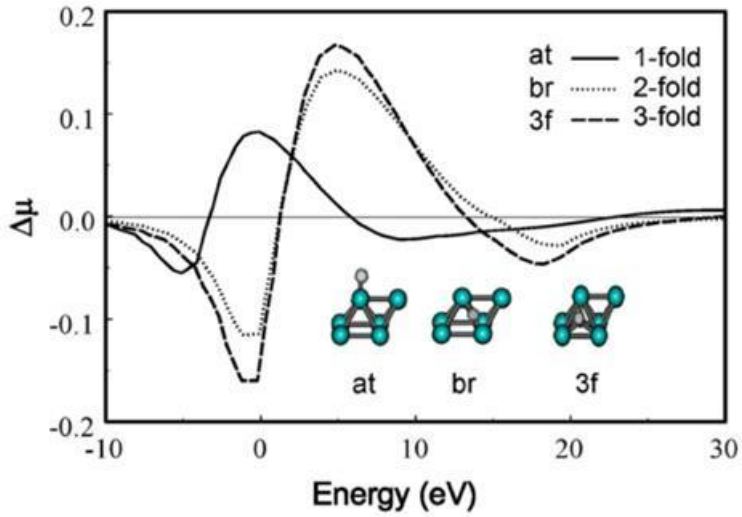

Figure 20. Delta XANES technique features for hydrogen adsorbed on atop, bridge and threefold (nfold) sites for Pt L_3 edge [178].

The spectra at 500 ^{0}C collected under H_2 was very similar for all the samples. Thus, we assumed that in principle no gases are adsorbed, at this temperature, on the sample. This was the maximum temperature that the measurements were performed since at this temperature the samples were completely reduced. Further, avoiding higher temperatures particle agglomeration is avoided. Thus, the XANES collected under each atmosphere was subtracted from the XANES collected under H_2 at 500 ^{0}C. The result from this subtraction leads to an evaluation of the effects due to the gas adsorption and active sites formed on the particles. This procedure was done for both edges and the results correspond to $\Delta\mu L_2$ and $\Delta\mu L_3$ to L_2 and L_3 edges, respectively.

II.9.2.1.2. Pt EXAFS data analysis

The EXAFS signal was extracted and the oscillations were Fourier-transformed in the same way described before (k range = 3-10 Å^{-1}).

Apart from Pt-Pt contribution, calculated for metallic Pt, to obtain a good fit it was necessary to include a Pt-O contribution, calculated for PtO_2. Three contributions were determined by fitting in R-space (1.4-3.2 Å). One corresponding to the Pt-Pt interaction and the other two corresponding to interactions between Pt and O with two different inter-atomic distances (Pt-O_S and Pt-O_L, $_S$=short, $_L$= long) that will be discussed later. For each contribution, three parameters were adjusted: N_i, R_i and σ_i^2. To decrease the correlation between the parameters, that is very strong, all

samples, at same temperature and atmosphere were fitted together. The same distance (R_i) was applied for all samples to the same contribution and just one σ_i^2 was used for all the contributions. The correlation between the parameters is presented at Table 11. The S_0^2 and ΔE_0 were fixed and equal to the values found for the reference compounds.

After finding the best fit in each case, to evaluate the errors bars we fitted just one parameter each time keeping the values for the other parameters constant.

Table 11: Correlation between the EXAFS parameters for the impregnated samples.

	Sample 1	**Sample 2**	**Sample n**
N_{Pt-Pt}	N_1	N_2	N_n
R_{Pt-Pt} (Å)	R_{Pt}		
N_{Pt-OS}	N_{1OS}	N_{2OS}	N_{nOs}
R_{Pt-OS} (Å)	R_{OS}		
N_{Pt-OL}	N_{1OL}	N_{2OL}	N_{nOL}
R_{Pt-OL} (Å)	R_{OL}		
σ_i^2 (Å^2)$_{Pt/Pt-O}$	σ_i^2		

II.10. Results

Diffraction patterns before and after the calcination (not shown) presented a boehmite and γ-alumina structure, respectively. No peaks corresponding to Pt^0 or CeO_2 were observed confirming that the samples are well dispersed.

The surface area results are presented in Table 12. About 200 $m^2\ g^{-1}$, with small variations depending on the cerium and platinum loading. Thus, the impregnation did not affect the textural properties of the support.

Table 12: Surface area and oxygen storage capacity.

Sample	Surface area ($m^2.g^{-1}$)	OSC (µmol $O_2\ g^{-1}$)	
		250 ^{0}C	350 ^{0}C
03PtAl	192	--	--
12Ce03PtAl	202	0.35 (± 0.04)	0.47 (± 0.08)
1PtAl	227	--	--
6Ce1PtAl	210	0.48 (± 0.07)	0.68 (± 0.1)
12Ce1PtAl	197	0.39 (± 0.05)	0.72 (± 0.1)

The OSC results are also presented in Table 12. At 250 ^{0}C the OSC were about 0.4 µmol $O_2\ g^{-1}$ and increased to 0.5 µmol $O_2\ g^{-1}$ to 12Ce03PtAl and 0.7 µmol $O_2\ g^{-1}$ to 6Ce1PtAl and 12Ce1PtAl at 350 ^{0}C. It is known that the Pt^0 advances the Ce

reduction. At 250 ^{0}C, according to the XANES data (Figure 24) Pt is in the oxide state. Thus, below 250 ^{0}C probably Pt is not helping the Ce reduction and the samples presented lower OSC. On the other hand, increasing the temperature, Pt became more reduced, especially for the samples with higher amount of Pt, and the OSC increased, showing the importance of this interface between Ce and Pt for this redox process.

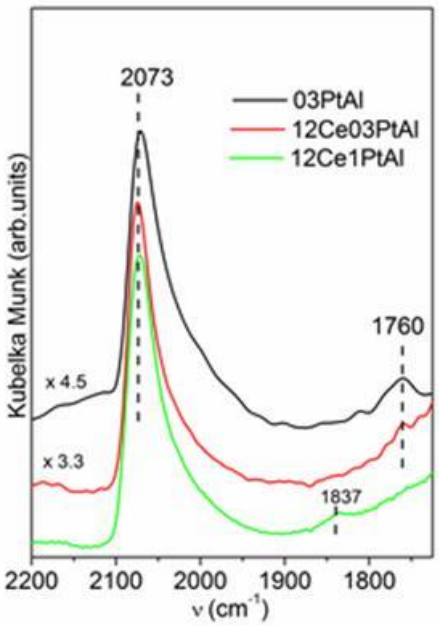

Figure 21. DRIFT spectra of adsorbed CO.

FTIR experiments, with CO adsorption, were performed in the region 2200 to 1700 cm^{-1} for the samples 03PtAl, 12Ce03PtAl and 12Ce1PtAl to evaluate the Pt sites available at the surface (Figure 21). A band with a high wave number at 2073 cm^{-1} corresponds to CO linearly adsorbed on Pt atoms in arrays [118] [179]. The FWHM, that is sensitive to the particle size, is bigger for the sample 03PtAl than for 12Ce03PtAl, showing that the samples with Ce are better dispersed. 03PtAl also presents a band at low wave number (1760 cm^{-1}) related with CO adsorption at high coordinated sites [118] [179]. The sample 12Ce03PtAl also presents this band but it is very small. A different band at 1837 cm^{-1} is observed for the sample 12Ce1PtAl related with CO adsorption at bridge sites [118] [179]. Thus, already from the CO adsorption results it is possible to notice that there is a variation on the sites that are formed for each sample depending on the Ce and Pt loading.

Figure 22 presents the EXAFS oscillation in k-space and the magnitude of the Fourier transform (R-space) with the best fit for 03PtAl before the reduction. The results for the other samples (12Ce03PtAl, 1PtAl, 6Ce1PtAl and 12Ce1PtAl) are

presented in Figure 1 in Annex C. The fit results are presented in Table 13. The first coordination shell corresponds to a single Pt-O contribution, showing that the Pt is completely oxidized after calcination. No residual chlorine was detected (no Pt-Cl contribution was observed). The coordination numbers for the samples with 0.3% of Pt are N_{Pt-O} = 4.5 and 6.0 for 03PtAl and 12Ce03PtAl, respectively. For the samples with 1% they are N_{Pt-O} = 5.0, 6.0 and 5.5 for 1PtAl, 6Ce1PtAl and 12Ce1PtAl, respectively. The coordination numbers are very similar for all samples apart from the different amount of Pt. A small contraction (ΔR = 0.08 Å) of the bond distance is observed, compared to the PtO_2 reference 2.07 Å, what is expected since it is a nanoparticle.

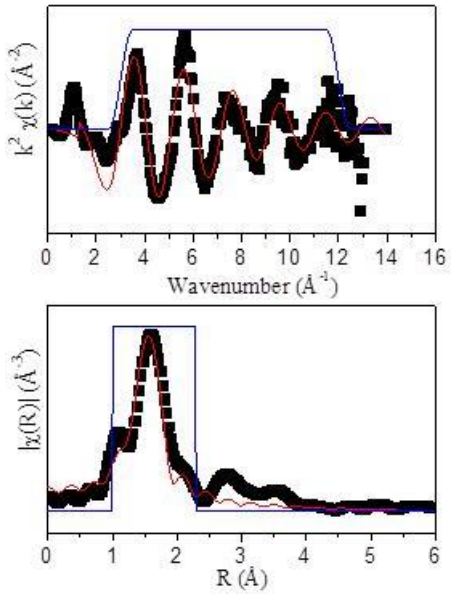

Figure 22. EXAFS data and fit at k space and Magnitude of the Fourier transforms for 03PtAl before the reduction.

Table 13: Structural parameters obtained from EXAFS analysis of the first coordination shell before the reduction.

	03PtAl	12Ce03PtAl	1PtAl	6Ce1PtAl	12Ce1PtAl
N_{Pt-O}[a]	4.5	6.0	5.0	6.0	5.5
R_{Pt-O} (Å)[b]	1.994				
σ^2_{Pt-O} (Å²)[a]	0.005				

E_0 = 8; S_0^2 = 0.9; a = error about 10%; b = error about 1%

Figure 23 presents the XANES spectra for the sample 03PtAl during the reduction. The white line intensity, for platinum, is related with the 5d orbitals occupancy. Before the reduction, the sample does not match with the spectra of PtO_2 reference due to the sample small particle size. Then, increasing the temperature, under hydrogen, there is a decrease in the white line intensity. This decrease indicates

the sample reduction since it corresponds to the increase of the 5d level occupancy. The sample is completely reduced at 500 ^{0}C comparing to the Pt^0 standard as shown in the quantification. At the end of the reduction the spectrum does not corresponds exactly to the standard spectrum of Pt^0, again due to the particle size effects. For the other samples the spectra are very similar and not shown.

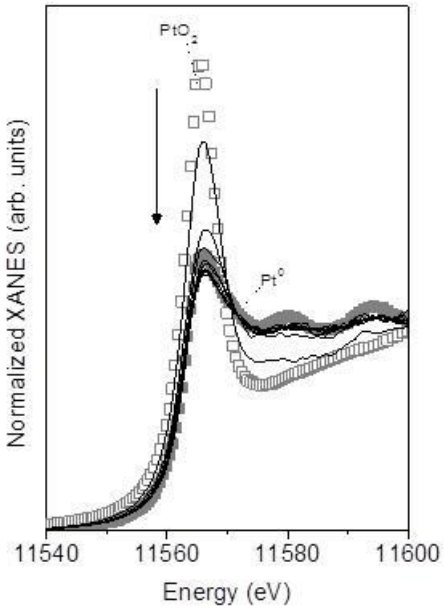

Figure 23. XANES spectra for 03PtAl during the reduction.

Figure 24 shows the percentage of Pt^0 and PtO_2 during the reduction for all samples describing the evolution of these species with temperature. The results were obtained by linear combination analysis for each spectrum using Pt^0 and PtO_2 standards. Pt^0:PtO_2 ratio of 1 is reached at: 30, 240, 262, 298 and 314 ^{0}C for 03PtAl, 12Ce03PtAl, 6Ce1PtAl, 12Ce1PtAl and 1PtAl samples, respectively. Sample 03PtAl is completely reduced at 240 ^{0}C while the others are completely reduced only at 500 ^{0}C.

Probably, the sample 03PtAl is easier to reduce than 1PtAl due to the lower amount of Pt. Concerning the samples with Ce, it is clear that as Pt changes the Ce oxygen storage capacity (as observed above) the Ce also changes the Pt redox properties. Interestingly opposite effects are observed depending on the ratio between Pt and Ce loading. Comparing the sample 12Ce03PtAl and 03PtAl it is possible to observe that the Ce addition slowed down the Pt reduction (it was necessary a higher temperature to reach the same amount of Pt and PtO_2). However for the samples containing 1% of Pt the temperature necessary to reach Pt^0 equal to PtO_2 is inversely proportional to the Ce loading (1PtAl > 6Ce1PtAl > 12CePtAl) and thus the Ce is

improving the Pt reduction. Probably this is due to the Pt particle size and contact area with Ce.

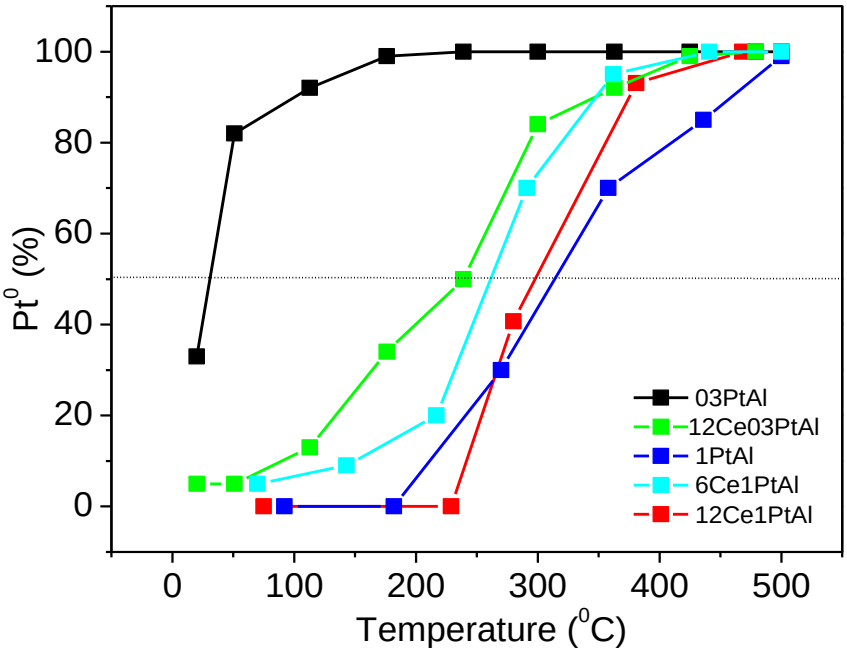

Figure 24. Quantification of platinum species during the reduction.

Figure 25 presents the EXAFS oscillation in k-space and the magnitude of the Fourier transform (R-space) with the best fit for 03PtAl sample after the reduction. The results for the other samples are presented in Figure 2 in Annex C.

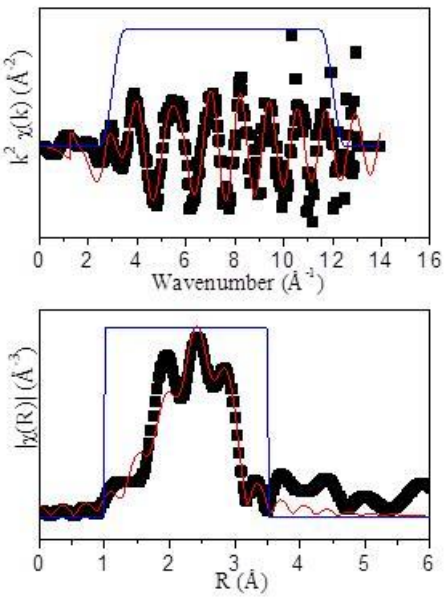

Figure 25. EXAFS data and fit at k space and Magnitude of the Fourier transforms for 03PtAl after the reduction.

Table 14 shows the fits results for the EXAFS data after the reduction for all the samples. The catalysts 03PtAl and 12Ce03PtAl were prepared from the same starting material thus at the beginning they presented the same dispersion. However, after the reduction the samples presented differences. The coordination number is smaller for the sample 12Ce03PtAl than for 03PtAl, showing that the Ce presence increases the stability against agglomeration. This higher stability can also be seen for the samples with a higher amount of Pt where we have the coordination number for Pt-Pt contribution inversely proportional to Ce loading: 9.0 to PtAl > 6.0 to 6Ce1PtAl > 3.3 to 12Ce1PtAl. Moreover 12Ce1PtAl despite presenting a higher amount of Pt presented similar particle size to the sample 12Ce03PtAl confirming the role of cerium in platinum stability.

Table 14: Structural parameters obtained from EXAFS analysis of catalysts after the reduction.

	03PtAl	**12Ce03PtAl**	**1PtAl**	**6Ce1PtAl**	**12Ce1PtAl**
N_{Pt-Pt}	8.5[a]	2.0[b]	9.0[a]	6.0[a]	3.3[a]
R_{Pt-Pt} (Å)	2.72[c]				
N_{Pt-OS}	1.1[b]	2.7[a]	--	--	1.0[b]
R_{Pt-OS} (Å)	2.06[c]				
N_{Pt-OL}	1.8[b]	5.5[b]	--	--	4.0[b]
R_{Pt-OL} (Å)	2.52[c]				
σ^2_{Pt-OS} / σ^2_{Pt-OL} (Å²)	0.01[a]				

E_{0Pt-Pt} = 8; E_{0Pt-O} = 6; S_0^2 = 0.9; a = error about 10%; b = error about 20%; c = error about 1%

The Pt-Pt coordination number for the sample 12Ce1PtAl is about 28% (N_{Pt-Pt} = 3.3) of bulk Pt (N_{Pt-Pt}=12), for the sample with 6% of CeO_2 it is about 50% (N_{Pt-Pt} = 6.0) and for the sample 1PtAl (N_{Pt-Pt} = 9.0) it corresponds to 75% of the bulk. These coordination numbers corresponds to a particle with 0.5, 0.8 and 1.6 nm for 12Ce1PtAl, 6Ce1PtAl and PtAl, respectively, considering a spherical model [79]. Due to the small particle size, the Pt particles structure becomes strongly sensitive to the support interaction and atmosphere conditions.

Although the samples looked reduced from the XANES analyses, we note that the EXAFS data could not be reproduced without adding Pt-O contributions. In fact two main Pt-O contributions, corresponding to two different inter-atomic distances were found: the first (Pt-O_S), about 2.1 Å similar to the value of the first PtO_2 shell [180], and for the samples with 12% of CeO_2 a longer one (Pt-O_L) around 2.50Å.

Two proposals are found in the literature to explain this long Pt-O_L distance. The first could be linked to the omission of Pt-Al interactions in the treatment of EXAFS signal [180]. A Pt-Al contribution model was tried and did not reproduce well our data (the fit quality was worse compared to the fit including the oxygen contribution). The second proposal invokes the presence of adsorbed hydrogen species on the surface [79]. This explanation is more realistic in our case since the measurements were done after reduction and under hydrogen atmosphere. On the other hand, this Pt-O interaction could be associated to the Pt anchoring to the support. This hypothesis is corroborated by the fact that smaller N_{Pt-Pt} and larger values of N_{Pt-O} were found for the samples with Ce (and inversely proportional to Ce loading). Thus, a stronger metal-support interaction, probably is taken place in the sample with Ce, through Ce-O_x species.

Figure 26 and 27 presents the EXAFS oscillation in k-space and the magnitude of the Fourier transform (R-space) with the best fit for the sample 03PtAl under different atmospheres at 250 and 350 ^{0}C, respectively. The results for the other samples are presented in Figure 3 and Figure 4 in Annex C. Table 15 and 16 presents the fit results for the EXAFS data for all the samples under different atmospheres at 250 and 350 ^{0}C, respectively. Interestingly, comparing the coordination number (N_{Pt-Pt}) at room temperature after reduction with the coordination number under H_2 at 250 ^{0}C there is a decrease for the Pt-Pt contribution and an increase for Pt-O contribution for all samples except for 1PtAl. This could be related with morphological changes, due to the high temperature, leading to a flat particle. This Pt-O contribution is larger for the samples with Ce and among them bigger for the sample 12Ce03PtAl probably due to the small particle size. It has been reported [180] that the Pt-O shell increase when the interaction between the Pt and the support becomes more uniform and that the particles adapt their morphology according to the support epitaxy. Stakheev et al. [181] observed a higher Pt-O coordination, originated from the interfacial oxygen atoms, that could be only explained by a flat or raft like morphologies (even in presence of hydrogen) caused by the support ionicity. They argue that the Pt-O bonds become stronger to compensate the increase in the surface free energy due to the small particle size. They also observed a short and a long distance for Pt-O contribution. Further, different coordination numbers from room temperature to high temperature leads to an interesting discussion concerning Pt dispersion measurements that are normally done.

Erroneous values of dispersion can be obtained if the temperature measurements are different from the reaction temperatures.

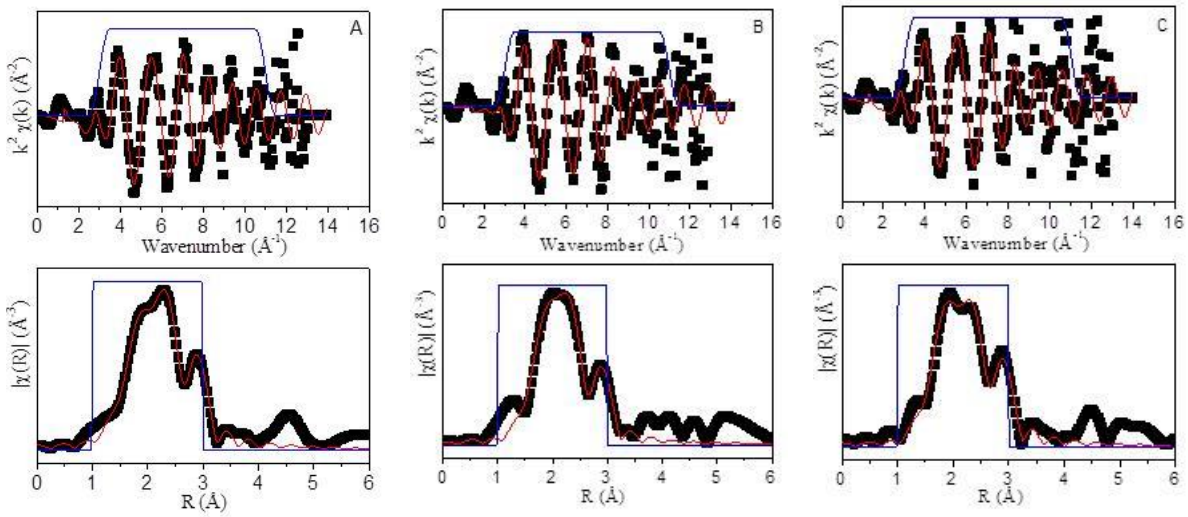

Figure 26. EXAFS data and fit at k space and Magnitude of the Fourier transforms for 03PtAl 250 ^{0}C (A) H_2, (B) WGS, (C) H_2-second time.

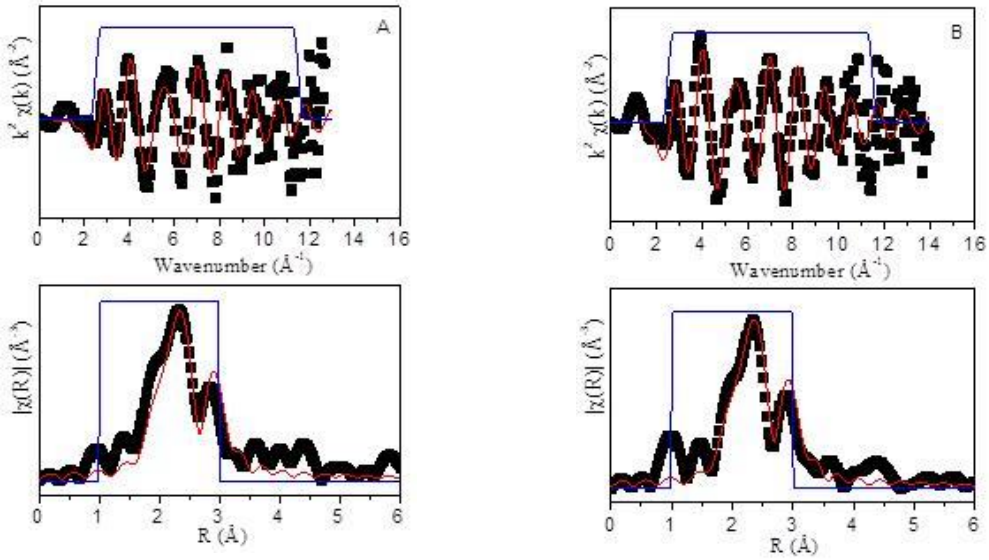

Figure 27. EXAFS data and fit at k space and Magnitude of the Fourier transforms for 03PtAl 350 ^{0}C (A) H_2, (B) WGS.

Small changes were observed for the samples under different atmospheres at 250 ^{0}C (Table 15). However, when the temperature is increased to 350 ^{0}C (Table 16), for the sample 03PtAl there is a significant increase of the coordination number for the Pt-Pt (N_{Pt-Pt}) contribution and the Pt-O (N_{Pt-O}) contribution disappeared indicating that the sample agglomerated. This corroborates the important role of Ce on the particles stability that depends on the metal particle size, on the

atmosphere and the temperature. The samples 12Ce03PtAl and 12Ce1PtAl, at 350 ^{0}C, presented both, Pt-Pt and Pt-O contributions, demonstrating the stability.

Table 15: Structural parameters obtained from EXAFS analysis of the catalysts at 250 ^{0}C and different atmospheres.

H_2				
	03PtAl	**12Ce03PtAl**	**1PtAl**	**12Ce1PtAl**
N_{Pt-Pt}	6[a]	2[b]	8[a]	2[a]
R_{Pt-Pt}	2.730[c]			
N_{Pt-Os}	1.4[b]	3[a]	--	1.2[b]
R_{Pt-Os}	2.06[c]			
N_{Pt-OL}	2[b]	5[a]	--	4[b]
R_{Pt-OL}	2.53[c]			
SS_{Pt} / SS_{Pt-O}	0.011[a]			
WGS				
	03PtAl	**12Ce03PtAl**	**1PtAl**	**12Ce1PtAl**
N_{Pt-Pt}	8[a]	0.4[b]	10[a]	3[a]
R_{Pt-Pt}	2.760[c]			
N_{Pt-Os}	1.6[b]	4[a]	--	1.3[b]
R_{Pt-Os}	2.05[c]			
N_{Pt-OL}	2[b]	7[a]	--	4[b]
R_{Pt-OL}	2.55[c]			
SS_{Pt} / SS_{Pt-O}	0.013[a]			
H_2-2º				
	03PtAl	**12Ce03PtAl**	**1PtAl**	**12Ce1PtAl**
N_{Pt-Pt}	6[a]	3[b]	8[a]	2[a]
R_{Pt-Pt}	2.740[c]			
N_{Pt-Os}	1.5[b]	2[a]	--	1.3[b]
R_{Pt-Os}	2.06[c]			
N_{Pt-OL}	3[b]	4[a]	--	4[b]
R_{Pt-OL}	2.52[c]			
SS_{Pt} / SS_{Pt-O}	0.011[a]			

E_{0Pt-Pt} = 8; E_{0Pt-O} = 6; S_0^2 = 0.9 a = error about 10%; b = error about 20%; c = error about 1%

At 350 ^{0}C, when the atmosphere was changed from hydrogen to WGS the Pt-Pt contribution disappeared for the catalyst 12Ce03PtAl. However, the Pt-O_s contribution increased (from N_{Pt-Os} = 3 and N_{Pt-OL} = 5 under H_2 to N_{Pt-Os} = 5 and N_{Pt-OL} = 10 under WGS). For the sample 6Ce1PtAl a reversible increase, in the coordination number, was also observed changing from H_2 to WGS probably indicating morphological changes depending on the atmosphere. The stability and Pt-O contribution was also observed for the sample 12Ce1PtAl. However the variations

depending on the atmosphere were smaller from 12Ce1PtAl than 12Ce03PtAl probably due to the differences in particle size.

Concerning the bond distances, no significant variations are observed changing the atmosphere for both temperatures. Although a bond distance contraction is expected due the small particle size, a relaxation is observed. This is due to the gases adsorption that leads to a bond distance increase and cause like a compensation phenomenon in relation to the contraction that would be expected. Thus, it is important to highlight that Ce contributes for the particles stability, observed through Pt-O contribution, but that this is also proportional to the Pt amount.

Table 16: Structural parameters obtained from EXAFS analysis of the catalysts at 350 ^{0}C and different atmospheres.

H_2				
	03PtAl	**12Ce03PtAl**	**6Ce1PtAl**	**12Ce1PtAl**
N_{Pt-Pt}	7[a]	1[b]	5[a]	2[a]
R_{Pt-Pt}	2.71[c]			
N_{Pt-Os}	--	3[a]	--	3[b]
R_{Pt-Os}	2.06[c]			
N_{Pt-OL}	--	5[a]	--	2[b]
R_{Pt-OL}	2.54[c]			
SS_{Pt} / SS_{Pt-O}	0.011[a]			
WGS				
	03PtAl	**12Ce03PtAl**	**6Ce1PtAl**	**12Ce1PtAl**
N_{Pt-Pt}	11[a]	--	9[a]	2[a]
R_{Pt-Pt}	2.759[c]			
N_{Pt-Os}	--	5[a]	--	2.4[b]
R_{Pt-Os}	2.08[c]			
N_{Pt-OL}	--	10[a]	--	5[b]
R_{Pt-OL}	2.53[c]			
SS_{Pt} / SS_{Pt-O}	0.015[a]			
H_2-2º				
	03PtAl	**12Ce03PtAl**	**6Ce1PtAl**	**12Ce1PtAl**
N_{Pt-Pt}	--	2[b]	6[a]	3[a]
R_{Pt-Pt}	2.715[c]			
N_{Pt-Os}	--	2[a]	--	1[b]
R_{Pt-Os}	2.05[c]			
N_{Pt-OL}	--	4[a]	--	4[b]
R_{Pt-OL}	2.52[c]			
SS_{Pt} / SS_{Pt-O}	0.011[a]			

E_{0Pt-Pt} = 8; E_{0Pt-O} = 6 S_0^2 = 0.9 a = error about 10%; b = error about 20%; c = error about 1%.

To investigate the electronic properties of the catalysts XANES at Pt edge was measured under different atmospheres. It has been suggested in the literature that the feature at 8 eV (relative to the edge) in the delta XANES for Pt L_2-edge ($\Delta\mu_{L2}$) is more suitable to determine the hydrogen coverage [92]. Figure 28 presents the $\Delta\mu_{L2}$ for the catalyst 12Ce1PtAl under hydrogen and CO at different temperatures. As expected the gas coverage for both atmospheres decreases with the temperature. For both gases and all temperatures the sample presents Atop sites features [92] similar to the sample 12Ce1PtAl presented at Figure 28. The feature under CO (Figure 28B) is more intense than under hydrogen (Figure 28A), for the same temperatures. The intensity under CO is higher due to the CO higher heat of adsorption compared to hydrogen thus the surface presents a higher coverage under CO [91]. Further, under H_2 at 450 ^{0}C $\Delta\mu_{L2}$ is zero showing that no hydrogen is adsorbed on Pt at this temperature. This confirmed our approach of subtract each spectrum from the spectrum measured under H_2 at 500 ^{0}C.

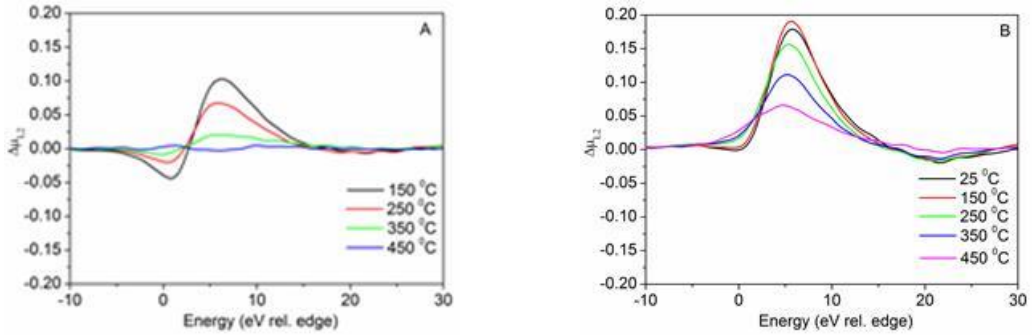

Figure 28. $\Delta\mu_{L2}$ for 12Ce1PtAl under (A) H_2 and (B) CO.

Figure 29 presents the $\Delta\mu_{L3}$ for the sample 03PtAl at 250 ^{0}C and 350 ^{0}C under different atmospheres. Nfold sites can be observed for all atmospheres and both temperatures. As expected the gases coverage at 250 ^{0}C is higher than 350 ^{0}C. The gases coverage increased as follow: WGS > CO > H_2.

The $\Delta\mu_{L3}$ for 12Ce03PtAl catalyst can be seen in Figure 30. Contrary from the sample 03PtAl different sites appear depending on the atmosphere and the temperature. At 250 ^{0}C under hydrogen almost no coverage is observed. Under WGS and CO a signature of atop sites can be observed. At 350 ^{0}C a shift to the left is observed compared to 250 ^{0}C. Ramaker et al [177] using delta XANES technique compared the adsorption of H and O on Pt and observed a left shift for O/Pt when

compared with H/Pt (2-4 eV lower for Pt/O). Thus, this shift of 4eV to lower energy at higher temperature could be related with an interaction between the platinum and the support.

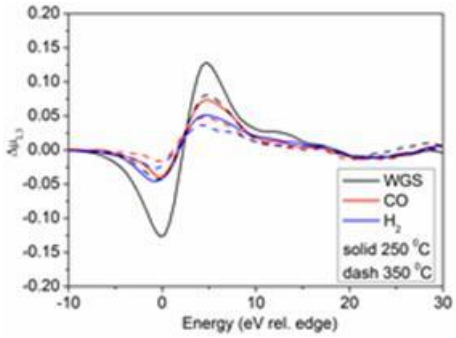

Figure 29. $\Delta\mu_{L3}$ for 03PtAl at 250 ^{0}C and 350 ^{0}C under different atmospheres.

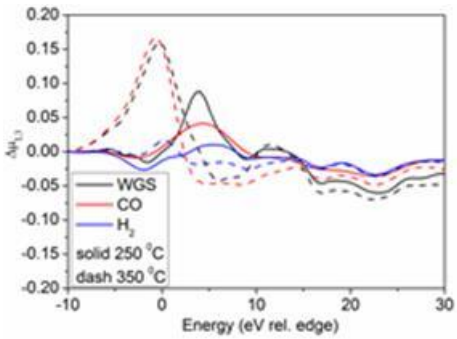

Figure 30. $\Delta\mu_{L3}$ for 12Ce03PtAl at 250 ^{0}C and 350 ^{0}C under different atmospheres.

For the sample 6Ce1PtAl Nfold sites appear (Figure 31) as for the sample 03PtAl. However the features are more intense for 6Ce1PtAl than for 03PtAl.

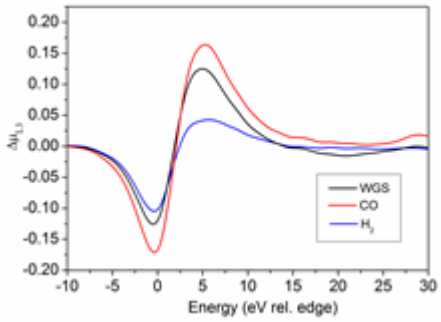

Figure 31. $\Delta\mu_{L3}$ for 6Ce1PtAl at 350 ^{0}C under different atmospheres.

For the sample 12Ce1PtAl different sites appeared according the atmosphere and the temperature (Figure 32). As observed for other samples, the coverage is higher at 250 than 350 ^{0}C. For H_2 and CO, Nfold sites can be seen interestingly, for WGS atop sites are formed. The formation of atop sites can be related to water adsorption [91]. An energy shift to low energy was observed for the Nfold sites

for 12Ce1PtAl as was observed for 12Ce03PtAl. However, 12Ce1PtAl presents a smaller displacement (-2 eV) compared to 12Ce03PtAl (-4 eV) that can be related with the particle size/morphology. The sample 12Ce03PtAl probably is smaller or flatter than 12Ce1PtAl and would be more susceptible to the water influence. Further, it has been demonstrated in the literature [25–27] that the signature curves are affected for OH adsorption on Pt that is near another atom. The curves are shifted to lower energies. Thus, probably both samples (12Ce1PtAl and 12Ce03PtAl) are being affected by a metal support interaction but this interface is higher for 12Ce03PtAl due to the particle morphology and the sites that are formed since it presents a higher shift.

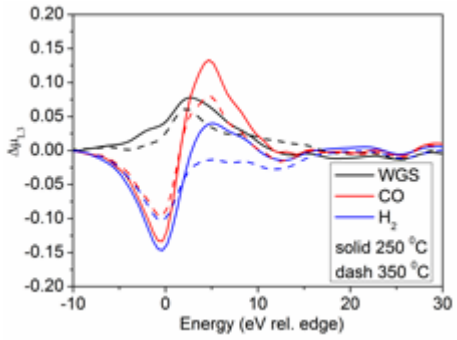

Figure 32. $\Delta\mu_{L3}$ for 12Ce1PtAl at 250 ^{0}C and 350 ^{0}C under different atmospheres.

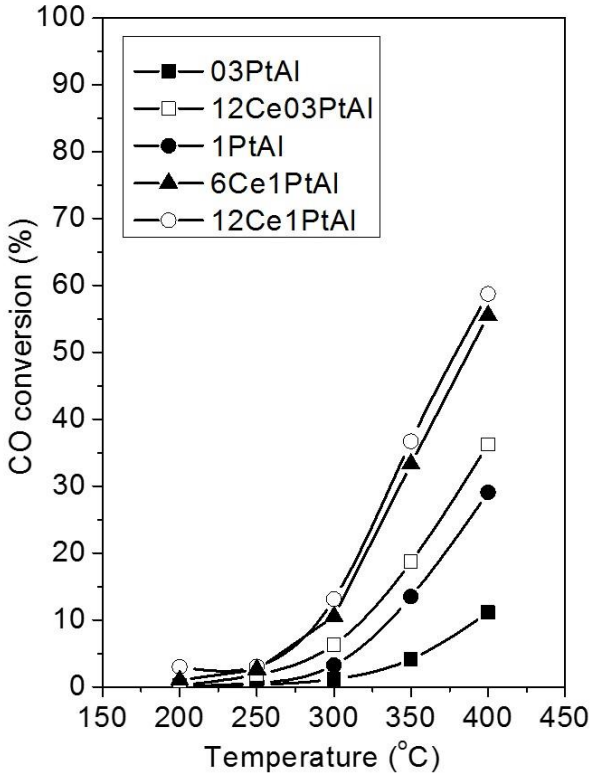

Figure 33. WGS reaction catalytic test H_2O:CO ratio 3:1.

Figure 33 shows the results for the catalytic tests under WGS as a function of temperature. The CO conversion is higher for the samples with Ce compared with the sample without Ce and the activity also increases with the Pt loading. The TOF results, for direct reaction, are presented in Table 17. It is possible to observe that the cerium increases the TOF comparing the samples with and without cerium and that the samples with 0.3% of platinum presents a better TOF compared to the sample with 1% due to the higher dispersion.

Table 17: Turn over frequency (TOF) for the forward reaction.

TOF (s^{-1})	03PtAl	12Ce03PtAl	1PtAl	6Ce1PtAl	12Ce1PtAl
250 ^{0}C	0.007	0.04	0.004	0.02	0.02
350 ^{0}C	0.03	0.15	0.02	0.08	0.11

II.11. Discussion

For structure sensitive reactions, like the WGS reaction, the catalytic activity is directly related to the particle size and thus with the sites that are present at the surface. The WGS reaction can occur over a Pt metal surface [33], involving the adsorption of CO and dissociation of H_2O, with the sites adjacent to Pt being essential for the catalysis effectivity. The use of CeO_2 and alkalis has been found to improve the activity of supported Pt catalysts [140] [185]. The presence of CeO_2 can promote the WGS [185], and DFT calculations have demonstrated that the dissociation of H_2O on Pt nanoparticles is an exothermic process. The interaction of Pt clusters with CeO_2 (111) or $Ce_{40}O_{80}$ nanoparticles results in changes of reactivity, favoring the dissociation of water, an important step for the WGS reaction [151].

To address the behavior of platinum-ceria-alumina catalysts samples with small particle size were prepared and their stability was demonstrated through the EXAFS results. The Pt diffusive motion, which is directly related to the particle stability, depends on the Pt-O bond, the nature of the support, and nanoparticle size. Monte Carlo simulations, for the reaction kinetics, indicates that the Pt atom can be trapped at certain γ-Al_2O_3 surface regions at low temperatures (<500 K), and the adsorption is weaker on a hydrated surfaces [186]. DFT/molecular dynamics studies indicate that the electronic and structural properties of Pt nanoparticles depend on the nature of the support and the atmosphere [187] [188]. Pt_{10}/γ-Al_2O_3 displays complex structural dynamics on multiple time scales, including vibrational motion on the center of mass and fluctuating bonding characteristics. When Pt is used on ceria-based supports in

the presence of oxygen, Pt oxide species are formed and are trapped on ceria surface through a relatively strong Pt-O-Ce interaction. Under reducing conditions, Pt-O-Ce interaction is reduced, forming small Pt^0 particles [189]. These studies suggested that the presence of ceria promotes a strong Pt-O-Ce interaction, and due to this interaction small stable particles are formed, depending on the reduction potential of the reactants. This is in agreement on what was observed for our samples.

As mentioned above, the catalyst oxi/reduction properties, are very sensitive to three factors: (i) the platinum particle size, (ii) the amount of CeO_2 and (iii) the possibility for both being in contact. Thus, using as an advantage, the high dispersion and stability of our samples it was possible to use the ΔXANES technique to evaluate changes caused by gas adsorption on the metal surface [91], since like this the bulk properties would be more similar with the surface properties and the study using a bulk technique like XAFS would be more sensitive.

N-fold sites were observed for 03PtAl, 1PtAl (not shown) and 6Ce1PtAl. Atop sites were observed for 12Ce1PtAl and 12Ce03PtAl. The formation of different surface sites is related with the SMSI. For highly dispersed Pt, single-atom Pt supported on FeO_x (Pt_1/FeO_x) has been shown to be highly active and stable for CO oxidation [189]. The transfer of electrons from Pt atoms to the FeOx surface is responsible for the strong binding and the stabilization of Pt_1/FeO_x samples. The partially vacant 5d orbitals of the positively charged species can help to reduce both the CO adsorption energy and the activation barrier for CO oxidation [84].

The sample 12Ce03PtAl presented a higher shift to lower energy for the ΔXANES result probably due to a strong interaction with water and/or with the support. The dissociation of H_2O on Pt sites is an essential step of the reaction [86]. The activation of H_2O can occur on the support surface or at the Pt-support interface, which can affect the reaction pathways for supported Pt catalysts. Energy profiles for the dissociation of water, calculated using DFT, demonstrated that an endothermic process occurs on Pt (111) [36], which is favored by low coordination Pt sites formed by decreasing the size of metal nanoparticles [36]. Nevertheless, experimental data for Pt/Al_2O_3 catalysts suggest that the TOF values for the WGS do not change significantly with Pt dispersion [33].

Following the same approach of Guo et al. [29] to identify the species at the surface during the reaction we subtracted the ΔμL3 under WGS from ΔμL3 under CO and the results are presented in Figure 34.

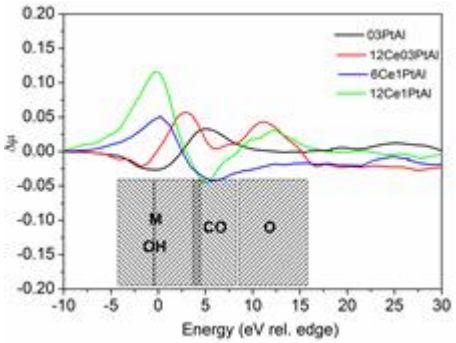

Figure 34. Result obtained from the subtraction from ΔμL3 under WGS from ΔμL3 under CO.

For the 03PtAl sample the same shape of CO curve is obtained subtracting the WGS curve from CO curve showing that the CO is the main specie on the surface of this sample during the reaction (as for 1PtAl at 250 ^{0}C, once it was not measured at 350 ^{0}C). Guo et al. [90] found for Pt/SiO_2 catalysts that the major surface specie under WGS reaction was CO (70%) while water was responsible just for 10% of adsorption.

Guo et al. [90] also simulated a ΔXANES spectra for CO and OH adsorbed on Pt(111). They found that the feature relative to OH adsorption is between -4 and 6 eV relative to the edge. For the sample 12Ce03PtAl is where we have a contribution. However, it was also found in the literature [91] that the OH adsorption changes when there is a “foreign” atom near Pt and the feature goes to lower energies. This feature at lower energies was observed for the samples 6Ce1PtAl and 12Ce1PtAl. Thus, considering that XAFS is an average technique, for the sample 12Ce03PtAl, due to the small amount of platinum, is more difficult to identify the signal relative to the Pt in contact with a foreign atom and in this case the contribution due to the signal from water adsorption is more intense. However, for the samples 6Ce1PtAl and 12Ce1PtAl there are more Pt atoms neighbors to Ce which causes an increase in the signal relative to this contribution leading this energy shift to the left, observed for the feature at ΔXANES result.

Furthermore, for the samples 12Ce03PtAl and 12Ce1PtAl due to the higher amount of CeO_2 the feature relative to O contribution (above 5 eV [91]) is more intense. These results are in agreement with EXAFS results where it was found a

higher Pt-O contribution for these samples. Thus, for small particles the active phase is a mixture between the oxide and the metallic phase while increasing the particle size just a metallic contribution is observed.

As can be seen above the active sites are depend on the metallic particle size and the metal-support interaction. The presence of a specific active site may be related with the occurrence of different mechanism reactions and due to this there is no consensus as to whether an associative mechanism or a redox mechanism is the main pathway for WGS reaction.

II.12. Conclusion – Part II

In situ characterization is very important to understand the catalytic properties since it is possible to evaluate the catalyst structure and electronic properties under real conditions.

The SMSI due to Ce impregnation on Pt/Al_2O_3 samples was demonstrated. The addition of ceria further oxidizes the catalyst before the reduction and makes it more stable at high temperature reducing the PtO_x mobility. The coordination numbers for the samples without Ce increased after thermal treatments. Morphological changes of the particles were observed by changes in the coordination numbers as a function of the temperature.

Different types of catalytic sites appeared depending on the platinum particle size and the interaction with ceria. The samples without Ce or with a “small” amount (6%) favored n-fold sites. For the samples with a larger amount of Ce (12%) different sites appeared depending on the temperature and atmosphere. The Pt-Ce interaction is probably higher in the 12Ce03PtAl catalyst compared to the other samples, leading to more pronounced morphological changes. The higher catalytic activity in the presence of ceria is probably due to a combination of highly dispersed Pt particles and Pt-O-Ce interaction promoting the activation of H_2O on Pt and ceria. This study about the properties of the highly dispersed Pt-based catalyst contributes to an understanding of the nanoscale properties of oxide-metal interfaces, as well as the way in which catalytic properties are influenced by factors such as nanoparticle size, oxidation potentials of the reactants, nature of the support, and temperature.

13. General Conclusion

Catalysts are dynamic systems that change depending on the atmosphere and temperature. The use of *in situ* techniques is very important to characterize and understand the catalyst behavior since the properties under reaction conditions will differ from the properties measured before or after the reaction.

It was demonstrated the importance of cerium for the platinum catalysts due to the existence of Pt-O bonds that anchor the particles and avoid agglomeration. This metal-support interaction depended on the catalyst preparation method and the oxide phase that was formed (particle size and crystalline structure). Also, depending on this metal-support interaction, different active sites were formed influencing on the gases adsorption and consequently the reactivity.

The use of pre-formed nanoparticles was a good strategy to decrease the number of variables and evaluate the support properties. It was possible to observe that crystalline domain, structure formed, oxidation state are important parameters that will influence the catalytic activity and that depends on the preparation method. Distinguishing which parameter governs the catalytic activity revealed to be a difficult task.

To observe changes for the Pt structure it was necessary to decrease the metal particle size and a strong metal-support interaction through an oxygen bond was observed. Changes on the surface sites that are formed were observed depending on the metal and support particle size and their interaction. Several parameters that influence the catalyst behavior have been identified however more studies are necessary to identify the catalytic site and relate it to the reaction mechanism.

14. Suggestions for future work

* Oxide phase controlled synthesis combined with the controlled synthesis for the metallic nanoparticles. Thus, will be easier to identify and split the catalyst properties that are relative to the support or the metallic phase;

* Perform theoretical calculations to corroborate the experimental results;

* Perform the WGS reaction using reactants and products in the feed to be able to calculate the TOF accurately.

15. Bibliography

[1] J.J. Liu, Advanced Electron Microscopy of Metal-Support Interactions in Supported Metal Catalysts, ChemCatChem. 3 (2011) 934–948. doi:10.1002/cctc.201100090.

[2] Y. Nagai, T. Hirabayashi, K. Dohmae, N. Takagi, T. Minami, H. Shinjoh, S. Matsumoto, Sintering inhibition mechanism of platinum supported on ceria-based oxide and Pt-oxide-support interaction, Journal of Catalysis. 242 (2006) 103–109. doi:10.1016/j.jcat.2006.06.002.

[3] L.S.F. Feio, C.E. Hori, S. Damyanova, F.B. Noronha, W.H. Cassinelli, C.M.P. Marques, J.M.C. Bueno, The effect of ceria content on the properties of Pd/CeO2/Al2O3 catalysts for steam reforming of methane, Applied Catalysis A: General. 316 (2007) 107–116. doi:10.1016/j.apcata.2006.09.032.

[4] A.P. Ferreira, D. Zanchet, J.C.S. Araújo, J.W.C. Liberatori, E.F. Souza-Aguiar, F.B. Noronha, J.M.C. Bueno, The effects of CeO2 on the activity and stability of Pt supported catalysts for methane reforming, as addressed by in situ temperature resolved XAFS and TEM analysis, Journal of Catalysis. 263 (2009) 335–344. doi:10.1016/j.jcat.2009.02.026.

[5] P.J.S. Prieto, a. P. Ferreira, P.S. Haddad, D. Zanchet, J.M.C. Bueno, Designing Pt nanoparticles supported on CeO2–Al2O3: Synthesis, characterization and catalytic properties in the steam reforming and partial oxidation of methane, Journal of Catalysis. 276 (2010) 351–359. doi:10.1016/j.jcat.2010.09.025.

[6] J.W. Niemantsverdriet, Spectroscopy in Catalysis - an introduction, Wiley-VCH, 2007.

[7] A.T. Bell, The impact of nanoscience on heterogeneous catalysis., Science (New York, N.Y.). 299 (2003) 1688–91. doi:10.1126/science.1083671.

[8] A.I. Frenkel, C.W. Hills, R.G. Nuzzo, A view from the inside: Complexity in the atomic scale ordering of supported metal nanoparticles, Journal of Physical Chemistry B. 105 (2001) 12689–12703. doi:10.1021/jp012769j.

[9] A.I. Frenkel, M.W. Small, J.G. Smith, R.G. Nuzzo, K.O. Kvashnina, M. Tromp, An in Situ Study of Bond Strains in 1 nm Pt Catalysts and Their Sensitivities to Cluster − Support and Cluster − Adsorbate Interactions, (2013).

[10] B. Roldan Cuenya, M. Alcántara Ortigoza, L.K. Ono, F. Behafarid, S. Mostafa, J.R. Croy, K. Paredis, G. Shafai, T.S. Rahman, L. Li, Z. Zhang, J.C. Yang, Thermodynamic properties of Pt nanoparticles: Size, shape, support, and adsorbate effects, Physical Review B. 84 (2011) 245438. doi:10.1103/PhysRevB.84.245438.

[11] A. Patlolla, P. Baumann, W. Xu, S.D. Senanayake, J.A. Rodriguez, a. I. Frenkel, Characterization of Metal-Oxide Catalysts in Operando Conditions by Combining X-ray Absorption and Raman Spectroscopies in the Same Experiment, Topics in Catalysis. 56 (2013) 896–904. doi:10.1007/s11244-013-0053-y.

[12] P. Parthasarathy, K.S. Narayanan, Hydrogen production from steam gasification of biomass: Influence of process parameters on hydrogen yield – A review, Renewable Energy. 66 (2014) 570–579. doi:10.1016/j.renene.2013.12.025.

[13] R. Burch, A. Goguet, F.C. Meunier, A critical analysis of the experimental evidence for and against a formate mechanism for high activity water-gas shift

catalysts, Applied Catalysis A: General. 409–410 (2011) 3–12. doi:10.1016/j.apcata.2011.09.034.

[14] Meeting the Challenge: The U.S. Chemical Industry Faces the 21st Century ., in: DOC (U.S. Department of Commerce), Washington, D.C. : U.S. Department of Commerce, 1996.

[15] Various Analysts, 2013 CHEMICALS RESEARCH REVIEW - BCC Research, 2013.

[16] H. Balat, E. Kırtay, Hydrogen from biomass – Present scenario and future prospects, International Journal of Hydrogen Energy. 35 (2010) 7416–7426. doi:10.1016/j.ijhydene.2010.04.137.

[17] J. Chang, K. Lee, P. Lin, Biohydrogen production with ÿxed-bed bioreactors, International Journal of Hydrogen Energy. 27 (2002) 1167–1174.

[18] D.L. Trimm, Natural Gas: Conventional Steam-Reforming, Fuels - Hydrogen Production. (2009) 293–299.

[19] J.M. Thomas, An exceptionally active catalyst for generating hydrogen from water., Angewandte Chemie (International Ed. in English). 50 (2011) 49–50. doi:10.1002/anie.201006390.

[20] N.K. Sinha, M. Neurock, A first principles analysis of the hydrogenation of C1C4 aldehydes and ketones over Ru(0001), Journal of Catalysis. 295 (2012) 31–44. doi:10.1016/j.jcat.2012.07.018.

[21] K.G. Mbuyi, M.S. Scurrell, D. Hildebrandt, D. Glasser, Conversion of Synthesis Gas to Dimethylether Over Gold-based Catalysts, Topics in Catalysis. 55 (2012) 771–781. doi:10.1007/s11244-012-9865-4.

[22] J.M. Bermúdez, B. Fidalgo, a. Arenillas, J. a. Menéndez, Dry reforming of coke oven gases over activated carbon to produce syngas for methanol synthesis, Fuel. 89 (2010) 2897–2902. doi:10.1016/j.fuel.2010.01.014.

[23] J.M. Bermúdez, B. Fidalgo, a. Arenillas, J. a. Menéndez, CO2 reforming of coke oven gas over a Ni/γAl2O3 catalyst to produce syngas for methanol synthesis, Fuel. 94 (2012) 197–203. doi:10.1016/j.fuel.2011.10.033.

[24] Y. Yang, M.G. White, P. Liu, A Theoretical Study of Methanol Synthesis from CO2 Hydrogenation on Metal-Doped Cu(111) Surfaces., The Journal of Physical Chemistry. A. (2011) 248–256. doi:10.1021/jp208448c.

[25] S. Lögdberg, D. Tristantini, Ø. Borg, L. Ilver, B. Gevert, S. Järås, E. a. Blekkan, A. Holmen, Hydrocarbon production via Fischer–Tropsch synthesis from H2-poor syngas over different Fe-Co/γ-Al2O3 bimetallic catalysts, Applied Catalysis B: Environmental. 89 (2009) 167–182. doi:10.1016/j.apcatb.2008.11.037.

[26] M. Lualdi, S. Lögdberg, F. Regali, M. Boutonnet, S. Järås, Investigation of Mixtures of a Co-Based Catalyst and a Cu-Based Catalyst for the Fischer–Tropsch Synthesis with Bio-Syngas: The Importance of Indigenous Water, Topics in Catalysis. 54 (2011) 977–985. doi:10.1007/s11244-011-9719-5.

[27] G. Jacobs, U. Graham, E. Chenu, P. Patterson, A. Dozier, B. Davis, Low-temperature water-gas shift: impact of Pt promoter loading on the partial reduction of ceria and consequences for catalyst design, Journal of Catalysis. 229 (2005) 499–512. doi:10.1016/j.jcat.2004.11.031.

[28] B.S.R. J, I NTERNATIONAL J OURNAL OF C HEMICAL A Review of the Water Gas Shift Reaction Kinetics, (n.d.).

[29] C.M. Kalamaras, I.D. Gonzalez, R.M. Navarro, J.L.G. Fierro, A.M. Efstathiou, Effects of reaction temperature and support composition on the mechanism of water - Gas shift reaction over supported-Pt catalysts, Journal of Physical Chemistry C. 115 (2011) 11595–11610. doi:10.1021/jp201773a.

[30] R. Burch, Gold catalysts for pure hydrogen production in the water-gas shift reaction: activity, structure and reaction mechanism., Physical Chemistry Chemical Physics : PCCP. 8 (2006) 5483–500. doi:10.1039/b607837k.

[31] M. Flytzani-Stephanopoulos, B.C. Gates, Atomically dispersed supported metal catalysts., Annual Review of Chemical and Biomolecular Engineering. 3 (2012) 545–74. doi:10.1146/annurev-chembioeng-062011-080939.

[32] S. Aranifard, S.C. Ammal, A. Heyden, On the importance of metal–oxide interface sites for the water–gas shift reaction over Pt/CeO2 catalysts, Journal of Catalysis. 309 (2014) 314–324. doi:10.1016/j.jcat.2013.10.012.

[33] A.A. Phatak, N. Koryabkina, S. Rai, J.L. Ratts, W. Ruettinger, R.J. Farrauto, G.E. Blau, W.N. Delgass, F.H. Ribeiro, Kinetics of the water–gas shift reaction on Pt catalysts supported on alumina and ceria, Catalysis Today. 123 (2007) 224–234. doi:10.1016/j.cattod.2007.02.031.

[34] Q. Fu, H. Saltsburg, M. Flytzani-Stephanopoulos, Active nonmetallic Au and Pt species on ceria-based water-gas shift catalysts., Science (New York, N.Y.). 301 (2003) 935–8. doi:10.1126/science.1085721.

[35] A.A. Gokhale, J.A. Dumesic, M. Mavrikakis, On the mechanism of low-temperature water gas shift reaction on copper., Journal of the American Chemical Society. 130 (2008) 1402–14. doi:10.1021/ja0768237.

[36] A. Bruix, J.A. Rodriguez, P.J. Ramírez, S.D. Senanayake, J. Evans, J.B. Park, D. Stacchiola, P. Liu, J. Hrbek, F. Illas, A new type of strong metal-support interaction and the production of H2 through the transformation of water on Pt/CeO2(111) and Pt/CeO(x)/TiO2(110) catalysts., Journal of the American Chemical Society. 134 (2012) 8968–8974. doi:10.1021/ja302070k.

[37] C. Zerva, C.J. Philippopoulos, Ceria catalysts for water gas shift reaction: Influence of preparation method on their activity, Applied Catalysis B: Environmental. 67 (2006) 105–112. doi:10.1016/j.apcatb.2006.04.013.

[38] G.A. Somorjai, J.Y. Park, Colloid Science of Metal Nanoparticle Catalysts in 2D and 3D Structures. Challenges of Nucleation, Growth, Composition, Particle Shape, Size Control and Their Influence on Activity and Selectivity, Topics in Catalysis. 49 (2008) 126–135. doi:10.1007/s11244-008-9077-0.

[39] P. Dash, T. Bond, C. Fowler, W. Hou, N. Coombs, R.W.J. Scott, Rational Design of Supported PdAu Nanoparticle Catalysts from Structured Nanoparticle Precursors, The Journal of Physical Chemistry C. 113 (2009) 12719–12730. doi:10.1021/jp9037182.

[40] Y. Nagai, K. Dohmae, Y. Ikeda, N. Takagi, T. Tanabe, N. Hara, G. Guilera, S. Pascarelli, M.A. Newton, O. Kuno, H. Jiang, H. Shinjoh, S. Matsumoto, In situ redispersion of platinum autoexhaust catalysts: An on-line approach to increasing catalyst lifetimes?, Angewandte Chemie - International Edition. 47

(2008) 9303–9306. doi:10.1002/anie.200803126.

[41] G.N. Vayssilov, Y. Lykhach, A. Migani, T. Staudt, G.P. Petrova, N. Tsud, T. Skála, A. Bruix, F. Illas, K.C. Prince, V. Matolín, K.M. Neyman, J. Libuda, Support nanostructure boosts oxygen transfer to catalytically active platinum nanoparticles., Nature Materials. 10 (2011) 310–315. doi:10.1038/nmat2976.

[42] M. Hatanaka, N. Takahashi, T. Tanabe, Y. Nagai, K. Dohmae, Y. Aoki, T. Yoshida, H. Shinjoh, Ideal Pt loading for a Pt/CeO2-based catalyst stabilized by a Pt–O–Ce bond, Applied Catalysis B: Environmental. 99 (2010) 336–342. doi:10.1016/j.apcatb.2010.07.003.

[43] T.X.T. Sayle, S.C. Parker, D.C. Sayle, O. Systems, C. Down, Oxidising CO to CO 2 using ceria nanoparticles, Phys. Chem. Chem. Phys. 7 (2005) 2936–2941.

[44] H. Shinjoh, M. Hatanaka, Y. Nagai, T. Tanabe, N. Takahashi, T. Yoshida, Y. Miyake, Suppression of Noble Metal Sintering Based on the Support Anchoring Effect and its Application in Automotive Three-Way Catalysis, Topics in Catalysis. 52 (2009) 1967–1971. doi:10.1007/s11244-009-9371-5.

[45] T. Bunluesin, R.J. Gottea, G.W. Grahamb, Studies of the water-gas-shift reaction on ceria-supported Pt , Pd , and Rh : implications for oxygen-storage properties, Applied Catalysis B: Environmental. 15 (1998) 107–114. doi:10.1016/S0926-3373(97)00040-4.

[46] W.C. Chueh, C. Falter, M. Abbott, D. Scipio, P. Furler, S.M. Haile, A. Steinfeld, High-flux solar-driven thermochemical dissociation of CO2 and H2O using nonstoichiometric ceria., Science (New York, N.Y.). 330 (2010) 1797–801. doi:10.1126/science.1197834.

[47] E.S. Putna, T. Bunluesin, X.L. Fan, R.J. Gorte, Ceria films on zirconia substrates : models for understanding oxygen-storage properties, Catalysis Today. 50 (1999) 343–352.

[48] R.J. Gorte, S. Zhao, Studies of the water-gas-shift reaction with ceria-supported precious metals, Catalysis Today. 104 (2005) 18–24. doi:10.1016/j.cattod.2005.03.034.

[49] L. Yang, O. Kresnawahjuesa, R.J. Gorte, A calorimetric study of oxygen-storage in Pd / ceria and Pd / ceria – zirconia catalysts, Catalysis Letters. 72 (2001) 33–37.

[50] F. Zhang, P. Wang, J. Koberstein, S. Khalid, S.-W. Chan, Cerium oxidation state in ceria nanoparticles studied with X-ray photoelectron spectroscopy and absorption near edge spectroscopy, Surface Science. 563 (2004) 74–82. doi:10.1016/j.susc.2004.05.138.

[51] A. Migani, G.N. Vayssilov, S.T. Bromley, F. Illas, K.M. Neyman, Dramatic reduction of the oxygen vacancy formation energy in ceria particles: a possible key to their remarkable reactivity at the nanoscale, Journal of Materials Chemistry. 20 (2010) 10535. doi:10.1039/c0jm01908a.

[52] A. Migani, G.N. Vayssilov, S.T. Bromley, F. Illas, K.M. Neyman, Greatly facilitated oxygen vacancy formation in ceria nanocrystallites., Chemical Communications. 46 (2010) 5936–8. doi:10.1039/c0cc01091j.

[53] G.N. Vayssilov, A. Migani, K. Neyman, Density Functional Modeling of the Interactions of Platinum Clusters with CeO 2 Nanoparticles of Different Size,

Journal of Physical Chemistry C. 115 (2011) 16081–16086. doi:10.1021/jp204222k.

[54] J. Conesa, Computer modeling of surfaces and defects on cerium dioxide, Surface Science. 339 (1995) 337–352. doi:10.1016/0039-6028(95)00595-1.

[55] D.C. Sayle, S.A. Maicaneanu, G.W. Watson, Nanoparticles , Supported on Yttrium-Stabilized Zirconia, Journal of American Chemical Society. 2 (2002) 11429–11439. doi:10.1021/ja020657f.

[56] F. Esch, S. Fabris, L. Zhou, T. Montini, C. Africh, P. Fornasiero, G. Comelli, R. Rosei, Electron localization determines defect formation on ceria substrates., Science (New York, N.Y.). 309 (2005) 752–5. doi:10.1126/science.1111568.

[57] J.W. Chorkendorff, I. Niemantsverdriet, Concepts of Modern Catalysis and Kinetics, n.d.

[58] K.T. Rim, D. Eom, L. Liu, E. Stolyarova, J.M. Raitano, S.-W. Chan, M. Flytzani-Stephanopoulos, G.W. Flynn, Charging and Chemical Reactivity of Gold Nanoparticles and Adatoms on the (111) Surface of Single-Crystal Magnetite: A Scanning Tunneling Microscopy/Spectroscopy Study, The Journal of Physical Chemistry C. 113 (2009) 10198–10205. doi:10.1021/jp8112599.

[59] R.B. Duarte, M. Nachtegaal, J.M.C. Bueno, J. a. van Bokhoven, Understanding the effect of Sm2O3 and CeO2 promoters on the structure and activity of Rh/Al2O3 catalysts in methane steam reforming, Journal of Catalysis. 296 (2012) 86–98. doi:10.1016/j.jcat.2012.09.007.

[60] R.B. Duarte, S. Damyanova, D.C. de Oliveira, C.M.P. Marques, J.M.C. Bueno, Study of Sm2O3-doped CeO2–Al2O3-supported Pt catalysts for partial CH4 oxidation, Applied Catalysis A: General. 399 (2011) 134–145. doi:10.1016/j.apcata.2011.03.045.

[61] V.B. Mortola, S. Damyanova, D. Zanchet, J.M.C. Bueno, Surface and structural features of Pt/CeO2-La2O3-Al2O3 catalysts for partial oxidation and steam reforming of methane, Applied Catalysis B: Environmental. 107 (2011) 221–236. doi:10.1016/j.apcatb.2011.07.012.

[62] A. Barrera, M. Viniegra, P. Bosch, V.H. Lara, S. Fuentes, Pd / Al 2 O 3 -La 2 O 3 catalysts prepared by sol – gel : characterization and catalytic activity in the NO reduction by H 2, 34 (2001) 97–111.

[63] D. a. Ward, E.I. Ko, Preparing Catalytic Materials by the Sol-Gel Method, Industrial & Engineering Chemistry Research. 34 (1995) 421–433. doi:10.1021/ie00041a001.

[64] D. Pierre, W. Deng, M. Flytzani-Stephanopoulos, The Importance of Strongly Bound Pt–CeO x Species for the Water-gas Shift Reaction: Catalyst Activity and Stability Evaluation, Topics in Catalysis. 46 (2007) 363–373. doi:10.1007/s11244-007-9013-8.

[65] W. Deng, M. Flytzani-Stephanopoulos, On the issue of the deactivation of Au-ceria and Pt-ceria water-gas shift catalysts in practical fuel-cell applications., Angewandte Chemie (International Ed. in English). 45 (2006) 2285–9. doi:10.1002/anie.200503220.

[66] G. Kyriakou, M.B. Boucher, A.D. Jewell, E.A. Lewis, T.J. Lawton, A.E. Baber, H.L. Tierney, M. Flytzani-stephanopoulos, E.C.H. Sykes, Heterogeneous

Hydrogenations, Science. 335 (2012) 1209–1212.

[67] C. Wheeler, The water–gas-shift reaction at short contact times, Journal of Catalysis. 223 (2004) 191–199. doi:10.1016/j.jcat.2004.01.002.

[68] A. Luengnaruemitchai, S. Osuwan, E. Gulari, Comparative studies of low-temperature water–gas shift reaction over Pt/CeO2, Au/CeO2, and Au/Fe2O3 catalysts, Catalysis Communications. 4 (2003) 215–221. doi:10.1016/S1566-7367(03)00036-0.

[69] J. a Rodriguez, J. Graciani, J. Evans, J.B. Park, F. Yang, D. Stacchiola, S.D. Senanayake, S. Ma, M. Pérez, P. Liu, J. Fdez Sanz, J. Hrbek, Water-gas shift reaction on a highly active inverse CeOx/Cu111 catalyst: unique role of ceria nanoparticles., Angewandte Chemie (International Ed. in English). 48 (2009) 8047–50. doi:10.1002/anie.200903918.

[70] D.W. Flaherty, W.-Y. Yu, Z.D. Pozun, G. Henkelman, C.B. Mullins, Mechanism for the water–gas shift reaction on monofunctional platinum and cause of catalyst deactivation, Journal of Catalysis. 282 (2011) 278–288. doi:10.1016/j.jcat.2011.06.024.

[71] I.D. González, R.M. Navarro, W. Wen, N. Marinkovic, J.A. Rodriguéz, F. Rosa, J.L.G. Fierro, A comparative study of the water gas shift reaction over platinum catalysts supported on CeO2, TiO2 and Ce-modified TiO2, Catalysis Today. 149 (2010) 372–379. doi:10.1016/j.cattod.2009.07.100.

[72] G.-M. Schwab, Chemical Effects at the Solid / Solid Phase Boundary, Journal of Colloid and Interface Science. 34 (1970) 337–342.

[73] S.J. Tauster, S.C. Fung, R.L. Garten, Strong Metal-Support Interactions . Group 8 Noble Metals Supported on Ti02, Journal of the American Chemical Society. 100 (1978) 170–175.

[74] S.J. Tauster, Strong metal-support interactions, Accounts of Chemical Research. 20 (1987) 389–394. doi:10.1021/ar00143a001.

[75] G.L. Haller, D.E. Resasco, Metal-Support Interaction : Group Vlll Metals and Reducible Oxides, Advances in Catalysis. 36 (1989) 173–235.

[76] C.T. Campbell, Catalyst-support interactions: Electronic perturbations., Nature Chemistry. 4 (2012) 597–8. doi:10.1038/nchem.1412.

[77] P. Company, T. Nelherlunds, XPS investigations of Pt and Rh supported on g-Al2O3 and TiO2, Surface Science. 135 (1983) 580–596.

[78] M.C. Gordon, M. B.; Cyrot-Lackmann, F.; Desjonquères, Relaxation and stability of small transition metal particles, Surface Science. 80 (1979) 159–164.

[79] C.H. Hu, C. Chizallet, C. Mager-Maury, M. Corral-Valero, P. Sautet, H. Toulhoat, P. Raybaud, Modulation of catalyst particle structure upon support hydroxylation: Ab initio insights into Pd13 and Pt13/γ-Al2O3, Journal of Catalysis. 274 (2010) 99–110. doi:10.1016/j.jcat.2010.06.009.

[80] J. a. Wang, T. López, X. Bokhimi, O. Novaro, Phase composition, reducibility and catalytic activity of Rh/zirconia and Rh/zirconia-ceria catalysts, Journal of Molecular Catalysis A: Chemical. 239 (2005) 249–256. doi:10.1016/j.molcata.2005.06.021.

[81] L.F. Liotta, a. Longo, a. Macaluso, a. Martorana, G. Pantaleo, a. M. Venezia,

G. Deganello, Influence of the SMSI effect on the catalytic activity of a Pt(1%)/Ce0.6Zr0.4O2 catalyst: SAXS, XRD, XPS and TPR investigations, Applied Catalysis B: Environmental. 48 (2004) 133–149. doi:10.1016/j.apcatb.2003.10.001.

[82] S.E. Golunski, H.A. Hatcher, R.R. Rajaram, T.J. Truex, Origins of low-temperature three-way activity in PtKeO , Applied Catalysis B: Environmental. 5 (1995) 367–376.

[83] N. Acerbi, S.C. Tsang, S. Golunski, P. Collier, A practical demonstration of electronic promotion in the reduction of ceria coated PGM catalysts, Chemical Communications. (2008) 1578–1580. doi:10.1039/b718956g.

[84] B. Qiao, A. Wang, X. Yang, L.F. Allard, Z. Jiang, Y. Cui, J. Liu, J. Li, T. Zhang, Single-atom catalysis of CO oxidation using Pt1/FeOx., Nature Chemistry. 3 (2011) 634–41. doi:10.1038/nchem.1095.

[85] P. Sonström, D. Arndt, X. Wang, V. Zielasek, M. Bäumer, Ligand Capping of Colloidally Synthesized Nanoparticles-A Way to Tune Metal-Support Interactions in Heterogeneous Gas-Phase Catalysis, Angewandte Chemie International Edition. 50 (2011) 3888–3891. doi:10.1002/anie.201004573.

[86] J.A. Rodriguez, J.C. Hanson, D. Stacchiola, S.D. Senanayake, In situ/operando studies for the production of hydrogen through the water-gas shift on metal oxide catalysts., Physical Chemistry Chemical Physics : PCCP. 15 (2013) 12004–25. doi:10.1039/c3cp50416f.

[87] S. Bordiga, E. Groppo, G. Agostini, J.A. Van Bokhoven, C. Lamberti, Reactivity of Surface Species in Heterogeneous Catalysts Probed by In Situ X ‐ ray Absorption Techniques, Chemical Reviews. 113 (2013) 1736–1850. doi:10.1021/cr2000898.

[88] G. Agostini, E. Groppo, A. Piovano, R. Pellegrini, G. Leofanti, C. Lamberti, Preparation of Supported Pd Catalysts : From the Pd Precursor Solution to the Deposited Pd 2 þ Phase, Langmuir. 26 (2010) 11204–11211. doi:10.1021/la1005117.

[89] Y. Nagai, K. Dohmae, Y. Ikeda, N. Takagi, N. Hara, T. Tanabe, G. Guilera, S. Pascarelli, M. a. Newton, N. Takahashi, H. Shinjoh, S. Matsumoto, In situ observation of platinum sintering on ceria-based oxide for autoexhaust catalysts using Turbo-XAS, Catalysis Today. 175 (2011) 133–140. doi:10.1016/j.cattod.2011.02.046.

[90] J.T. Guo, Neng; Fingland, Bradley R.; Williams, W. Damion; Kispersky, Vincent F.; Jelic, Jelena; Delgass, W. Nicholas; Ribeiro, Fabio H.; Meyerc; Randall J. and Miller, Determination of CO, H2O and H2 coverage by XANES and EXAFS on Pt and Au during water gas shift reaction, Physical Chemistry Chemical Physics : PCCP. 12 (2010) 5678–5693. doi:10.1039/b926434e.

[91] J.J. Rehr, J.J. Kas, F.D. Vila, M.P. Prange, K. Jorissen, Parameter-free calculations of X-ray spectra with FEFF9., Physical Chemistry Chemical Physics : PCCP. 12 (2010) 5503–13. doi:10.1039/b926434e.

[92] Y. Ji, V. Koot, a Vandereerden, B. Weckhuysen, D. Koningsberger, D. Ramaker, A three-site Langmuir adsorption model to elucidate the temperature, pressure, and support dependence of the hydrogen coverage on supported Pt particles, Journal of Catalysis. 245 (2007) 415–427. doi:10.1016/j.jcat.2006.10.028.

[93] D. Meira, Síntese e caracterização de nanocatalisadores de platina suportados aplicados à reação de reforma do metano, Universidade Federal de São Carlos, 2010.

[94] T. Lo, R.R. Go, R. Bokhimi, S.A. Morales, O.S. Novaro, X-Ray Diffraction , FTIR , and NMR Characterization of Sol — Gel Alumina Doped with Lanthanum and Cerium, Journal of Solid State Chemistry. 128 (1997) 161–168.

[95] D. Wang, Y. Kang, V. Doan-Nguyen, J. Chen, R. Küngas, N.L. Wieder, K. Bakhmutsky, R.J. Gorte, C.B. Murray, Synthesis and oxygen storage capacity of two-dimensional ceria nanocrystals., Angewandte Chemie (International Ed. in English). 50 (2011) 4378–81. doi:10.1002/anie.201101043.

[96] G. Guilera, B. Gorges, S. Pascarelli, H. Vitoux, M. a Newton, C. Prestipino, Y. Nagai, N. Hara, Novel high-temperature reactors for in situ studies of three-way catalysts using turbo-XAS., Journal of Synchrotron Radiation. 16 (2009) 628–34. doi:10.1107/S0909049509026521.

[97] L.I. Smith, A tutorial on Principal Components Analysis Introduction, 2002.

[98] B. Ravel, M. Newville, ATHENA, ARTEMIS, HEPHAESTUS: data analysis for X-ray absorption spectroscopy using IFEFFIT., Journal of Synchrotron Radiation. 12 (2005) 537–41. doi:10.1107/S0909049505012719.

[99] S.X. CALVIN, S., LUO, Comparison of extended x-ray absorption fine structure and Scherrer analysis of x-ray diffraction as methods for determining mean sizes of polydisperse nanoparticles., Applied Physics Letters. 87 (2005) 2331021–2331023.

[100] A.M. Shahin, F. Grandjean, G.J. Long, T.P. Schuman, Cerium L III -Edge XAS Investigation of the Structure of Crystalline and Amorphous Cerium Oxides, Chem. Mater. 17 (2005) 315–321.

[101] A. Bianconi, H. Dexpert, A. Kotani, T. Ce, Specific intermediate-valence state of insulating 4f compounds detected by L3 x-ray absorption, Physical Review B. 35 (1987) 806–812. doi:10.1103/PhysRevB.35.806.

[102] P. Nachimuthu, W.-C. Shih, R.-S. Liu, L.-Y. Jang, J.-M. Chen, The Study of Nanocrystalline Cerium Oxide by X-Ray Absorption Spectroscopy, Journal of Solid State Chemistry. 149 (2000) 408–413. doi:10.1006/jssc.1999.8566.

[103] M.J. Douillard, L.; Gautier, M.; Thromat, N.; Henriot, M.; Guittet, Local electronic structure of Ce-doped Y2O3: An XPS and XAS study., Physical Review B. 49 (1994) 16171–16180. doi:10.1103/PhysRevB.49.16171.

[104] G. Hu, Z.; Bertram, S.; Kaindl, X-ray absorption study of PrO2 at high pressure, Physical Review B. 49 (1994) 39–43.

[105] L. Dexpert, H.; Karnatak, R.C.; Esteva, J. M.; Connerade, J. P.; Gasbnier, M.; Caro, P. E.; Albert, X-ray absorption studies of CeO2, PrO2 and TbO2. II. Rare-earth valence state by LIII absorption edges., Physical Review B. 36 (1987) 1750–1753. doi:10.1103/PhysRevB.36.1750.

[106] A. Soldatov, A. V.; Ivanchenko, T. S.; Della Longa, S.; Kotani, A.; Iwamoto, Y.; Bianconi, Crystal-structure effects in the Ce L3-edge x-ray absorption spectrum of CeO2: Multiple-scattering resonances and many-body final states., Physical Review B. 50 (1994) 5074–5080. doi:10.1103/PhysRevB.50.5074.

[107] E. V. Kaindl, G.; Schmiester, G.; Sampathkumaran, Pressure-induced changes

in LIII x-ray absorption near-edge structure of CeO2 and CeF4: Relevance of 4f-electronic structure, Physical Review B. 38 (1988) 10174–10177. doi:10.1103/PhysRevB.38.10174.

[108] J. Zhang, Z. Wu, T. Liu, T. Hu, Z. Wu, X. Ju, XANES study on the valence transitions in cerium oxide nanoparticles, Journal of Synchrotron Radiation. 8 (2001) 531–532. doi:10.1107/S0909049500016022.

[109] V. Fernandes, P. Schio, a J. a de Oliveira, W. a Ortiz, P. Fichtner, L. Amaral, I.L. Graff, J. Varalda, N. Mattoso, W.H. Schreiner, D.H. Mosca, Ferromagnetism induced by oxygen and cerium vacancies above the percolation limit in CeO2., Journal of Physics. Condensed Matter : An Institute of Physics Journal. 22 (2010) 216004 (8pp). doi:10.1088/0953-8984/22/21/216004.

[110] C. Hennig, Evidence for double-electron excitations in the L3-edge x-ray absorption spectra of actinides, Physical Review B. 75 (2007) 35120-1-35120–7. doi:10.1103/PhysRevB.75.035120.

[111] M.G. Solera, J. A.; García, J.; Proietti, Multielectron excitations at the I. edges in rare-earth ionic aqueous solutions, Physical Review B. 51 (1995) 2678–2686.

[112] R.U. Ribeiro, D.M. Meira, C.B. Rodella, D.C. Oliveira, J.M.C. Bueno, D. Zanchet, Probing the stability of Pt nanoparticles encapsulated in sol–gel Al2O3 using in situ and ex situ characterization techniques, Applied Catalysis A: General. 485 (2014) 108–117. doi:10.1016/j.apcata.2014.07.039.

[113] A. Bruix, A. Migani, G.N. Vayssilov, K.M. Neyman, J. Libuda, F. Illas, Effects of deposited Pt particles on the reducibility of CeO2(111)., Physical Chemistry Chemical Physics : PCCP. 13 (2011) 11384–92. doi:10.1039/c1cp20950g.

[114] M. Happel, J. Mysliveček, V. Johánek, F. Dvořák, O. Stetsovych, Y. Lykhach, V. Matolín, J. Libuda, Adsorption sites, metal-support interactions, and oxygen spillover identified by vibrational spectroscopy of adsorbed CO: A model study on Pt/ceria catalysts, Journal of Catalysis. 289 (2012) 118–126. doi:10.1016/j.jcat.2012.01.022.

[115] D.U. D. Zanchet, H. Tolentino, M.C. Martins Alves, O.L. Alves, Inter-atomic distance contraction in thiol-passivated gold nanoparticles, Chemical Physics Letters. 323 (2000) 167–172.

[116] D.C. Vaarkamp, M.; Modica, F. S.; Miller, J. T.; Koningsberger, Influence of Hydrogen Pretreatment on the Structure of the Metal-Support Interface in Pt/Zeolite Catalysts, Journal of Catalysis. 144 (1993) 611–626.

[117] A.J. Moraweck, B.; Clugnet, G.; Renouprez, Contraction and relaxation of interatomic distances in small platinum particles from extended X-ray absorption fine structure (EXAFS) spectroscopy, Surface Science. 81 (1979) L631–L634.

[118] B.A. Riguetto, S. Damyanova, G. Gouliev, C.M.P. Marques, L. Petrov, J.M.C. Bueno, Surface Behavior of Alumina-Supported Pt Catalysts Modified with Cerium as Revealed by X-ray Diffraction, X-ray Photoelectron Spectroscopy, and Fourier Transform Infrared Spectroscopy of CO Adsorption, The Journal of Physical Chemistry B. 108 (2004) 5349–5358. doi:10.1021/jp031167s.

[119] H. Song, R. Rioux, J.D. Hoefelmeyer, R. Komor, K. Niesz, M. Grass, P. Yang, G.A. Somorjai, Hydrothermal Growth of Mesoporous SBA-15 Silica in the Presence of PVP-Stabilized Pt Nanoparticles: Synthesis, Characterization, and

Catalytic Properties, J. Am. Chem. Soc. 128 (2006) 3027–3037. doi:10.1021/ja057383r.

[120] I. Tankov, K. Arishtirova, J.M.C. Bueno, S. Damyanova, Surface and structural features of Pt/PrO2–Al2O3 catalysts for dry methane reforming, Applied Catalysis A: General. 474 (2013) 135–148. doi:10.1016/j.apcata.2013.08.030.

[121] P. Bazin, O. Saur, J.C. Lavalley, M. Daturi, G. Blanchard, FT-IR study of CO adsorption on Pt/CeO2: characterisation and structural rearrangement of small Pt particles, Physical Chemistry Chemical Physics. 7 (2005) 187–194. doi:10.1039/b414159h.

[122] R. Grisel, Influence of the Preparation of Au/Al2O3 on CH4 Oxidation Activity, Journal of Catalysis. 191 (2000) 430–437. doi:10.1006/jcat.1999.2787.

[123] L. Wang, F. Meng, Oxygen vacancy and Ce 3 + ion dependent magnetism of monocrystal CeO 2 nanopoles synthesized by a facile hydrothermal method, Materials Research Bulletin. 48 (2013) 3492–3498. doi:10.1016/j.materresbull.2013.05.036.

[124] F. Meng, L. Wang, J. Cui, Controllable synthesis and optical properties of nano-CeO 2 via a facile hydrothermal route, Journal of Alloys and Compounds. 556 (2013) 102–108. doi:10.1016/j.jallcom.2012.12.096.

[125] G. Jacobs, P.M. Patterson, U.M. Graham, D.E. Sparks, B.H. Davis, Low temperature water-gas shift: kinetic isotope effect observed for decomposition of surface formates for Pt/ceria catalysts, Applied Catalysis A: General. 269 (2004) 63–73. doi:10.1016/j.apcata.2004.03.049.

[126] C. Paun, O. V Safonova, J. Szlachetko, P.M. Abdala, M. Nachtegaal, J. Sa, E. Kleymenov, A. Cervellino, F. Krumeich, J.A. Van Bokhoven, Polyhedral CeO2 Nanoparticles: Size-Dependent Geometrical and Electronic Structure, Journal of Physical Chemistry C. 116 (2012) 7312–7317. doi:10.1021/jp300342b.

[127] S. Damyanova, J.M.. Bueno, Effect of CeO2 loading on the surface and catalytic behaviors of CeO2-Al2O3-supported Pt catalysts, Applied Catalysis A: General. 253 (2003) 135–150. doi:10.1016/S0926-860X(03)00500-3.

[128] L. Kepinski, M. Wolcyrz, Hydrogen induced spreading of CeO2 on SiO2, Catalysis Letters. 15 (1992) 329–337.

[129] J.Z. Shyu, W.H. Weber, H.S. Gandhi, Surface characterization of alumina-supported ceria, The Journal of Physical Chemistry. 92 (1988) 4964–4970. doi:10.1021/j100328a029.

[130] G.A. Alayoglu, S.; An, K.; Melaet, G.; Chen, S.; Bernardi, F.; Wang, L. W.; Lindeman, A. E.; Musselwhite, N.; Guo, J.; Liu, Z.; Marcus, M. A.; Somorjai, Pt-mediated reversible reduction and expansion of CeO2 in Pt nanoparticle/mesoporous CeO2 catalyst: in situ X-ray spectroscopy and diffraction studies under redox (H2 and O2) atmospheres, The Journal of Physical Chemistry C. 117 (2013) 26608–26616.

[131] L. Belhadi, F. Decremps, S. Pascarelli, L. Cormier, Y. Le Godec, S. Gorsse, F. Baudelet, C. Marini, G. Garbarino, Polyamorphism in cerium based bulk metallic glasses: Electronic and structural properties under pressure and temperature by x-ray absorption techniques, Applied Physics Letters. 103 (2013) 111905. doi:10.1063/1.4820434.

[132] A. Trovarelli, P. Fornasiero, eds., Catalysis by Ceria and Related Materials, Imperial C, 2002.

[133] L. Barrio, G. Zhou, I.D. Gonzales, M. Estrella, J. Hanson, J.A. Rodriguez, R.M. Navarro, J.L.G. Fierro, In situ characterization of Pt catalysts supported on ceria modified TiO2 for the WGS reaction: influence of ceria loading., Phys. Chem. Chem. Phys. 14 (2012) 2192–2202. doi:10.1039/c1cp22509j.

[134] P.S. Lambrou, C.N. Costa, S.Y. Christou, a. M. Efstathiou, Dynamics of oxygen storage and release on commercial aged Pd-Rh three-way catalysts and their characterization by transient experiments, Applied Catalysis B: Environmental. 54 (2004) 237–250. doi:10.1016/j.apcatb.2004.06.018.

[135] H. Cordatos, T. Bunluesin, J. Stubenrauch, J.M. Vohs, R.J. Gorte, Effect of Ceria Structure on Oxygen Migration for Rh/Ceria Catalysts, The Journal of Physical Chemistry. 100 (1996) 785–789. doi:10.1021/jp952050+.

[136] H.J. Kalakkad, D.S.; Datye, A. K.; Robota, Pt-CeO2 contact and its effect on CO hydrogenation selectivity, Journal of Catalysis. 148 (1994) 729–736. doi:10.1006/jcat.1994.1259.

[137] S.A. Nunan, J. G.; Robota, H. J.; Cohn, M. J.; Bradley, Physicochemical Properties of Ce-Containing Three-Way Catalysts and the Effect of Ce on Catalyst Activity, Journal of Catalysis. 133 (1992) 309–324. doi:10.1016/0021-9517(92)90242-A.

[138] H. Imagawa, A. Suda, K. Yamamura, S. Sun, Monodisperse CeO2 Nanoparticles and Their Oxygen Storage and Release Properties, The Journal of Physical Chemistry C. 115 (2011) 1740–1745. doi:10.1021/jp109878j.

[139] A. Norman, V. Perrichon, Magnetic susceptibility measurements applied to the study of the reversible hydrogen adsorption on high surface area CeO2-ZrO2 mixed oxides in presence of precious metals, Physical Chemistry Chemical Physics. 5 (2003) 3557–3564. doi:10.1039/b303606p.

[140] J.H. Pazmiño, M. Shekhar, W. Damion Williams, M. Cem Akatay, J.T. Miller, W. Nicholas Delgass, F.H. Ribeiro, Metallic Pt as active sites for the water–gas shift reaction on alkali-promoted supported catalysts, Journal of Catalysis. 286 (2012) 279–286. doi:10.1016/j.jcat.2011.11.017.

[141] P. Panagiotopoulou, J. Papavasiliou, G. Avgouropoulos, T. Ioannides, D.I. Kondarides, Water–gas shift activity of doped Pt/CeO2 catalysts, Chemical Engineering Journal. 134 (2007) 16–22. doi:10.1016/j.cej.2007.03.054.

[142] C. Vignatti, M.S. Avila, C.R. Apesteguía, T.F. Garetto, Catalytic and DRIFTS study of the WGS reaction on Pt-based catalysts, International Journal of Hydrogen Energy. 35 (2010) 7302–7312. doi:10.1016/j.ijhydene.2010.04.180.

[143] J.M. Zalc, V. Sokolovskii, D.G. Löffler, Are Noble Metal-Based Water–Gas Shift Catalysts Practical for Automotive Fuel Processing?, Journal of Catalysis. 206 (2002) 169–171. doi:10.1006/jcat.2001.3465.

[144] P. Panagiotopoulou, D.I. Kondarides, Effect of morphological characteristics of TiO2-supported noble metal catalysts on their activity for the water-gas shift reaction, Journal of Catalysis. 225 (2004) 327–336. doi:10.1016/j.jcat.2004.04.030.

[145] D.F. Grenoble, D. C.; Estadt, M. M.; Ollis, The chemistry and catalysis of the

water gas shift reaction, Journal of Catalysis. 67 (1981) 90–102.

[146] T.X.T. Sayle, S.C. Parker, C.R. a. Catlow, The role of oxygen vacancies on ceria surfaces in the oxidation of carbon monoxide, Surface Science. 316 (1994) 329–336. doi:10.1016/0039-6028(94)91225-4.

[147] G. Skandan, C.M. Foster, H. Frase, M.N. Ali, J.C. Parker, H. Hahn, Phase characterization and stabilization due to grain size effects of nanostructured Y2O3, Nanostructured Materials. 1 (1992) 313–322.

[148] J. Vecchietti, A. Bonivardi, W. Xu, D. Stacchiola, J.J. Delgado, M. Calatayud, S.E. Collins, Understanding the Role of Oxygen Vacancies in the Water Gas Shift Reaction on Ceria-Supported Platinum Catalysts, ACS Catalysis. 4 (2014) 2088–2096. doi:10.1021/cs500323u.

[149] D. Koningsberger, In situ X-ray absorption spectroscopy as a unique tool for obtaining information on hydrogen binding sites and electronic structure of supported Pt catalysts: towards an understanding of the compensation relation in alkane hydrogenolysis, Journal of Catalysis. 216 (2003) 178–191. doi:10.1016/S0021-9517(02)00135-5.

[150] G. Jacobs, S. Ricote, U.M. Graham, B.H. Davis, Low Temperature Water-Gas Shift Reaction: Interactions of Steam and CO with Ceria Treated with Different Oxidizing and Reducing Environments, Catalysis Letters. 145 (2015) 533–540. doi:10.1007/s10562-014-1440-0.

[151] W. Xu, R. Si, S.D. Senanayake, J. Llorca, H. Idriss, D. Stacchiola, J.C. Hanson, J.A. Rodriguez, In situ studies of CeO2-supported Pt, Ru, and Pt–Ru alloy catalysts for the water–gas shift reaction: Active phases and reaction intermediates, Journal of Catalysis. 291 (2012) 117–126. doi:10.1016/j.jcat.2012.04.013.

[152] J. a. Rodriguez, Gold-based catalysts for the water–gas shift reaction: Active sites and reaction mechanism☆, Catalysis Today. 160 (2011) 3–10. doi:10.1016/j.cattod.2010.06.030.

[153] R.J. Madon, D. Braden, S. Kandoi, P. Nagel, M. Mavrikakis, J. a. Dumesic, Microkinetic analysis and mechanism of the water gas shift reaction over copper catalysts, Journal of Catalysis. 281 (2011) 1–11. doi:10.1016/j.jcat.2011.03.008.

[154] O. V. Safonova, A.A. Guda, C. Paun, N. Smolentsev, P.M. Abdala, G. Smolentsev, M. Nachtegaal, J. Szlachetko, M.A. Soldatov, A. V. Soldatov, J.A. Van Bokhoven, Electronic and geometric structure of Ce3+ forming under reducing conditions in shaped ceria nanoparticles promoted by platinum, Journal of Physical Chemistry C. 118 (2014) 1974–1982. doi:10.1021/jp409571b.

[155] Y. Lykhach, V. Johánek, H.A. Aleksandrov, S.M. Kozlov, M. Happel, T. Skála, P.S. Petkov, N. Tsud, G.N. Vayssilov, K.C. Prince, K.M. Neyman, V. Matolín, J. Libuda, Water chemistry on model ceria and Pt/ceria catalysts, Journal of Physical Chemistry C. 116 (2012) 12103–12113. doi:10.1021/jp302229x.

[156] D.R. Mullins, P.M. Albrecht, T.-L. Chen, F.C. Calaza, M.D. Biegalski, H.M. Christen, S.H. Overbury, Water Dissociation on CeO 2 (100) and CeO 2 (111) Thin Films, The Journal of Physical Chemistry C. 116 (2012) 19419–19428. doi:10.1021/jp306444h.

[157] U. Berner, K. Schierbaum, G. Jones, P. Wincott, S. Haq, G. Thornton, Ultrathin

ordered CeO overlayers on Pt (111): interaction with NO , NO , H O and CO, Surface Science. 467 (2000) 201–213.

[158] V. Matolín, I. Matolínová, F. Dvořák, V. Johánek, J. Mysliveček, K.C. Prince, T. Skála, O. Stetsovych, N. Tsud, M. Václavů, B. Šmíd, Water interaction with CeO2(111)/Cu(111) model catalyst surface, Catalysis Today. 181 (2012) 124–132. doi:10.1016/j.cattod.2011.05.032.

[159] A.M. Efstathiou, Catalysis, J. Spivey, RSC, 2016.

[160] J.P. Clay, J.P. Greeley, F.H. Ribeiro, W.N. Delgass, W.F. Schneider, DFT comparison of intrinsic WGS kinetics over Pd and Pt, Journal of Catalysis. 320 (2014) 106–117. doi:10.1016/j.jcat.2014.09.026.

[161] M. Gonzalez Castaño, T.R. Reina, S. Ivanova, M. a. Centeno, J. a. Odriozola, Pt vs. Au in water–gas shift reaction, Journal of Catalysis. 314 (2014) 1–9. doi:10.1016/j.jcat.2014.03.014.

[162] F.C. Meunier, D. Tibiletti, a. Goguet, S. Shekhtman, C. Hardacre, R. Burch, On the complexity of the water-gas shift reaction mechanism over a Pt/CeO2 catalyst: Effect of the temperature on the reactivity of formate surface species studied by operando DRIFT during isotopic transient at chemical steady-state, Catalysis Today. 126 (2007) 143–147. doi:10.1016/j.cattod.2006.10.003.

[163] F.C. Meunier, A. Goguet, C. Hardacre, R. Burch, D. Thompsett, Quantitative DRIFTS investigation of possible reaction mechanisms for the water-gas shift reaction on high-activity Pt- and Au-based catalysts, Journal of Catalysis. 252 (2007) 18–22. doi:10.1016/j.jcat.2007.09.003.

[164] C.M. Kalamaras, S. Americanou, A.M. Efstathiou, “Redox” vs “associative formate with -OH group regeneration” WGS reaction mechanism on Pt/CeO2: Effect of platinum particle size, Journal of Catalysis. 279 (2011) 287–300. doi:10.1016/j.jcat.2011.01.024.

[165] P. Panagiotopoulou, D.I. Kondarides, Effect of the nature of the support on the catalytic performance of noble metal catalysts for the water-gas shift reaction, Catalysis Today. 112 (2006) 49–52. doi:10.1016/j.cattod.2005.11.026.

[166] C. Kalamaras, D. Dionysiou, A. Efstathiou, Mechanistic Studies of the Water–Gas Shift Reaction over Pt/Ce x Zr1–x O2 Catalysts: The Effect of Pt Particle Size and Zr Dopant, ACS Catalysis. 2 (2012) 2729–2742. doi:10.1021/cs3006204.

[167] C.M. Kalamaras, K.C. Petallidou, A.M. Efstathiou, The effect of La3+-doping of CeO2 support on the water-gas shift reaction mechanism and kinetics over Pt/Ce1-xLaxO2-??, Applied Catalysis B: Environmental. 136–137 (2013) 225–238. doi:10.1016/j.apcatb.2013.02.003.

[168] K.C. Petallidou, A.M. Efstathiou, Low-temperature water-gas shift on Pt/Ce1-xLaxO2-??: Effect of Ce/La ratio, Applied Catalysis B: Environmental. 140–141 (2013) 333–347. doi:10.1016/j.apcatb.2013.04.007.

[169] K.C. Petallidou, C.M. Kalamaras, A.M. Efstathiou, The effect of La3+, Ti4+ and Zr4+ dopants on the mechanism of WGS on ceria-doped supported Pt catalysts, Catalysis Today. 228 (2014) 183–193. doi:10.1016/j.cattod.2013.10.081.

[170] K.C. Petallidou, S. Boghosian, A.M. Efstathiou, Low-temperature water-gas shift on Pt/Ce0.5La0.5O2-δ: Effect of support synthesis method, Catalysis Today.

242 (2015) 153–167. doi:10.1016/j.cattod.2014.06.042.

[171] J. Ke, W. Zhu, Y. Jiang, R. Si, Y.-J. Wang, S.-C. Li, C. Jin, H. Liu, W.-G. Song, C.-H. Yan, Y.-W. Zhang, Strong Local Coordination Structure Effects on Subnanometer PtO_x Clusters over CeO_2 Nanowires Probed by Low-Temperature CO Oxidation, ACS Catalysis. 5 (2015) 5164–5173. doi:10.1021/acscatal.5b00832.

[172] M. Yang, J. Liu, S. Lee, B. Zugic, J. Huang, L.F. Allard, M. Flytzani-Stephanopoulos, A Common Single-Site Pt(II)-O(OH)x- Species Stabilized by Sodium on “active” and “inert” Supports Catalyzes the Water-Gas Shift Reaction, Journal of the American Chemical Society. 137 (2015) 3470–3473. doi:10.1021/ja513292k.

[173] M.T. Paffett, S.C. Gebhard, R.G. Windham, B.E. Koel, Chemisorption of CO , H2, and O2 on Ordered Sn/Pt(111) Surface Alloys, Society. 94 (1990) 6831–6839. doi:10.1021/j100380a053.

[174] G. Pirug, H.P. Bonzel, G. Broden, The adsorption of potassium on Pt(111) and its effect on oxygen adsorption, Surface Science. 122 (1982) 1–20. doi:10.1016/0039-6028(82)90055-3.

[175] C.N. Ávila-Neto, J.W.C. Liberatori, a. M. da Silva, D. Zanchet, C.E. Hori, F.B. Noronha, J.M.C. Bueno, Understanding the stability of Co-supported catalysts during ethanol reforming as addressed by in situ temperature and spatial resolved XAFS analysis, Journal of Catalysis. 287 (2012) 124–137. doi:10.1016/j.jcat.2011.12.013.

[176] J.T. Guo, N.; Fingland, B. R.; Williams, W. D.; Kispersky, V. F.; Jelic, J.; Delgass, W. N.; Ribeiro, F. H.; Meyer, R. J.; Miller, Determination of CO, H2O and H2 coverage by XANES and EXAFS on Pt and Au during water gas shift reaction, Physical Chemistry Chemical Physics : PCCP. 12 (2010) 5678–5693. doi:10.1039/b926434e.

[177] D.C. Ramaker, D.E.; Koningsberger, The atomic AXAFS and Dl XANES techniques as applied to heterogeneous catalysis and electrocatalysis, Physical Chemistry Chemical Physics : PCCP. 12 (2010) 5514–5534. doi:10.1039/b926434e.

[178] Y. Ji, V. Koot, a Vandereerden, B. Weckhuysen, D. Koningsberger, D. Ramaker, A three-site Langmuir adsorption model to elucidate the temperature, pressure, and support dependence of the hydrogen coverage on supported Pt particles, Journal of Catalysis. 245 (2007) 415–427. doi:10.1016/j.jcat.2006.10.028.

[179] J. Xu, J.T. Yates, Terrace width effect on adsorbate vibrations: a comparison of Pt(335) and Pt(112) for chemisorption of CO, Surface Science. 327 (1995) 193–201. doi:10.1016/0039-6028(94)00849-3.

[180] M. Vaarkamp, J.T. Miller, F.S. Modica, D.C. Koningsberger, On the Relation between Particle Morphology , Structure of the Metal-Support Interface , and Catalytic Properties of Pt / γ -Al 2 O 3, Journal of Catalysis. 163 (1996) 294–305.

[181] a. Y. Stakheev, Y. Zhang, a. V. Ivanov, G.N. Baeva, D.E. Ramaker, D.C. Koningsberger, Separation of Geometric and Electronic Effects of the Support on the CO and H2 Chemisorption Properties of Supported Pt Particles: The Effect of Ionicity in Modified Alumina Supports, Journal of Physical Chemistry C. 111 (2007) 3938–3948. doi:10.1021/jp0651182.

[182] F.J. Scott, C. Roth, D.E. Ramaker, T. George, W. Uni, Kinetics of CO Poisoning in Simulated Reformate and Effect of Ru Island Morphology on PtRu Fuel Cell Catalysts As Determined by Operando X-ray Absorption Near Edge Spectroscopy, J. Phys. Chem. C. 111 (2007) 11403–11413.

[183] F.J. Scott, S. Mukerjee, D.E. Ramaker, CO Coverage/Oxidation Correlated with PtRu Electrocatalyst Particle Morphology in 0.3 M Methanol by In Situ XAS, Journal of The Electrochemical Society. 154 (2007) A396–A406. doi:10.1149/1.2709496.

[184] M. Teliska, V.S. Murthi, S. Mukerjee, D.E. Ramaker, Correlation of Water Activation, Surface Properties, and Oxygen Reduction Reactivity of Supported Pt–M/C Bimetallic Electrocatalysts Using XAS, Journal of The Electrochemical Society. 152 (2005) A2159–A2169. doi:10.1149/1.2040949.

[185] B. Zugic, D.C. Bell, M. Flytzani-Stephanopoulos, Activation of carbon-supported platinum catalysts by sodium for the low-temperature water-gas shift reaction, Applied Catalysis B: Environmental. 144 (2014) 243–251. doi:10.1016/j.apcatb.2013.07.013.

[186] N. Aaron Deskins, D. Mei, M. Dupuis, Adsorption and diffusion of a single Pt atom on γ-Al2O3 surfaces, Surface Science. 603 (2009) 2793–2807. doi:10.1016/j.susc.2009.07.021.

[187] F. Vila, J. Rehr, J. Kas, R. Nuzzo, a. Frenkel, Dynamic structure in supported Pt nanoclusters: Real-time density functional theory and x-ray spectroscopy simulations, Physical Review B. 78 (2008) 121404. doi:10.1103/PhysRevB.78.121404.

[188] L. Wang, D.D. Johnson, Shear Instabilities in Metallic Nanoparticles : Hydrogen-Stabilized Structure of Pt 37 on Carbon, Journal of American Chemistry Society. 129 (2007) 3658–3664.

[189] T. Zheng, J. He, Y. Zhao, W. Xia, J. He, Precious metal-support interaction in automotive exhaust catalysts, Journal of Rare Earths. 32 (2014) 97–107. doi:10.1016/S1002-0721(14)60038-7.

[190] M.M. Smith, J. M. Van Ness, H. C. Abbot, Introdução à Termodinâmica da Engenharia Química, 2007.

Annex A

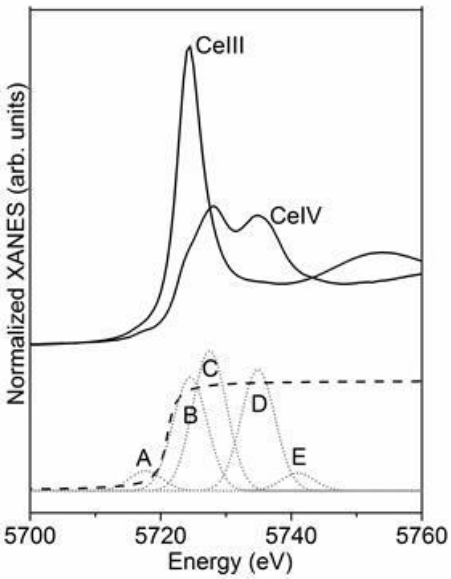

Figure 1. Gaussians positions found for the CeIV and CeIII standards. Arctan is placed in this picture for CeIV standard.

Calculating the turn over frequency (TOF)

Considering a reaction:

$$A + B \rightarrow C + D$$

The reaction conversion is given:

x_A and x_B for the reactants A e B, respectively

Fluxes at reactor entrance are F_A e F_B for the reactants A e B, respectively.

1) **Converting the flux from (ml/min) to mol/min**
   Ideal gas law:

$$P(atm)*V\ (L)=n\ (mol)*R(L*atm*K^{-1}*mol^{-1})*T(K) \qquad \text{(eq.1)}$$

   Knowing
   P = 1 atm (atmospheric pressure)
   R = 0,0820574587 (gases constant, $L*atm*K^{-1}*mol^{-1}$)
   T = reaction temperature (K)

2) Reaction rate

Reaction rate r_A (mol*s^{-1}*g^{-1}) is given by:

$$r_A\,(mol * s^{-1}g^{-1}) = (n\,(mol) * x_A)/m_{catalyst} \quad \text{(eq. 3)}$$

Where:

x_A = experimental conversion
$m_{catalyst}$ = catalyst mass used for the catalytic test

3) Partial pressure at reactor entrance

$$P_{0A} = \frac{F_A}{F_A + F_B}$$

$$P_{0B} = \frac{F_B}{F_A + F_B}$$

4) Partial pressure at reactor exit

For reactant A (limiting reactant)

$$P_{SA} = (F_A - F_A * x_A)/(F_A + F_B) \quad \text{(eq.5)}$$

For reactant B

$$P_{SB} = (F_B - F_A * x_A)/(F_A + F_B) \quad \text{(eq.6)}$$

For product C

$$P_{SC} = (F_A * x_A)/(F_A + F_B) \quad \text{(eq.7)}$$

And $P_{SC} = P_{SD}$ (stoichiometric coefficients are all 1)

5) Direct reaction rate r_0 (mol*s^{-1}*g^{-1})

$$r_0 = \frac{r_{A*}(\frac{F_A}{F_A+F_B}*\frac{F_B}{F_AF_B})}{P_{SA*}\left(\frac{F_B}{F_A+F_B}-P_{SC}\right)-\frac{(P_{SC*}P_{SD})}{K_{eq}}} \qquad \text{(eq.8)}$$

6) Equilibrium constant Keq:

$$K = \exp\left(\frac{-\Delta G^\circ}{RT}\right) \qquad \text{(eq.9)}$$

$$\Delta G^\circ = \Delta H^\circ - T\Delta S^\circ \quad \text{(eq.10)}$$

$$\Delta H^\circ = \Delta H_o^\circ + R\int_{T_o}^{T}\frac{\Delta C_p^\circ}{R}dT \quad \text{(eq11)}$$

$$\Delta S^\circ = \Delta S_o^\circ + R\int_{T_o}^{T}\frac{\Delta C_p^\circ}{RT}dT \quad \text{(eq12)}$$

Substituting 11 e 12 in 10

$$\Delta G^\circ = \Delta H_o^\circ + R\int_{T_o}^{T}\frac{\Delta C_p^\circ}{R}dT - T\left(\Delta S_o^\circ + R\int_{T_o}^{T}\frac{\Delta C_p^\circ}{RT}dT\right) \qquad \text{eq (13)}$$

Where

$\Delta S_o^\circ = \frac{\Delta H_o^\circ - \Delta G_o^\circ}{T_o}$ eq (14)

And:

ΔH_o° e ΔG_o° tabulated data for each gas at 298,15K .

Substituting eq. 14 in eq 13

$$\Delta G^\circ = \Delta H_o^\circ + R\int_{T_o}^{T}\frac{\Delta C_p^\circ}{R}dT - T\left(\frac{\Delta H_o^\circ - \Delta G_o^\circ}{T_o} + R\int_{T_o}^{T}\frac{\Delta C_p^\circ}{RT}dT\right) \quad \text{(eq.15)}$$

Dividing by RT and rearranging

$$\frac{\Delta G^\circ}{RT} = \frac{\Delta H_o^\circ}{RT} + \frac{1}{T}\int_{T_o}^{T} \frac{\Delta C_p^\circ}{R} dT - \frac{1}{R}\frac{\Delta H_o^\circ - \Delta G_o^\circ}{T_o} - \frac{1}{T}\int_{T_o}^{T} \frac{\Delta C_p^\circ}{RT} dT$$

$$\frac{\Delta G^\circ}{RT} = \frac{\Delta G_o^\circ - \Delta H_o^\circ}{RT_o} + \frac{\Delta H_o^\circ}{RT} + \frac{1}{T}\left(\int_{T_o}^{T} \frac{\Delta C_p^\circ}{R} dT - \int_{T_o}^{T} \frac{\Delta C_p^\circ}{RT} dT\right) \quad \text{(eq. 16)}$$

- To calculate ΔH_o°

$$\Delta H_o^\circ = \sum v_i \, \Delta H_o{}^\circ{}_{fi} = \sum \Delta H_o{}^\circ{}_{f\ products} - \sum \Delta H_o{}^\circ{}_{f\ reactants} \quad \text{(eq. 17)}$$

- To calculate ΔG_o°

$$\Delta G_o^\circ = \sum v_i \, \Delta G_o{}^\circ{}_{fi} = \sum \Delta G_o{}^\circ{}_{f\ products} - \sum \Delta G_o{}^\circ{}_{f\ reactants} \quad \text{(eq. 18)}$$

- To calculate $\Delta C_p{}^\circ$

$$\Delta C_p^\circ = \sum v_i \, C_p{}^\circ{}_i = \sum C_p{}^\circ{}_{products} - \sum C_p{}^\circ{}_{reactants} \quad \text{(eq. 19)}$$

- Gases heat capacity

$$C_p = R(A + BT + CT^2 + DT^{-2}) \quad \text{(eq. 20)}$$

$$\Delta C_p = R(\Delta A + \Delta BT + \Delta CT^2 + \Delta DT^{-2}) \quad \text{(eq. 21)}$$

Where A, B, C and D are tabulated data em presented at Table 1 [190].

Table 1. Constants to calculate the heat capacity.

	A	B	C	D
Carbon monoxide	3.376	0.557	0	-0.031
Water	3.47	1.45	0	0.121
Carbon dioxide	5.457	1.045	0	-1.157
Hydrogen	3.249	0.422	0	0.083

For the first integral from equation 16:

$$\int_{T_o}^{T} \frac{\Delta C_p^\circ}{R} dT = \int_{T_o}^{T} (\Delta A + \Delta BT + \Delta CT^2 + \Delta DT^{-2}) dT$$

$$\int_{T_o}^{T} \frac{\Delta C_p^{\circ}}{R} dT = \Delta A T + \frac{\Delta B}{2} T^2 + \frac{\Delta C}{3} T^3 - \Delta D T^{-1} \Big|_{T_o}^{T} \quad \text{(eq. 22)}$$

For the second integral from equation 16:

$$\int_{T_o}^{T} \frac{\Delta C_p^{\circ}}{RT} dT = \int_{T_o}^{T} \left(\frac{\Delta A}{T} + \Delta B + \Delta C T + \Delta D T^{-3} \right) dT$$

$$\int_{T_o}^{T} \frac{\Delta C_p^{\circ}}{RT} dT = \Delta A \, ln(T) + \Delta B T + \frac{\Delta C}{2} T^2 - \frac{\Delta D}{2} T^{-2} \Big|_{T_o}^{T} \quad \text{(eq. 23)}$$

Substituting all values at equation 16 we can find the equilibrium constant. Then we can find r_0. After this to calculate the activation energy is necessary to plot $\ln(r_0)$ for y axis versus 1/T x axis. The line slope will be the Activation Energy due to the Arrhenius equation.

7) TOF calculation

$$TOF = \frac{F_A(mol*s^{-1})*x_A*MM(g*mol^{-1})}{m_{catalisador}*t_m*d} \quad \text{(eq. 14)}$$

Where

MM = molecular mass of metallic phase

t_m = metallic phase percentage in the sample

d = dispersion (can be calculated from EXAFS data, microscopy, nitrous oxide, etc. The idea is to find out how much from the total metallic phase is at the surface). We will use the dispersion calculated by EXAFS data as explained before.

As mentioned before the terms in red correspond to the reaction rate (r_A). However, for certain reactions like WGS to calculate the TOF correctly would be necessary to do the catalytic test using the reactants and the products to feed the reactor since it would be a more realistic condition similar to the reform outlet. When it is not possible we have to calculate an “apparent” TOF using the direct reaction rate r_0 that is what is presented at the results.

Annex B

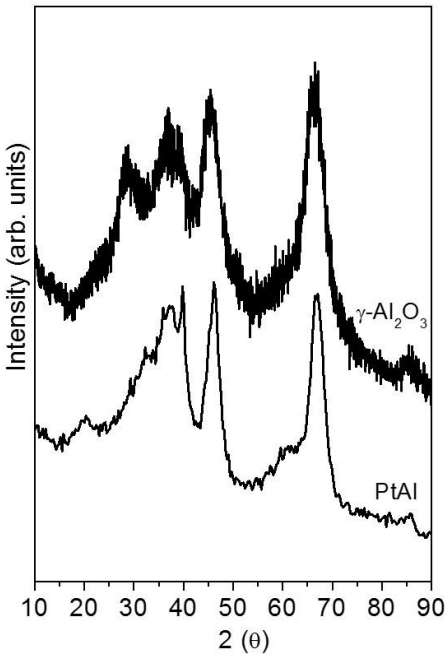

Figure 1. Diffraction patterns for the samples γ-Al_2O_3 and PtAl.

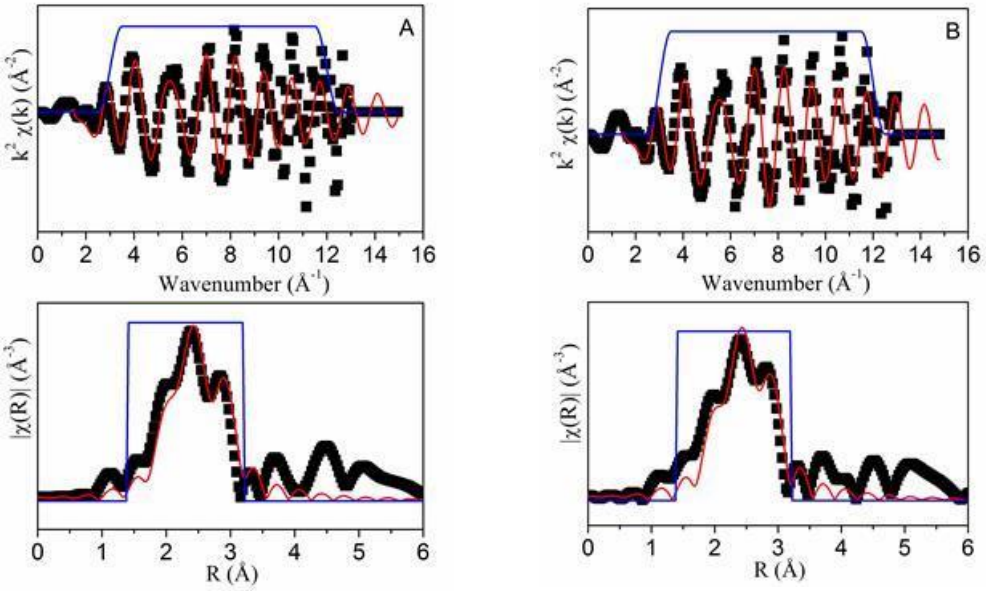

Figure 2. EXAFS data and fit at k space and Magnitude of the Fourier transforms for (A) g-Pt12CeAl and (B) i-12CePtAl after the reduction. Black squares (data); red line (fit) and blue line (window).

Table 1: EXAFS fits results after reduction.

	PtAl	**g-Pt12CeAl**	**i-12CePtAl**	**Pt^0**
N_{Pt-Pt}	6.5 (± 0.6)	6 (± 1)	6 (± 1)	12
R_{Pt-Pt} (Å)	2.75 (± 0.01)	2.76 (± 0.01)	2.75 (± 0.01)	2.76 (± 0.02)
σ^2_{Pt-Pt} (Å²)	0.006 (± 0.001)	0.009 (± 0.002)	0.007 (± 0.002)	0.004 (± 0.003)

Values found for the Pt foil and fixed for all samples: $E_0 = 9$; $S_0^2 = 0.9$

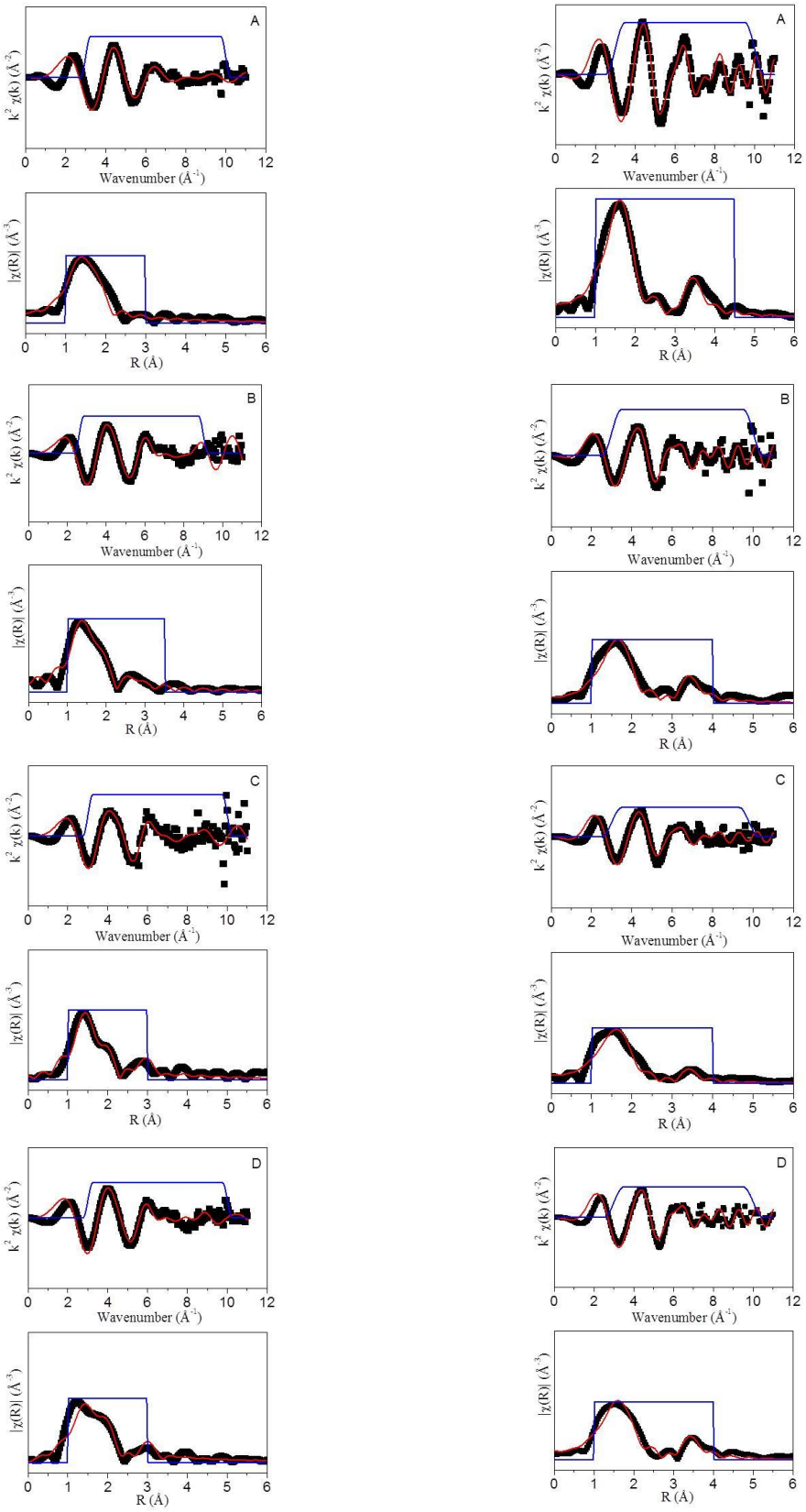

Figure 3. EXAFS data and fit at k space and Magnitude of the Fourier transforms for g-Pt12CeAl (left) and i-12CePtAl (right). (A) Calcined; (B) reduced 25 ^{0}C; (C) H_2 500 ^{0}C; (D) WGS 250 ^{0}C

Table 2: Structural parameters obtained from EXAFS analysis of g-Pt12CeAl under H_2 500 ^{0}C and WGS 250 ^{0}C.

	H_2 500 ^{0}C	WGS 250 ^{0}C
N_{Ce-O1}	3 (± 1)	4 (± 3)
R_{Ce-O1} (Å)	2.20 (± 0.02)	2.20 (± 0.03)
N_{Ce-O2}	3 (± 1)	5 (± 3)
R_{Ce-O2} (Å)	2.4 (± 0.03)	2.40 (± 0.04)
N_{Ce-Al}	4 (± 3)	3 (± 4)
R_{Ce-Al}	3.60 (± 0.06)	3.7 (± 0.1)
σ_{Ce-O}^2 / σ_{Ce-Al}^2 (Å)	0.003 (± 0.006) / 0.01 (± 0.03)	0.008 (± 0.01) / 0.01 (± 0.03)

(a) after reduction; E_0 = -15 (± 5), S_o^2 = 0.9.

Table 3: Structural parameters obtained from EXAFS analysis of i-12PtCeAl under H_2 500 ^{0}C and WGS 250 ^{0}C.

	H_2 500 ^{0}C	WGS 250 ^{0}C
N_{Ce-O1}	7 (± 2)	7 (± 2)
R_{Ce-O1} (Å)	2.31 (± 0.01)	2.31 (± 0.01)
N_{Ce-Ce}	1.1 (± 0.7)	2.0 (± 0.6)
R_{Ce-Ce} (Å)	3.78 (± 0.04)	3.79 (± 0.02)
σ_{Ce-O}^2 / σ_{Ce-Ce}^2 (Å)	0.02 (± 0.006) / 0.005 (± 0.002)	0.02 (± 0.005) / 0.005 (± 0.002)

(a) after reduction; E_0 = -9 (± 2), S_o^2 = 0.9.

Annex C

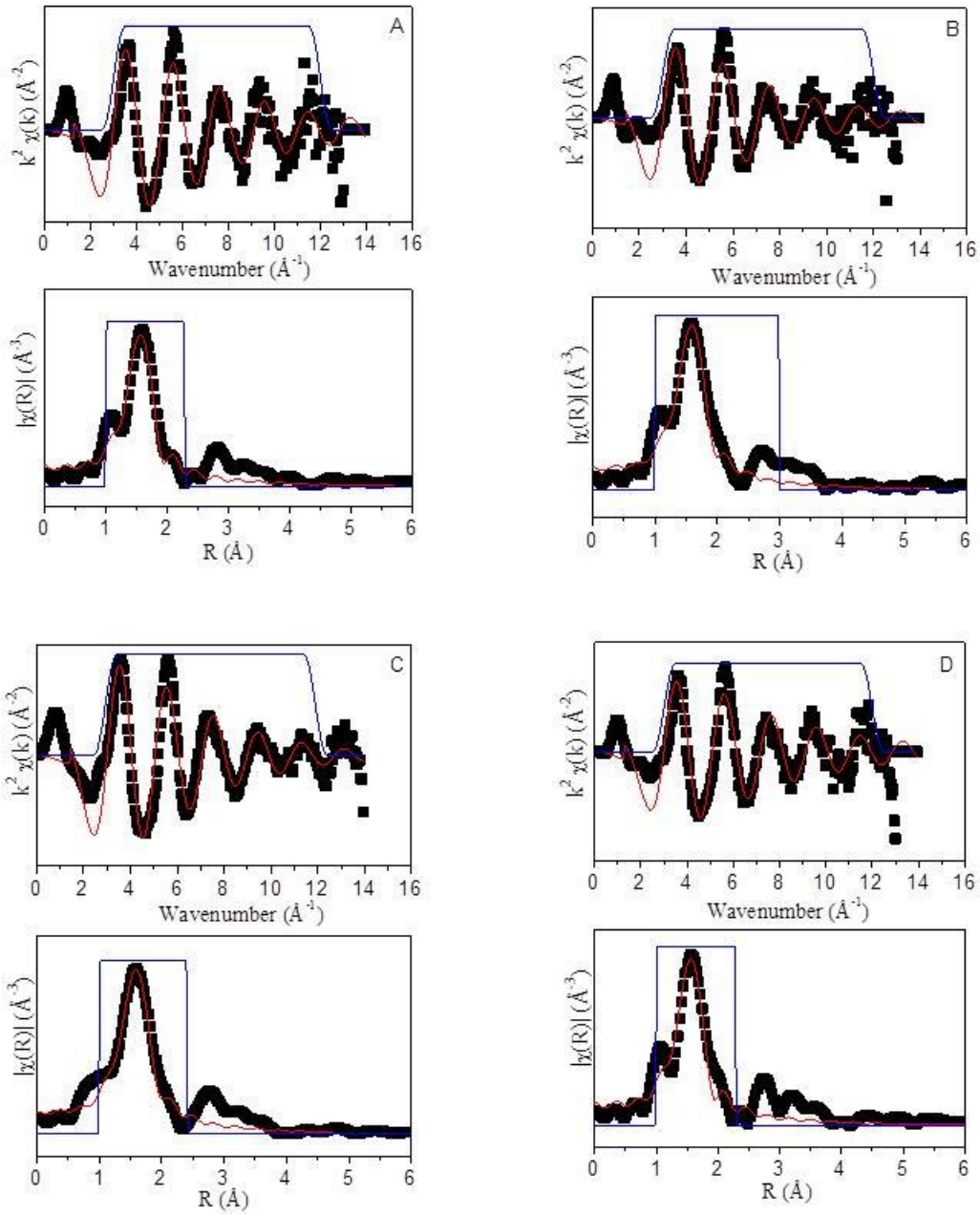

Figure 1. EXAFS data and fit at k space and Magnitude of the Fourier transforms before the reduction (A) 12Ce03PtAl, (B) 1PtAl, (C) 6Ce1PtAl, (D) 12Ce1PtAl

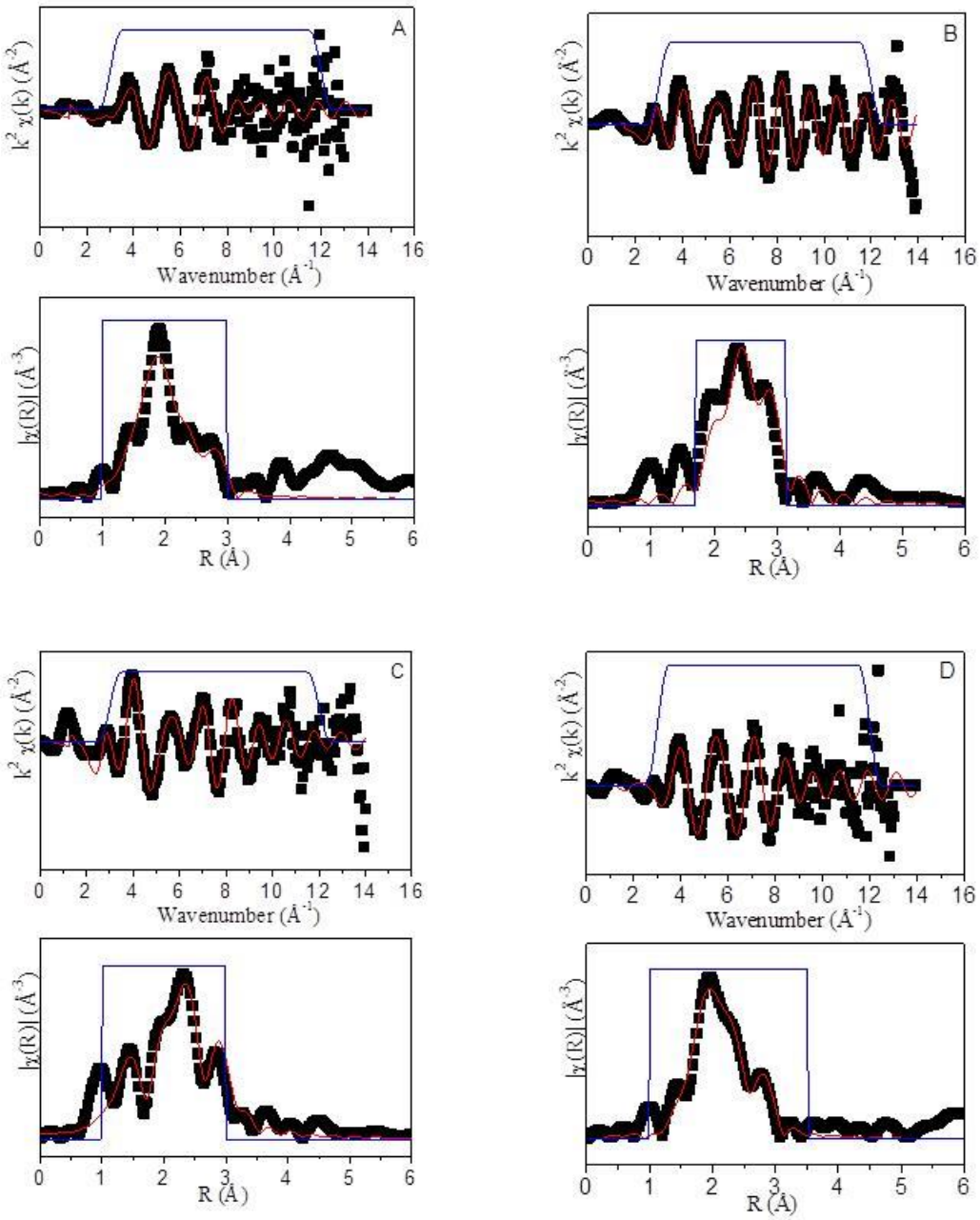

Figure 2. EXAFS data and fit at k space and Magnitude of the Fourier transforms after the reduction (A) 12Ce03PtAl, (B) 1PtAl, (C) 6Ce1PtAl, (D) 12Ce1PtAl

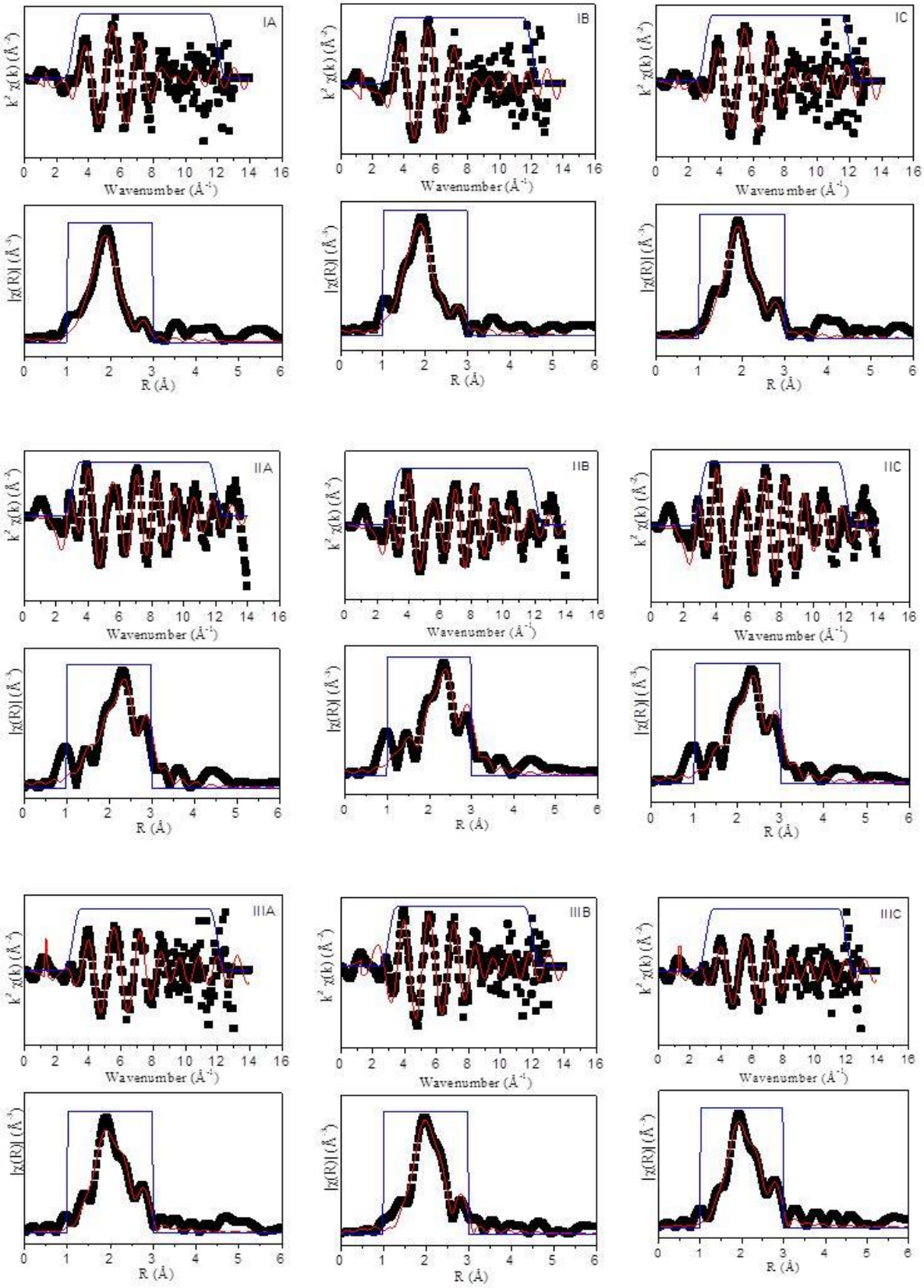

Figure 3. EXAFS data and fit at k space and Magnitude of the Fourier transforms 250 ^{0}C (A) H_2, (B) WGS, (C) H_2-second time, (I) 12Ce03PtAl, (II) 1PtAl, (III) 12Ce1PtAl

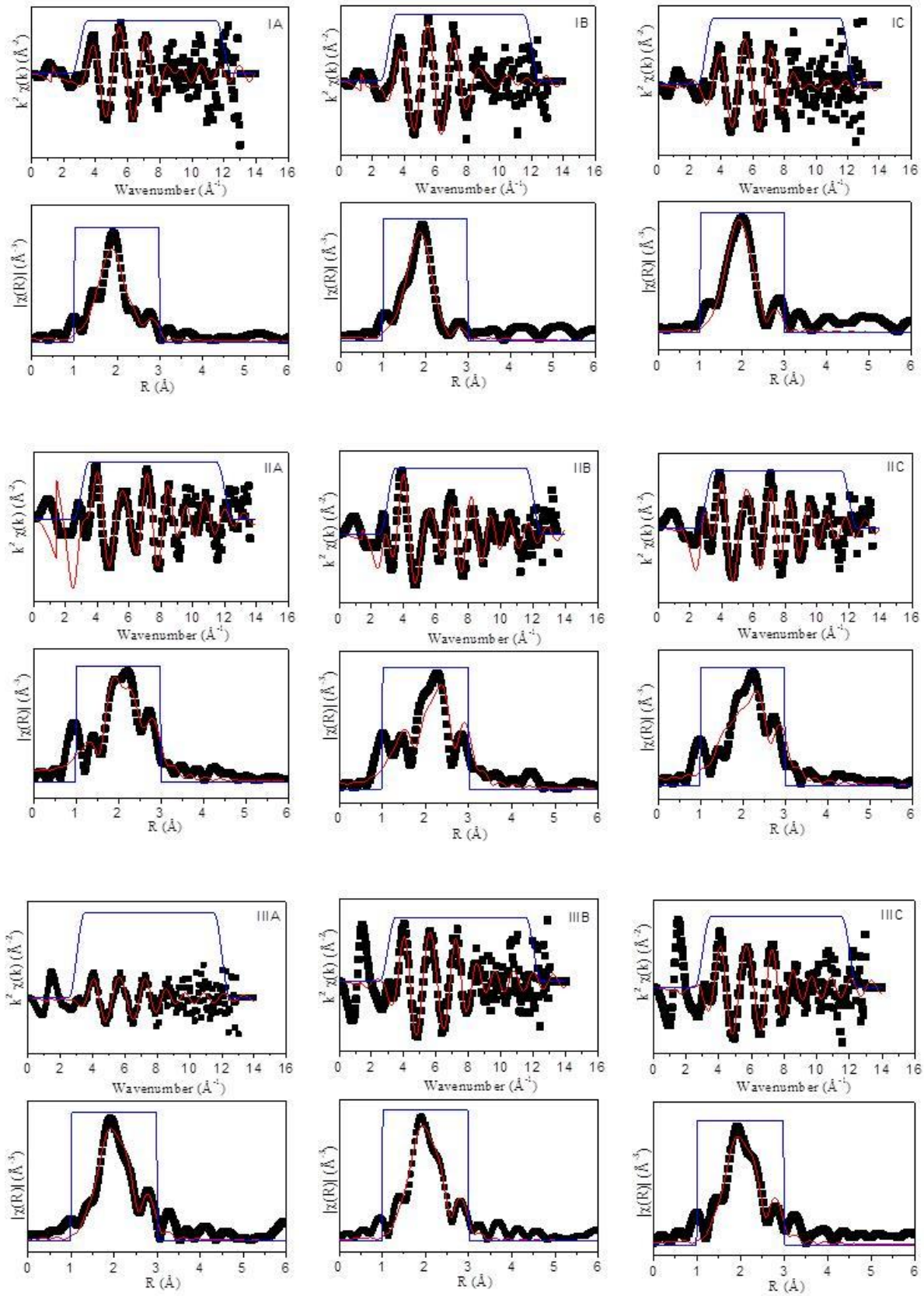

Figure 4. EXAFS data and fit at k space and Magnitude of the Fourier transforms 350 ^{0}C (A) H_2, (B) WGS, (C) H_2-second time, (I) 12Ce03PtAl, (II) 6Ce1PtAl, (III) 12Ce1PtAl.